

https://dspace.org/

Synthesis and application of boron-nitrogen doped carbon nano-onions in supercapacitors

Shaku, Bokome

2020

https://hdl.handle.net/10539/31031

Shaku, Bokome (2020) Synthesis and application of boron-nitrogen doped carbon nanoonions in supercapacitors, University of the Witwatersrand, Johannesburg, <http://hdl.handle.net/10539/31031>

Downloaded from a DSpace repository. https://dspace.org/

Synthesis and application of boron-nitrogen doped carbon nano-onions in supercapacitors

By

Bokome Shaku

Student Number: 726829

Supervisors:

Dr Manoko S. Maubane-Nkadimeng

Prof Neil J. Coville

Prof Kenneth I. Ozoemena

A dissertation submitted to the Faculty of Science,

University of the Witwatersrand, Johannesburg,

in fulfilment for the degree of

Master of Science in Chemistry

January, 2020.

DECLARATION

I declare that this dissertation, which is hereby submitted for a degree of Master of Science in the Faculty of Science, School of Chemistry, University of the Witwatersrand, Johannesburg is my own unaided work and has not been submitted for examination at any institution.

UNIVERSITY OF THE
WITWATERSRAND,
JOHANNESBURG



(*Signed*) Bokome Shaku

On this 28th day of January 2020

DEDICATION

This work is dedicated to my family:

My late loving father (Makate W. Shaku) and my mother (Mokgohloe O. Shaku)

ACKNOWLEDGEMENTS

There are numerous people I would like to thank for contributing to this work. Firstly, I would like to thank the **Almighty God** for everything in my life. Thank you, dear God, for this good life. I wish to express my warm and sincere thanks to my supervisor, **Dr Manoko S. Maubane-Nkadimeng,** for giving me huge assistance in designing the research project and equipping me with problem solving skills. Thank you for your endless support, kind and understanding spirit.

I am extremely thankful to my co-supervisors, **Prof Neil J. Coville** and **Prof Kenneth I. Ozoemena,** for their valuable guidance and support throughout completing this project.

I extend my gratitude to my mentors, **Dr Bridget Mutuma** and **Dr Boitumelo Matsoso,** for their kindness and mentorship throughout this project. Special thanks to **Thomas Mongwe** and **Thapelo Mofokeng** for helping me in the laboratory. To the School of Chemistry and also CATMAT, C-dots and Ozoemena research groups at the University of the Witwatersrand - thanks for the enthusiasm, support and for making the lab a greatest place to be.

I am grateful to the microscopy and microanalysis unit (MMU) for allowing me to make use of their instruments. Many thanks to **Dr Rudolph Erasmus** for his kind assistance with the Raman spectroscopy analysis. Special thanks to **Rhandzu Rikhotso** for allowing me to do high resolution transmission electron microscopy (HRTEM) analysis through the Council for Scientific and Industrial Research (CSIR) characterization facility.

Special gratitude to the National Research Foundation **(NRF)** of South Africa, DSI-NRF Centre of Excellence in Strong Materials **(CoE-SM)** and Post-graduate Merit Award **(PMA)** for financial assistance. Thanks a lot for settling all my academic fees, stipends, chemicals and conference expenses.

I also acknowledge with a deep sense of reverence, my gratitude towards my parents and members of my family, who gave me endless support. Dear **mom** and **dad**, you planted a seed and got to watch it grow. Now your seed is blossoming. Thank you so much for everything.

Lastly, I would like to thank good friends of mine, **Mothekgi Shaku and Lesiba Papo,** for being there for me always. Thanks for the support, understanding and unconditional love.

PRESENTATIONS

- SACI 2018 conference: Poster presentation "*Properties of catalyst-free carbon nano-onions grown by the flame pyrolysis method for possible application in supercapacitors*" Pretoria, South Africa.
- CoE-SM/AMSEN annual student presentation (2019): Poster presentation "*Synthesis and application of nitrogen-doped carbon nano-onions in supercapacitors*" University of the Witwatersrand, South Africa.
- Energy storage and Industry 4.0 (ENSTIN 2019): Poster presentation "*Physico-chemical properties of catalyst-free carbon nano-onions grown by the flame pyrolysis method for possible application in supercapacitors*" KwaMaritane Bush Lodge, Pilanesburg National Park, South Africa.
- 70th Annual meeting of the International Society of Electrochemistry (2019): Poster presentation "*Physico-chemical properties of catalyst-free carbon nano-onions grown by the flame pyrolysis method for possible application in supercapacitors*" Durban, South Africa.
- Wits Cross Faculty 2019 Symposium: Poster presentation "*Physico-chemical properties of catalyst-free carbon nano-onions grown by the flame pyrolysis method for possible application in supercapacitors*" University of the Witwatersrand, South Africa.

ABSTRACT

This work reports on the synthesis of carbon nano-onions (CNOs) via the chemical vapor deposition (CVD) and flame pyrolysis methods for application in supercapacitors (SCs).

The synthesis of CNOs using CVD was achieved by reducing a Fe-Co catalyst to its metallic state, followed by decomposition of acetylene (C_2H_2) as a carbon source. The metal catalyst was supported on calcium carbonate ($CaCO_3$). The synthesis of CNOs was carried out at different reaction temperatures (i.e. 450 ℃, 550 ℃ and 650 ℃). In addition to the final product encapsulating metal catalyst particles, the synthesized CNOs contained a number of by-products such as carbon nano-fibres and carbon nano-tubes. To overcome the problem associated with the undesired formation of carbon materials, a flame pyrolysis approach was used for the synthesis of CNOs with high purity, using grapeseed oil as a carbon source. The pristine material was annealed at different temperatures and doped with boron (B) and nitrogen (N). Physical properties of the materials were investigated and characterized by scanning electron microscopy (SEM), transmission electron microscopy (TEM), X-ray diffraction (XRD), X-ray photoelectron spectroscopy (XPS), a gas adsorption technique, Brunauer-Emmet-Teller (BET) analysis, Raman spectroscopy and thermogravimetric analysis (TGA). The results from the CVD method demonstrated a change as the temperature and flow rate increased. Microscopy analysis revealed successful dispersion of Fe and Co particles onto $CaCO_3$ which produced a mixture of materials (CNOs, CNFs and CNTs). The XRD patterns confirmed the presence of highly active crystalline mixed oxide ($CoFe_2O_4$) as the dominant catalyst phase. TEM analysis of CNOs from the flame pyrolysis method revealed multi-layered concentric carbon layers with no by-products. The amount of substitutional nitrogen in the CNO samples was 1.67% which resulted in an increase in the specific surface area and I_D/I_G ratio.

The work further explored the use of CNOs, from flame pyrolysis, as electrode materials in a two electrode system. The capacitance and resistivity of the prepared carbon electrodes were evaluated using techniques such as cyclic voltammetry (CV), galvanostatic charge-discharge (GCD) and electrochemical impedance spectroscopy (EIS).

The electrochemical performance of N-doped CNOs was investigated and compared with those of the pristine, annealed and B-doped CNOs within an operating cell potential of 0.8 V

in a 2 M KOH electrolyte. The specific capacitance increased upon nitrogen doping to 54 F/g as compared to pristine CNOs (7.5 F/g), annealed CNOs at 750 ℃ -2 h (22.5 F/g) and B-doped CNOs (28 F/g). The N-doped CNOs exhibited superior electrochemical performance compared to pristine, annealed and B-doped CNOs which was related to the high surface area and I_D/I_G ratio and indicated that the electrolyte ions could readily penetrate the pores of the electrode material. Our results demonstrated that N-doped CNOs are capable of delivering energy in a short timeframe in supercapacitors.

TABLE OF CONTENTS

DECLARATION I
DEDICATION II
ACKNOWLEDGEMENTS III
PRESENTATIONS V
ABSTRACT VI
TABLE OF CONTENTS VIII
LIST OF TABLES XV
LIST OF SYMBOLS AND ABBREVIATIONS XVI
Chapter 1: Introduction 1
1. Introduction 1
1.1 Background and motivation 1
1.2 Problem statement 2
1.3 Purpose of the study 3
1.3.1 Aims of the study 3
1.3.2 Objectives 4
1.4 Outline of the dissertation 4
1.5 References 5
Chapter 2: Literature review 5
2. Introduction 7
2.1 Background on supercapacitors 7
2.2 Energy storage mechanism of conventional capacitors and supercapacitors 9
2.2.1 Energy storage in conventional capacitors 9
2.2.2 Principle of a supercapacitor 11
2.3 Types of supercapacitors 12
2.3.1 Electric double layer capacitors 13
2.3.1.1 Properties of different types of electrolytes used in EDLCs 18
2.3.2 Energy storage in pseudocapacitors 19
2.3.3 Hybrid capacitors 20
2.4 Carbon nano-onions 21

2.4.1 Synthesis of carbon nano-onions 22
2.4.2 Doping and functionalization of CNOs 23
2.4.3. Application of CNOs in supercapacitors 25
2.5 References 26
Chapter 3: Reaction optimization studies for the Fe-Co catalysed synthesis of carbon nano-onions using a chemical vapor deposition technique 32
3. CNOs synthesised by CVD 32
3.1 Materials and Reagents 33
3.2 Preparation of the supported bimetallic catalyst (10% Fe-Co/$CaCO_3$) 33
3.3 Synthesis of CNOs using the supported bimetallic catalyst 34
3.4 Characterization techniques 34
3.4.1 Transmission electron microscopy (TEM) 34
3.4.2 Scanning electron microscopy (SEM) 35
3.4.3 X-ray diffraction (XRD) 35
3.4.4 Raman analysis 35
3.4.5 Thermal gravimetric analysis (TGA) 35
3.4.6 Brunauer-Emmett-Teller (BET) 36
3.5 Results and discussion 36
3.5.1 Morphology analysis 36
3.5.1.1 TEM analysis 36
3.5.1.2 SEM analysis 38
3.5.2 XRD 40
3.5.3 Raman spectroscopy analysis 41
3.5.4 Thermal stability 43
3.5.5 Surface area analysis 45
3.5.6 Carbon material yield 45
3.5.7 Summary of the results 46
3.6 Conclusions 47
3.7 References 49
Chapter 4: Synthesis of CNOs by flame pyrolysis 52
4. Introduction 52

4.1 Materials and reagents 53
4.2 Synthesis of CNOs using flame pyrolysis 54
4.3 Annealing of the raw soot 54
4.4 Boron doped raw soot 55
4.5 Nitrogen doped raw soot 55
4.6 Results and discussion 55
4.6.1 TEM analysis of the pristine, annealed and doped CNOs 55
4.6.2 Raman analysis of pristine, annealed and doped CNOs 58
4.6.3 XRD analysis of pristine, annealed and doped CNOs 60
4.6.4 Thermal stability of pristine and annealed CNOs 61
4.6.5 CN and XPS elemental analysis of the pristine and N-doped CNOs 64
4.7 Growth mechanism of CNOs synthesized from flame pyrolysis 68
4.8 Conclusions 69
4.9 References 70
Chapter 5: Application of CNOs using two electrode cell in 2 M KOH 73
5. Introduction 73
5. 1 Electrochemical characterization procedure 75
5.1.1 Fabrication of undoped, B-doped and N-doped CNOs electrodes in a full symmetric cell 75
5.1.2 Screening of materials using a three-electrode system 75
5.2. Two electrode measurements 76
5.3 Cyclic voltammetry (CV) analysis of the pristine and annealed CNOs 77
5.4 Cyclic voltammetry (CV) analysis of undoped, B-doped and N-doped CNOs 78
5.5 Galvanostatic charge-discharge of undoped, B-doped and N-doped CNOs 80
5.6 Electrochemical impedance spectroscopy analysis of undoped, B-doped and N-doped CNOs 82
5.7 Cyclic stability of N-doped CNOs 85
5.8 Ragone plot of undoped, B-doped and N-doped CNOs 85
5.9 Conclusions 88

5.10 References 89
Chapter 6: General conclusions and recommendations 91
6.1 Properties of CNOs synthesized from CVD method 91
6.2 Properties of CNOs synthesized from flame pyrolysis method 91
6.3 Application of CNOs in SCs 91
6.4 Recommendations 92
Appendix A: Supplementary Information 93

LIST OF FIGURES

Chapter 2

Figure 2. 1: Energy storage device generated by SOHIO in 1966 [9]. 8
Figure 2.2: Diagram showing an electrostatic capacitor [12] 9
Figure 2. 3: Different types of devices in terms of energy and power [21]. 11
Figure 2. 4: Schematic illustration of a supercapacitor [24]. 12
Figure 2. 5: Taxonomy of different types of supercapacitors and their type of materials used. 13
Figure 2. 6: (a) The Helmholtz model, (b) the Gouy-Chapman model, and (c) the Stern model [27, 28]. 14
Figure 2. 7: Schematic illustration of EDLC [30]. 15
Figure 2. 8: Schematic representation of pseudocapacitor [30]. 19
Figure 2. 9: Three types of mechanism used in pseudocapacitors [50]. 20
Figure 2. 10: Schematic representation of a hybrid capacitor [30]. 21
Figure 2. 11: High resolution TEM images of (a) nanodiamonds [80], different sizes and shapes of CNOs [65, 80] and metal encapsulated CNOs [78]. 23
Figure 2. 12: Image showing CNOs in distilled water. 24

Chapter 3

Figure 3. 1: (a-c) TEM images of sample 1 and (d-f) sample 3. 36
Figure 3. 2: (a-c) TEM images for sample 4 and (d-f) sample 5. 37
Figure 3. 3: (a, b) SEM images of sample 1. 38
Figure 3. 4: Growth mechanism of carbon nanomaterials synthesized from CVD [23]. 39
Figure 3. 5: (a-c) XRD pattern of samples 1-5. 40
Figure 3. 6: (a, b) Raman spectrum of sample 1-5. 42
Figure 3. 7: Raman spectra of samples 4 and 5. 42
Figure 3. 8: (a, b) TGA and (c, d) TGA-derivative of samples 1-5. 44

Chapter 4

Figure 4. 1: Flame pyrolysis method for synthesis of CNOs [16]. 54
Figure 4. 2: (a-c) TEM images of the pristine and (d-e) annealed CNOs at 750 ℃-2 h. 56

Figure 4. 3: Particle size distribution of pristine CNOs. 57
Figure 4. 4: (a-c) High magnification TEM images of N-doped CNOs and (d-f) B-doped CNOs 57
Figure 4. 5: (a) Raman spectra of pristine, annealed and (b) B-doped and N-doped CNOs. .. 59
Figure 4. 6: (a) XRD patterns of pristine, annealed and (b) B-doped and N-doped CNOs 61
Figure 4. 7: (a, b) TGA and (c, d) TGA-derivative plots of the pristine and annealed CNOs. 62
Figure 4. 8: (a) TGA data and (b) TGA-derivative plots for B-doped and N-doped CNOs.... 63
Figure 4. 9: XPS survey spectra of pristine and N-doped CNOs. 65
Figure 4. 10: (a) The C1s and (b) O1s deconvoluted spectra of pristine CNOs. 65
Figure 4. 11: (a) C1s, (b) O1s and (c) N1s deconvoluted spectra of N-doped CNOs. 66
Figure 4. 12: Growth mechanism of CNOs via the bottom-up approach [22]. 69

Chapter 5

Figure 5. 1: (a) T-type cell used in this study and (b) coated carbon papers (electrodes) with a separator sandwich between the two electrodes. 75
Figure 5. 2: Screening method using a three electrode system. 76
Figure 5. 3: (a) CV curves of pristine and annealed CNOs in 2 M KOH, (b) 2 M H_2SO_4 and (c) Comparison of annealed CNOs at 750 ℃ (2 h) in 2 M KOH and 2 M H_2SO_4. Scan rate: 25 mV/s using a three electrode system. 77
Figure 5. 4: Comparative cyclic voltammograms for pristine CNOs, annealed CNOs at 750 °C (2 h), B-doped CNOs and N-doped CNOs in 2 M KOH at a scan rate of 10 mV/s. 78
Figure 5. 5: (a) Comparison of cyclic voltammograms for pristine CNOs, (b) annealed CNOs at 750 °C (2 h), (c) B-doped CNOs and (d) N-doped CNOs at various scan rates in 2 M KOH. 79
Figure 5. 6: (a) Comparison of galvanostatic charge-discharge at various current densities for pristine CNOs, (b) annealed CNOs at 750 ℃ for 2 h, (c) B-doped CNOs and (d) N-doped CNOs. Electrolyte: 2 M KOH 76
Figure 5. 7: (a) Comparative GCD curves and Csp VS current density (F/g) for pristine CNOs, annealed CNOs at 750 °C-2 h, B-doped CNOs and N-doped CNOs in 2 M KOH at 0.1 A/g. 82
Figure 5. 8: (a) Nyquist plot of pristine, annealed, B-doped and N-doped CNOs after cycling with the inset representing the expanded portion of the high frequency and (b) electrical equivalent circuit (EEC) used to fit the experimental data. 83
Figure 5. 9: (a) Nyquist plots of the pristine, (b) annealed CNOs, (c) B-doped and (d) N-doped CNOs with the inset representing the expanded portion of the high frequency region before and after cycling. 84

Figure 5. 10: Cycling stability of the N-doped CNOs after 10,000 cycles. 85
Figure 5. 11: Ragone plot of pristine, annealed, B-doped and N-doped CNOs. Electrolyte: 2 M KOH electrolyte. 86

Appendix

Figure S 1: TEM images of carbon materials grown at (a-c) 650℃ (Sample 5) and (d) 550 ℃ (sample 4).....93
Figure S 2: TEM images of (a) pristine and (b) B-doped CNOs. 93
Figure S 3: Raman spectra of pristine CNOs used for determination of the FHWM. 94

LIST OF TABLES

Chapter 3

Table 3. 1: List of materials and reagents used in this study 33
Table 3. 2: Reaction conditions for synthesis of CNOs.....34
Table 3. 3: The Raman data for CNOs synthesized by CVD. 43
Table 3. 4: TGA data of the synthesized materials. 44
Table 3. 5: BET surface area of the synthesized materials (samples 1-5). 45
Table 3. 6: Percentage (%) yield of the synthesized carbon materials. 46
Table 3. 7: Summary results of the materials synthesized at different temperatures……...43

Chapter 4

Table 4. 1: Materials and reagents used in this study 53
Table 4. 2: Raman data for pristine, annealed, B-doped and N-doped CNOs.....60
Table 4. 3: Decomposition temperatures (determined by the derivative TGA) for the pristine, annealed CNOs at different temperatures and time and B-doped and N-doped CNOs.....63
Table 4. 4: CN measurements of the pristine and N-doped CNOs.....64
Table 4. 5: XPS component peak positions (eV). 67
Table 4. 6: Summary of % concentration of all bonds in the samples.....67
Table 4. 7: BET surface areas and pore volumes of the pristine, annealed, B-doped and N-doped CNOs. 68

Chapter 5

Table 5. 1: Specific capacitance (F/g) of the undoped, B-doped and N-doped CNOs at various current densities 81
Table 5. 2: Parameters values obtained from the experimental data fitted using EEC.....83
Table 5. 3: Summary of specific capacitance of boron and nitrogen doped carbon material together with their specific surface area and pore volume 87

LIST OF SYMBOLS AND ABBREVIATIONS

ACs	Activated carbons
AN	Acetonitrile
Ar	Argon
Au	Gold
BET	Brunauer-Emmett-Teller technique
C	Capacitance
$CaCO_3$	Calcium carbonate
Ce,sp	Gravimetric capacitance
$(CH_3O)_3B$	Trimethyl borate
Co	Cobalt
CoO	Cobalt oxide
$CoFe_2O_4$	Cobalt ferrite
$Co(NO_3)_2.6H_20$	Cobalt (II) nitrate hexahydrate
Co_3O_4	Cobalt (II, III) oxide
Cu	Copper
CNOs	Carbon nano-onions
CNTs	Carbon nano-tubes
CVD	Chemical vapour deposition
EDLCs	Electric double layer capacitances
EIS	Electric impedance spectroscopy
E_{max}	Maximum energy

F	Farads
$Fe(NO_3)_3.9H_2O$	Iron (III) nitrate nonahydrate
GCD	Galvanostatic charge-discharge
H_2	Hydrogen
HNO_3	Nitric acid
H_2SO_4	Sulphuric acid
i	Applied current
$KMnO_4$	Potassium permanganate
KOH	Potassium hydroxide
L_a	Crystallite size
Li_2SO_4	Lithium sulphate
N_2	Nitrogen
NH_3	Ammonia
PC	Propylene carbonate
Pb^{2+}	Lead
PVs	Photovoltaic cells
Q	Charge
NEC	Nippon Electric Company
SCs	Supercapacitors
SEM	Scanning electron microscopy
SOHIO	Standard Oil of Ohio
TEM	Transmission electron microscopy
TGA	Thermal gravimetric analysis

ΔV_{IR}	Voltage drop
XPS	X-ray photoelectron microscopy

Chapter 1: Introduction

1. Introduction

1.1 Background and motivation

The high energy demand in the present day is due to the population growth which affects life quality [1]. Various types of primary energy sources such as hydrocarbons are utilized daily because they are less expensive and they give high energy [2]. Non-renewable energy sources (i.e. coal) are used to supply most of the energy in the world [3, 4]. The use of fossil fuels results in generation of harmful gases resulting in a change of the world's temperature by about 1-5 degrees [5]. The environmental pollution caused by fossil fuels has resulted in research focused on renewable energy across the globe [6]. Hence, research is now focused on exploring the use of renewable energy sources since they produce less harmful gases to the environment. Renewable energy is the kind of energy that originates from normal re-established sources [7]. The penetration of renewable energy sources and other forms of potential distributed generation sources is increasing worldwide [8]. Renewable energy technology which is an alternative route for energy generations account for a little percentage in global energy supply [9, 10]. The great advantage in utilizing renewable resources (wind, hydrothermal, biomass and nuclear) is that they produce less or no waste products such as GHG or other chemical pollutants [11]. As much as the renewable energy shows to be an escalating solution to environment pollution, a key stumbling block in renewables is the difficulties in electricity storage and transmission. Grid energy storage is a critical component in the integration of renewable technology and ensuring distribution of electricity [12]. But the August 2003 blackout in the Northeast, the September 2011 power failure that extended from Southern California to Mexico and Arizona and 2020 loads shedding by ESKOM electricity grid in South Africa are more widely publicized examples in which power outages affected and still continue to affect millions of people across the globe. Electrochemical energy storages (in the form of supercapacitors) can be seen as a valuable approach for improving the reliability and overall use of the entire power system. Storage of energy in general provides us with another approach of taking the energy when is available, storing it and then feeding it into the grid or a single household when is needed. Energy storage has the

potential to change the way we live. Energy storage is considered the key element in an energy system that organizes production, consumption and transport of electricity in a smart way [13]. Storing energy allows transmission and distribution to operate at full capacity, decreasing the demand for newer or upgraded lines and increasing plant efficiencies. Storing energy for shorter periods may be useful for smoothing out small peaks and sags in voltage.

Traditionally, batteries are commonly used to store energy, however, they have many disadvantages as they take longer times to charge, they are heavy and generally contain harmful chemicals or toxic metals. Amongst available energy storage technologies, electrochemical capacitors are preferred energy storing devices due to their high power, long life cycle and high reliability [14].

Energy storage in the world can be effectively overseen by the utilization of energy storage gadgets, for example, supercapacitors [15]. Supercapacitors (SCs) are electrochemical capacitors that store energy and deliver high power density in a short period of time [16]. The construction of SCs involves two electrodes immersed in an electrolyte with a separator between the electrodes to prevent electrical conduction [17]. The increase in energy demand motivates the use of carbon materials in SCs such as activated carbon (ACs), carbon nano-onions (CNOs) and carbon nanotubes (CNTs), because they are cheap, easy to synthesize and they are of high stability [18]. The unique and fascinating multi-layered properties of CNOs are observed in a nano range of 1-100 nm [19]. CNOs have been reported to give high power densities in SCs because of their high conductivity and high surface area accessibility for electrolyte ions [20]. However, CNOs gives limited amount of energy which can be improved by doping using nitrogen or boron. The heteroatom doping can also tailor the electron-donor properties of carbons and subsequently enhance their electrochemical activity [21]. Studies have demonstrated that nitrogen-doped carbons have better electronic properties than the related undoped ones [22-24].

1.2 Problem statement

Energy storage capabilities have been the subject of much research. Because many electronic devices (such as laptops computers, smartphones, and digital cameras) have been become an integral part of an increasingly more mobile man, demands for energy storage and consumption have drastically augmented. Hence, there is a need for more efficient energy storage devices in nearly every domain [25]. There is a pressing need to find an economical,

lomg-lasting and ecologically friendly way to store the energy we harness from an increasingly diverse array of sources. The development of SCs has been proposed to address some of these energy storage needs because of rapid charging/discharging and longer life cycle [26]. SCs attract much attention as a good alternative or supplement to batteries. A breakthrough took place in understanding how SCs function over the past decades [27, 28].

Two main types of SCs are electric double layer capacitors (EDLCs) with carbon electrodes and pseudocapacitors with metal-oxide or conducting polymers [29]. Carbon electrodes offer long cycle life and rapid charging, but suffer from limited volumetric capacitance [30]. Metal-oxide electrodes have higher capacitance than carbon electrodes at lower conductivities [31]. It was shown that only ruthenium oxide is he only metal-oxide with an appropriate capacitance and conductivity [32]. However, it is prohibited due to its high cost. Hence, the use of carbon electrodes such as doped CNOs may offer a viable solution of high capacitance.

1.3 Purpose of the study

1.3.1 Aims of the study

The increase in energy demand has prompted a great attention on developing excellent electrode materials for use in SCs. However, most of the materials present today still have drawbacks and hence a lot of effort has been based on improving the energy density of the materials for use in industries. The increase in energy density in SCs is often improved by increasing the pore volume of the material and improving its conductivity using dopants. The proposition for this study is that upon doping the CNOs with heteroatoms such as nitrogen and boron, there will be an increase in surface area and conductivity leading to an improvement in energy storage in SCs. The hypothesis leads to the following aim:

- To synthesize and study electrochemical properties of functionalized CNOs through incorporation of heteroatoms, in particular boron and nitrogen, to the carbon nano-onions.

1.3.2 Objectives

- To synthesize core-shell CNOs over a bimetallic catalyst using a chemical vapor deposition technique.
- To synthesize catalyst free CNOs through the flame pyrolysis technique.
- To dope CNOs with boron and nitrogen (post-doping method was explored).
- To use the synthesized materials as carbon electrode materials in a symmetric system in SCs.
- The synthesized materials was characterized using techniques such as: TEM, TGA, SEM, Raman spectroscopy, BET analysis and XPS.
- To compare the capacitance and resistivity of the obtained materials using CV, GCD and EIS.

1.4 Outline of the dissertation

This work is distributed into six chapters with **Chapter 1** incorporating the motivation of the study, aims and objectives as well as discussing the energy challenges faced in the world. This chapter also discusses the use of renewable energy sources as energy systems that are replenished and will never run out. In this section, the use of supercapacitors as electrochemical energy storage systems is taken into account.

Chapter 2 is a literature review that gives a background on electrochemistry and the three types of supercapacitors known to date. Carbon nano-onions as electrode materials in supercapacitors are discussed.

Chapter 3 discusses the results and discussion of carbon nano-onions synthesized from a chemical vapour deposition (CVD) method.

Chapter 4: This chapter entails results and discussions on the synthesis of carbon onions from flame pyrolysis.

Chapter 5: This chapter discusses the electrochemistry findings obtained from two and three electrode cells using carbon nano-onions as electrode materials.

Chapter 6: This final chapter of the dissertation gives the concluding remarks showing the importance of the study and covers the way forward with possible future work.

1.5 References

1. X. Qiu, C. Burda. *Chemical Physics* 339 (2007) 1.
2. N. Keller, N.I. Maksimova, V. V. Roddatis, M. Schur, G. Mestl, Y.V. Butenko, V.L. Kuznetso, R. Schlogl. *Angewandte Chemie International Edition* 41 (2002) 1885.
3. J. Goldmberg. *Science* 135 (2007) 808.
4. J. Chow, R.J. Kopp, P.R. Portney. *Science* 302 (2003) 1528.
5. Z. Qi, M. Gary. *Vacuum Science and Technology* 4 (2017) 2166.
6. H. Bang, A.E. Ellinger, J. Hatjimarcou, P.A. Traichal. *Physics* 17 (2000) 449.
7. K. Mazloomi, C. Chandima. *Renewable and Sustainable Energy* 16 (2012) 3024.
8. S.A. Sherif, F. Barbir., T.N. Veziroglu. Electricity 18 (2005) 62.K. Mazloomi., C. Chandima. *Renewable and Sustainable Energy* 16 (2012) 3024.
9. A. Midilli, M. Ay, I. Dincer, M.A. Rosen. *Renewable and Sustainable Energy* 9 (2005) 255.
10. D.K. Ross. *Vacuum* 80 (2006) 1084.
11. P. G. Bruce, S. A. Freunberger, L. J. Hardwick and J.M. Tarasco. *Nature Materials* 11 (2012) 19.
12. A. Kausar. *Material Science* 25 (2017) 109.
13. http://energystorage.org/energy-storage/technologies/electrochemical-capacitors (accessed 03 June 2018).
14. A. Burke, Z. Liu. H. Zhao. IEEE International Electric Vehicle Conference (IEVC). Florence, Italy: IEEE; (2014) 1.
15. F. Machado, J.P.F. Trovão, C.H. Antunes. *IEEE Transactions on Vehicular Technology* 65 (2015) 29.

16. D.Y. Qu. *Power Sources* 109 (2002) 403.

17. X. Jian, S. Liu, Y. Gao, W. Tian, Z. Jiang, X. Xiao, H. Tang, L. Yin. *Electrical Engineering* 4 (2016) 75.

18. M.S. Wang, D. Golberg, Y. Bando. *ACS Nano* 4 (2010) 4396.

19. M. E. Plonska-Brzezinska, L. Echegoyen. *Materials Chemistry A* 1 (2013) 13703.

20. J. K. McDonough; Y. Gogotsi. *The electrochemical society Interface* 3 (2013) 61.

21. J. Hao, J.Wang, S. Qin, D. Liu, Y. Li, W. Lei. *Materials Chemistry A* (2018) 8053.

22. L. Zhao, L. Fan, M. Zhou, H. Guan, S.Y. Qiao, M. Antonietti *et al*. *Advanced Materials* 22 (2010) 5202.

23. L.F. Chen, X.D. Zhang, H.W. Liang, M.G. Kong, Q.F. Guan, P. Chen *et al*. *ACS Nano* 6 (2012) 7092.

24. Q. Shi, R.Y. Zhang, Y.Y. Lv, Y.H. Deng, A.A. Elzatahrya, D.Y. Zhao. *Carbon* 84 (2015) 335.

25. K.F. Jensen, W. Kern.Thin Film Processes, New York, Academic Press (1991).

26. M.E. Glavin, P.K.W. Chan, S. Armstrong, W.G. Hurley. A stand –alone photovoltaic supercapacitor battery hybrid energy storage system. 13th Power Electronic Motion Control Conference, EPE-PEMC Pozma, Poland (2008).

27. B. Conway. Electrochemical supercapacitors: scientific fundamentals and technological applications. New York: Kluwer/Plenum, (1999).

28. Y.A. Maletin, N.G. Strizhakova, V.Y. Izotov, A.A. Mironova, S.G. Kozachkov, V.V. Danilin, T. Ekstrom. Supercapacitor stacks of high energy and power density. Florida, USA, (1997).

29. P.R. Bueno. *Power Sources* 414 (2019) 420.

30. A. Burke. *Power Source* 91 (2000) 37.

31. R.Kotz, M. Carlen. *Electrochimica Acta* 45 (2000) 2483.

32. I.H. Kim, K.B. Kim. *Elecrochemical and Solid State Letters* 4 (2001) 62.

Chapter 2: Literature review

2. Introduction

The energy storage in supercapacitors (SCs) requires materials that have both high conductivity and high surface area to be able to conduct electrolyte ions rapidly and accommodate them in large pores. Carbon materials are the main focus in SCs because they are cheaper and their surface area can be improved by functionalization or adding heteroatoms, such as boron or nitrogen, to improve the conductivity [1]. Carbon nano-onions (CNOs) are materials that are applied in energy storage in SCs together with different materials, for example, activated carbons (ACs), carbon aerogels and carbon nanotubes (CNTs). ACs are among the greatest popular carbon materials applied in electric double layer capacitances (EDLCs). This is mainly due to their high surface area (500 to 2000 m^2/g) produced in the carbon material after activation [2, 3]. However, only a fraction of the surface area can contribute to the capacitance because only the mesopores (2-50 nm) can be accessible, while the micropores (< 2 nm) are inaccessible, for diffusion of electrolyte ions [4]. The low amount of energy is due to the inaccessibility of the micropores [5]. The capacitance that arises from pristine CNTs is low unless a pseudocapacitive component such as manganese oxide is added to enhance capacitance of CNTs [6]. As a result, CNOs were the material of choice in our study, because their outer surface area is accessible for diffusion of electrolyte ions which gives them a high-power density.

This chapter will present the background on SCs and the different types of SCs. Different types of electrolytes are also discussed. This chapter also entails the discussion of CNOs as electrode materials in SCs. It will help to understand the necessity of using CNOs as electrode materials in SCs and how to enhance their conductivity by doping with various heteroatoms (i.e. nitrogen and boron).

2.1 Background on supercapacitors

The perceptions made by rubbing an amber with fur was created by researchers in the eighteenth century for the improvement of the idea of electric charge [7]. The development of

the principal capacitor named Leyden container began in the year 1746 [8]. The structure of the Leyden container included two foils (inward and external) associated with an electrostatic generator utilized as a source of power [9]. However, the volume of the Leyden jar was too big, hence it was reduced to a flat capacitor so it could be more reliable and easier to work with. The capacitor still had problems associated with electric charges which were later resolved by Michael Faraday using the Helmholtz process [10]. This led to the invention of high powered capacitors years later, due to the progress made by Faraday. The unit farad (F) as described in **equation 2.1** was then established as a measurement of capacitance in the field of electricity [10].

SCs then became popular as devices that store energy, delivering high power in a period of short time. SCs store larger amounts of energy than conventional capacitors because of their high capacitance. Among the different types of SCs, an EDLC was the first capacitor manufactured and licenced by Standard Oil of Ohio (SOHIO) at the Nippon Electric Company (NEC) (**Figure 2.1)** [11]. The high power of SCs led to developments in energy technology. Because of the fast charging rate and high power densities, SCs became useful in the electronics industries for use in mobile phones, cameras and electric hybrid cars [12, 13].

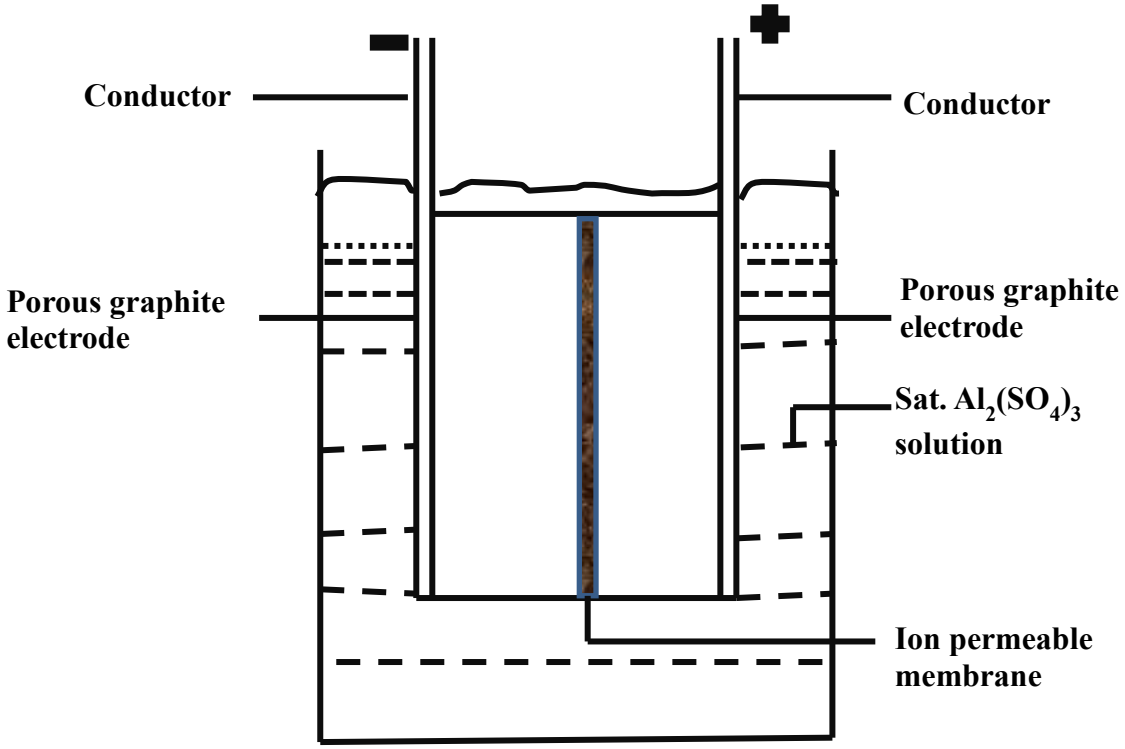


Figure 2. 1: Energy storage device generated by SOHIO in 1966 [11].

2.2 Energy storage mechanism of conventional capacitors and supercapacitors

SCs are electrochemical energy storage devices comprising of a cathode and anode. The amount of energy is stored by diffusion of the electrolyte ions to the electrode material upon charging the system.

The increase in population rate resulted in an increase in people using transportation that involve the use of fossil fuels which deteriorates the environment. Hence, SCs as renewable energy storage devices are employed to provide energy for transportation in vehicles such as buses that need fast charging and to reduce greenhouse emissions. Based on the understanding above, systems that provide a high amount of energy are required. This then led to the development of pseudocapacitors and hybrid capacitors. The difference between capacitors and SCs lies in the amount of energy and power delivered per mass. The working mechanisms of the conventional capacitors and SCs are described below.

2.2.1 Energy storage in conventional capacitors

Conventional capacitors store energy via electrostatic interaction. Capacitors that are available up to date have similar designs with two conductive electrodes separated by dielectric materials such as plastics, glass, ceramic etc. (**Figure 2.2**) [14].

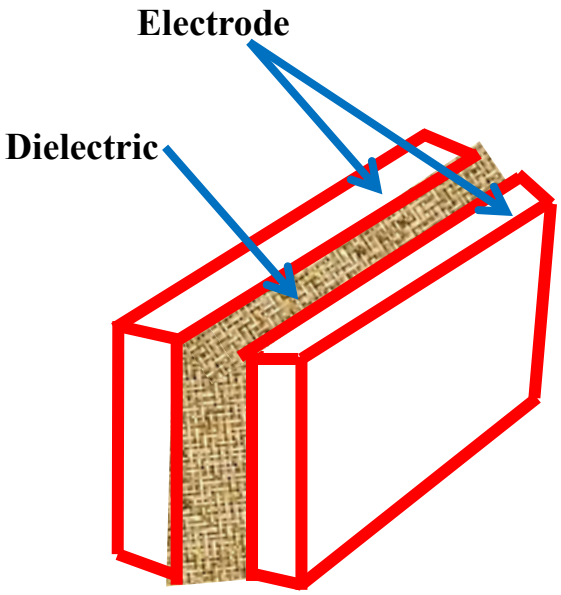


Figure 2.2: Diagram showing an electrostatic capacitor [14]

In operation, a potential is applied across the two electrodes. The two electrodes then become positively and negatively charged causing movement of opposite charged electrolytes towards them. This led to energy storage due to the movement of opposite charge across the two electrodes [14]. Hence, the energy storage arises from a capacitance that is calculated using the following equation [15]:

$$C = \frac{Q}{V} \qquad \text{eqn 2.1}$$

The capacitance is represented by C in Farads, Q (C) is the stored charge and V (V) is the applied voltage.

Equation 2.2 is used to calculate the capacitance C that arises from conventional capacitors [16]:

$$C = \varepsilon_o \varepsilon_r \frac{A}{D} \qquad \text{eqn 2.2}$$

where A (m^2/g) is the surface area of individually cathode and anode material, D (m) speaks to the separation between the materials, ε_0 is the dielectric steady of free space ($F.m^{-1}$), and ε_r is the constant of the insulating material between the cathode and anode material. Capacitance and the separation distance are inversely proportional as shown in **equation 2.2**.

The two principles that are generally utilized in capacitors are energy and power density. The following **equation 2.3** is used to calculate the energy density E of a capacitor:

$$E = \frac{1}{2} C V^2 \qquad \text{eqn 2.3}$$

Equation 2.3 shows that energy is directly proportional to capacitance.

The power density is calculated using **equation 2.4**. It is mainly affected by the equivalent series resistance (ESR). ESR is indirectly proportional to the power P. This shows that a small ESR which is contributed by internal components such as current collectors, electrodes and dielectric materials results in a high-power density. Hence, internal resistance in a circuit should be avoided to give a high-power density of the material. Thus, the maximum power (P_{max}) in SCs is calculated using the equation below [17-19]:

$$P_{max} = \frac{V^2}{4 \times ESR} \qquad \text{eqn 2.4}$$

The bridging gap between capacitors, SCs, batteries and fuel cells lies in the amount of energy stored and power delivered in a specific period of time (**Figure 2.3**) [20]. In addition,

batteries can store more energy than a conventional capacitor/SCs, however, it can't convey the stored energy in a short time frame which is one of the disadvantages of using a battery when more power density is required in a short period of time [21, 22]. The lower energy densities of SCs limit them for applications where high energy is needed. However, the greater power density that is delivered by SCs makes them attractive for application where high power in a short time is required [23].

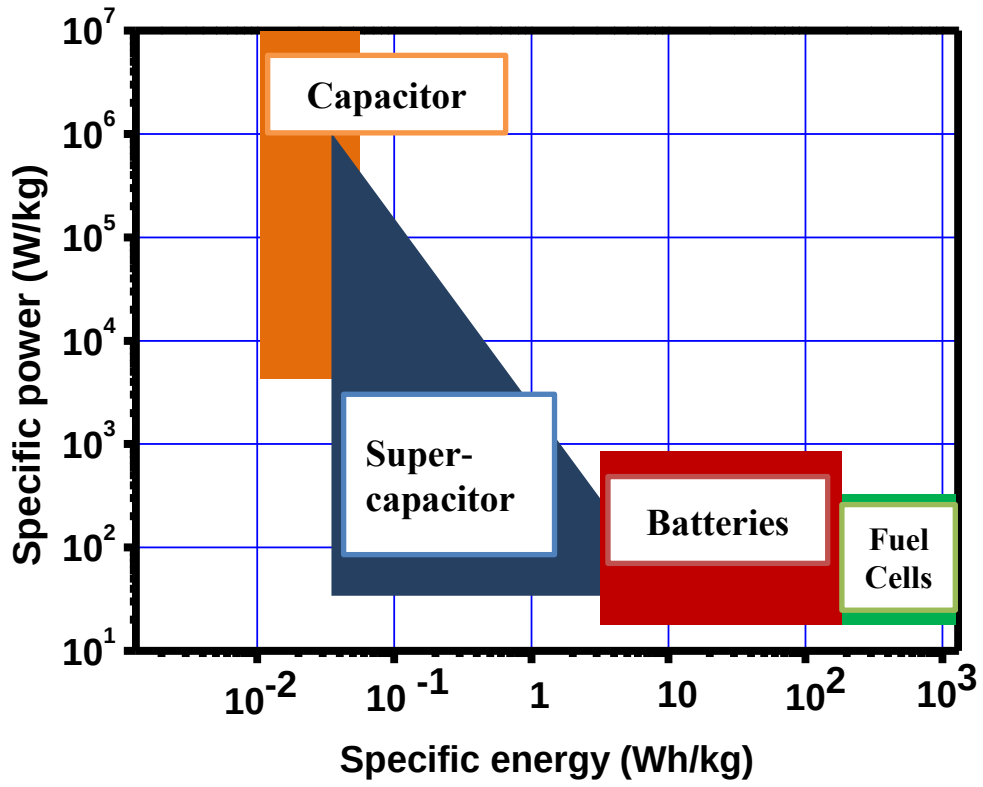


Figure 2. 3: Different types of devices in terms of energy and power [24].

2.2.2 Principle of a supercapacitor

The difference between SCs and conventional capacitors lies in the amount of energy stored which comes from the high surface area of the materials used in SCs. Hence, the capacitance and amount of energy calculated both from **equation 2.2** and **2.3** are high in SCs as compared to conventional capacitors [25]. The design shown in **Figure 2.4** is of SCs and it involves two electrodes submerged into an electrolyte solution of a certain concentration. At the point

when a potential is applied over the anode and cathode, one becomes positively charged and one negatively charged with the membrane preventing the relocation of electrolyte ions [26]. Besides the prevention of the relocation of electrolyte ions, the membrane also helps to prevent an electrical short circuit when operating the SCs system. The electrolyte ions then migrate to the charged electrode surface resulting in energy storage. The current collector (black line) helps to reduce the internal resistance of the SCs system [27]. In summary, all parameters represented in **Figure 2.4** show a significant part in the conductivity, internal resistance and the amount of energy that is stored.

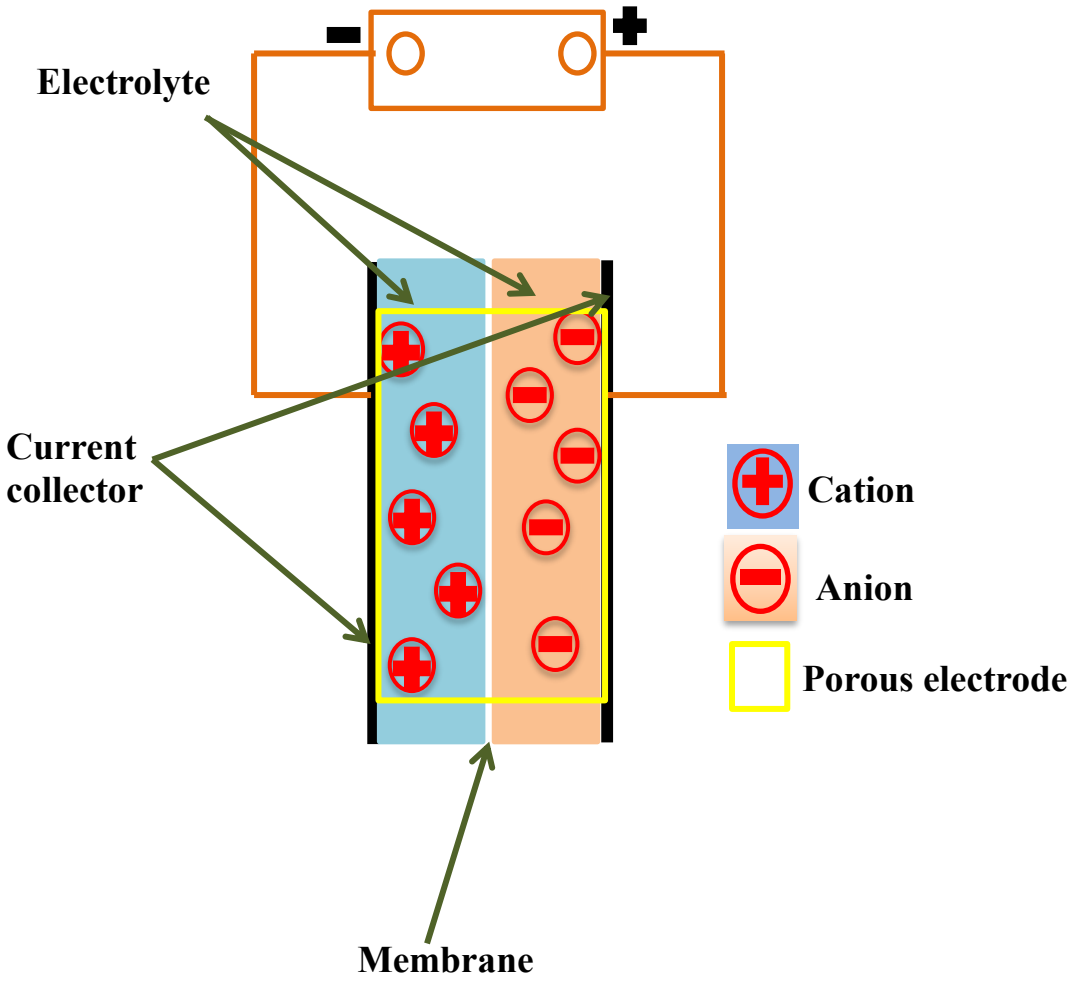


Figure 2. 4: Schematic illustration of a supercapacitor [28].

2.3 Types of supercapacitors

The three common types of SCs used in the energy sectors are: (i) electric double layer capacitors (EDLCs), (ii) pseudocapacitors and (iii) hybrid capacitors (**Figure 2.5**) with

different types of materials used in each type of SCs. The difference in the three groups lies in their energy storage mechanism and the type of materials used. The EDLCs store energy through the surface assimilation of electrolyte ions inside the pores of the anode and cathode materials while the pseudocapacitors store vitality by means of the quick Farad redox responses at the cathode and anode materials [29]. Hybrid capacitors store energy by combining both the mechanisms of the EDLCs and pseudocapacitor (Faradaic and non-Faradaic) using materials such as metal oxides and carbon materials [30].

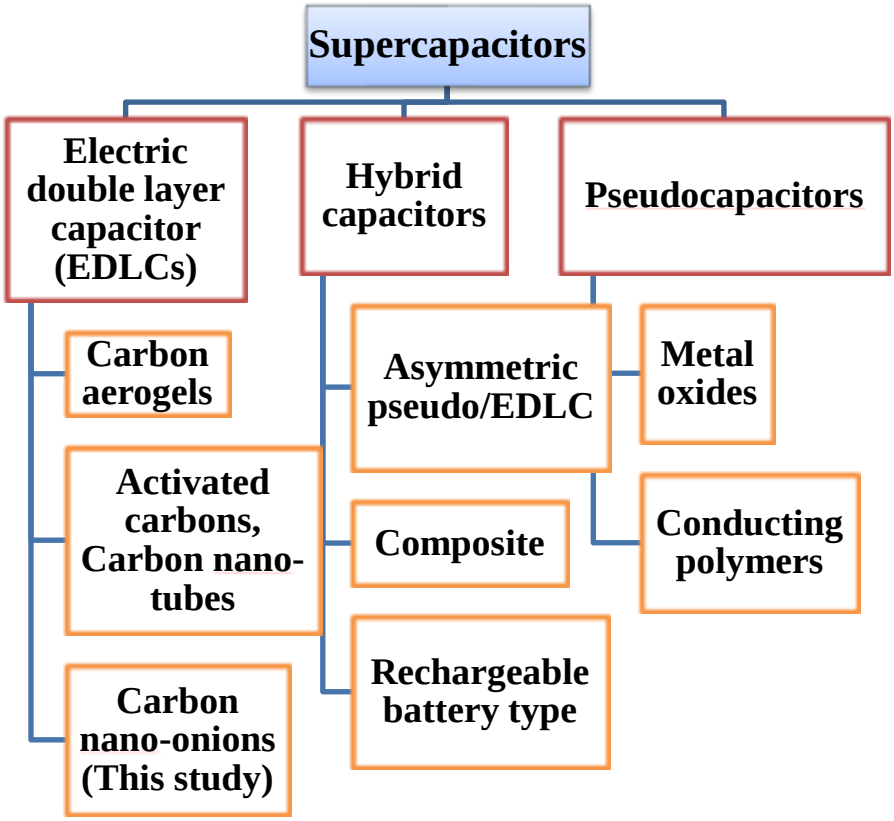


Figure 2. 5: Taxonomy of different types of supercapacitors and their type of materials used.

2.3.1 Electric double layer capacitors

Electric double layer capacitors (EDLCs) consist of two electrodes that are positively and negatively charged when voltage is applied across them. When a potential is applied through the cell, electrolyte ions migrate to the electrode surface forming a double layer. The accumulation of the electrolyte ions at the carbon electrode surface results in energy storage.

Thus, a material of high surface area is required in SCs [31]. Separators are selected dependending on the specific electrolyte for that reaction. For example, successful operation of SCs requires a separator that is electrochemically inert and highly thermal stable at the working temperature to avoid resistance occurring in the cell. The Hemholtz model is used to explain what happens to charge separation at the surface of the electrode material (**Figure 2.6a**) [32]. Since capacitance is mostly influenced by the applied voltage and concentration of the electrolyte, Gouy and Chapman autonomously settled EDLCs with the expectation of movement of free electrolyte ions (see **Figure 2.6b**) [33]. The inner and outer region of ion distribution was then combined by Stern using the two models (Helmholtz and Gouy-Chapman) as shown in **Figure 2.6c** [34]. The Stern layer represents particles' limited size and subsequently a particle's nearest way to deal with the electrode is on the request for the ionic range.

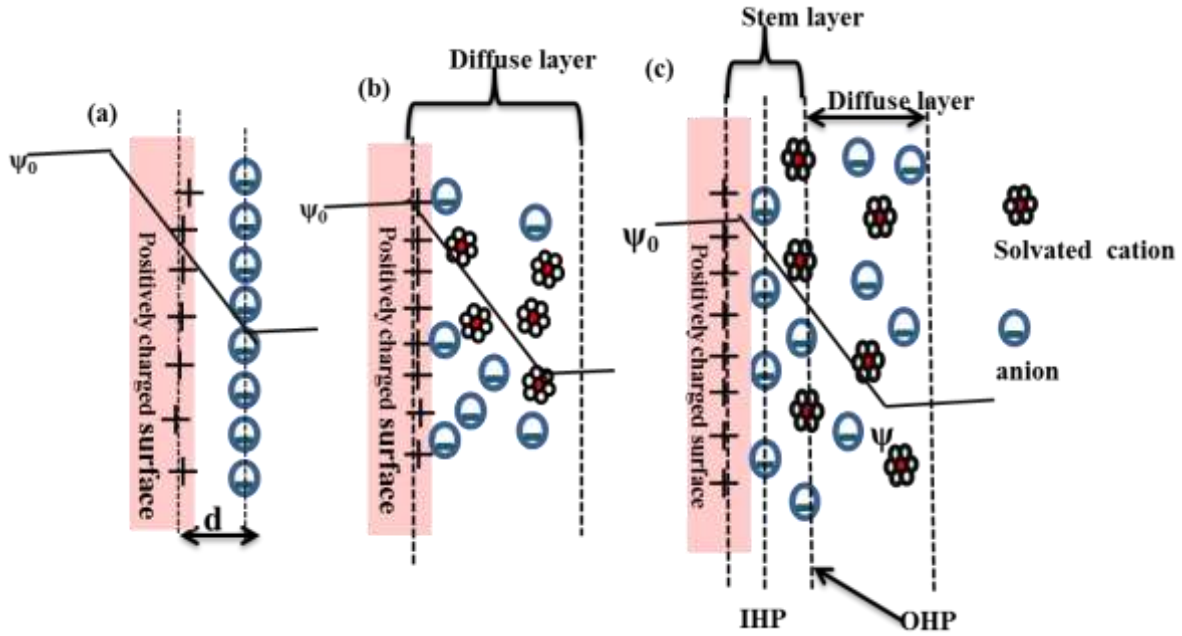


Figure 2. 6: (a) The Helmholtz model, (b) the Gouy-Chapman model, and (c) the Stern model [32, 33].

EDLCs utilize cathode and anode materials that have the same properties isolated by a separator submerged in an electrolyte (i.e. porous carbon material as shown in **Figure 2.7**). **Equation 2.5** is used to calculate the total capacitance of the positive (C_+) and negative

electrode (C_-). Since the C_+ and C_- are of the same material, the total capacitance is then equal the addition of the capacitance at each electrode as shown in **equation 2.5** [34].

$$\frac{1}{C_{cell}} = \frac{1}{C_+} + \frac{1}{C_-} \qquad \text{eqn 2.5}$$

where C_+ is the capacitance of the positive electrode material, C_- is the capacitance of the negative electrode material, and C_{cell} is the total capacitance of the positive and negative electrode in Farads (F).

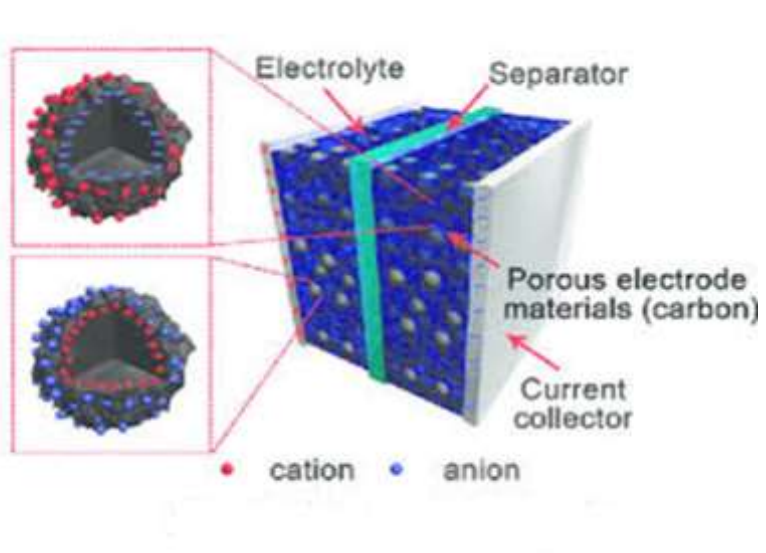


Figure 2. 7: Schematic illustration of EDLC [35].

There are two types of techniques used to calculate capacitance; cyclic voltammetry (CV) and galcanostatic charge-discharge (GCD). In a system where a full symmetric device is used, capacitance of a single electrode is calculated using the **equation 2.6 [36]**:

$$\frac{1}{C_{cell}}\ (F) = \frac{i}{\Delta v/\Delta t} \qquad \text{eqn 2.6}$$

where $i\ (A)$ is the current applied in a full symmetric device and $\Delta V/\Delta t\ (\frac{V}{s})$ is the difference in the discharge time.

Equation 2.7 is used to calculate the capacitance of a cell (C_{cell}) where the cathode and anode materials are of the same material ($C_+ = C_-$) [36],

$$C_{cell} = \frac{C_e}{2} \qquad \text{eqn 2.7}$$

where $C_e = C_+ = C_-$

Equation 2.8 is used to calculate the capacitance of the electrode [36]:

$$C_e = 2C_{cell} \qquad \text{eqn 2.8}$$

From the galvanostatic charge-discharge, the gravimetric capacitance ($C_{e,sp}$ (F/g)) of a single electrode is calculated using the following **equation 2.9 [36]**:

$$C_{e,sp}\,(\text{F/g}) = \frac{2C_{cell}}{m_e} \qquad \text{eqn 2.9}$$

where the capacitance and mass of one electrode are represented by $C_{e,sp}$ (F/g) and m_e (g).

The specific gravimetric capacitance C_{sp} (F/g) (**equation 2.10**) can be calculated from a symmetric cell where the materials coated on the anode and cathode are of the same chemical and physical properties and of the same amount [36].

$$C_{sp} = \frac{4C_{cell}}{M} \qquad \text{eqn 2.10}$$

The overall mass M (g) exists as the combination of each mass of the two electrodes (i.e. $M = 2m_e$) [37, 38]. This equation suggests that capacitance is inversely proportional to mass, hence mass loading of the active material plays a big significant part in SCs. Less mass loading of the active material leads to a higher capacitance. Not only does mass loading show an imperative part in SCs, the diffusion of electrolyte ions into the surface of the electrode materials is also vital in an application. Hence, it is essential to counterpart both the sizes of the electrolyte ion and that of the pores of the electrode material as to obtain high capacitance.

Thus, how a device delivers energy in a specific period of time has prompted research in determining two parameters in the energy sector; energy and power density [39]. Energy is

directly proportional to capacitance and inversely proportional to mass as shown by the following **equation 2.11** [40]:

$$E_{sp}(\text{Wh/kg}) = \frac{C_{cell}V^2}{2M} \qquad \text{eqn 2.11}$$

where the mass of the electrode material is represented by M (kg) and the maximum voltage is V (V). **Equation 2.11** shows that increasing both the capacitance and voltage is important for an increase in energy density.

The following **equation 2.12** is used to calculate the maximum specific power (W/kg) [41]:

$$P_{max}(\text{W/kg}) = \frac{V^2}{4ESRM} \qquad \text{eqn 2.12}$$

Voltage drop is an important parameter that is considered when calculating power density. Voltage drop (ΔV_{IR}) is observed at the start of the discharge curve from a galvanostatic charge-discharge curve. It occurs mainly from the internal resistance and it is used to calculate the ESR presented in the following **equation 2.13 [42]**:

$$\text{ESR } (\Omega) = \frac{\Delta V_{IR}}{2i} \qquad \text{eqn 2.13}$$

Equation 2.14 and **2.15** represented below are used to explain the principle of movement of ions in EDLCs when charging and discharging [43]:

On the positive electrode:

Charging process: $E_{s1} + A^- \longrightarrow E_{s1}^+//A^- + e^-$ eqn 2.14

Discharging process: $E_{s1}^+//A^- + e^- \longrightarrow E_{s1} + A^-$ eqn 2.15

On the negative electrode:

Charging process: $E_{s2} + C^+ \longrightarrow E_{s2}^+//C^+$ eqn 2.16

Discharging process: $E_{s2}^+//C^+ \longrightarrow E_{s2} + C^+ + e^-$ eqn 2.17

The overall reaction that occurs on the positive and negative electrode is summarized as follows:

Charging process: $E_{s1} + E_{s2} + A^- + C^+ \longrightarrow E_{s1}//A^- + E_{s2}//C^+$ eqn 2.18

Discharging process: $E_{s1}//A^- + E_{s2}//C^+ \longrightarrow E_{s1} + E_{s2} + A^- + C^+$ eqn 2.19

where E_{S1} and E_{S2} are the first and second electrodes at the positive and negative electrodes. A^- is the negatively charged electrolyte ion and C^+ is the positively charged electrolyte ion and the sign // represents the interface between the surface of the electrodes and the electrolyte ions.

Upon charging the system in SCs, negatively and positively charged electrolyte ions (A^- and C^+) move towards the oppositely charged electrode materials (E_{S1} and E_{S2}). The double layer is developed // and it is caused by movement of positive and negative charges of the electrolyte ions to opposite charges on the electrode materials when the system is charged. When the system is discharged, the electrolyte ions (A^- and C^+) detach from the interface // [43, 44].

2.3.1.1 Properties of different types of electrolytes used in EDLCs

Three primary classes of electrolyte solutions have been used in EDLCs: aqueous, organic, and ionic liquid (IL) electrolytes [45]. All the three electrolytes mentioned above have different ionic conductivity and operate at different voltages. Hence, their usage in different applications depends on their ionic conductivity and stability window [45]. For example, the amount of energy that is stored when using aqueous electrolytes (KOH and H_2SO_4) is low as compared to organic liquids since they operate at lower voltages (~1 V) despite their greater conductivity [46]. However, the amount of energy stored using H_2SO_4 can be higher when the potential is amplified to 1.6 V [47]. However, the major disadvantage of using acid media as an electrolyte in SCs is corrosion. Luckily, the corrosive problems faced with acid media based electrolytes can be minimized by using electrolytes that have a neutral pH (i.e. Na_2SO_4 and Li_2SO_4) [48, 49]. The use of organic liquid electrolytes offers an increased amount of energy since they operate at higher voltages (2.7-2.8 V) despite their lower conductivity [50]. Moreover, their increased amount of energy makes them applicable commercially where a high amount of energy is needed. Electrolytes prepared with propylene carbonate (PC) and

acetonitrile (AN) are also applicable in SCs, but PC is more temperature sensitive than AN [51, 52].

2.3.2 Pseudocapacitors

The lower energy storage in EDLCs is mainly due to the lower operating voltage. Thus, the amount of energy stored can be increased by adding a pseuodcapacitor material and by using redox-active electrolytes [53]. Redox-active electrolytes can also be used to improve the energy storage since they contain various oxidation states (e.g., iodine, bromine, hydroquinones) that serves as the main source of capacitance [54-57]. This is possible through Faradaic reactions [58]. However, pseudocapacitors have lower capacitance retentions after long cycling as compared to EDLCs. The difference between EDLCs and pseudocapacitors lies in the energy storage mechanisms and the type of material used [59]. The high capacitance in pseuodocapacitors results in an increase in energy storage due to the storage mechanism of two different materials of high surface areas (**Figure 2.8**) [35, 60].

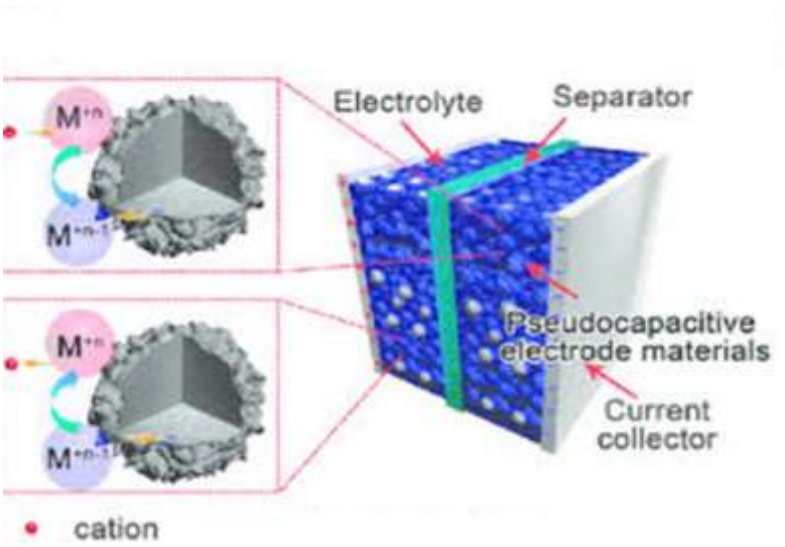


Figure 2. 8: Schematic representation of pseudocapacitor [35].

There are three mechanisms by which electrolyte ions diffuse into the pores of electrode materials in pseudocapacitors such as: (a) Underpotential mechanism, (b) Redox mechanism and (c) Intercalation of ions (**Figure 2.9**).

(a) Underpotential mechanism is a process whereby lead (Pb^{2+}) ions adsorb on the surface of gold (Au) potential more positive than the balance (Nernst) potential for the decrease of this metal (see **Figure 2.9a**).

(b) Redox mechanism involves ion adsorption process resulting in electron transfer between the species involved (e.g. storage of hydrogen with hydrated RuO_2 as shown in **Figure 2.9b**).

(c) Intercalation of ions is a process whereby electrolyte ions move between the pores on a surface region followed by adsorption on the surface (e.g. diffusion of electrolyte Li ions on the surface of a host material. such as Nb_2O_5, as shown in **Figure 2.9c**).

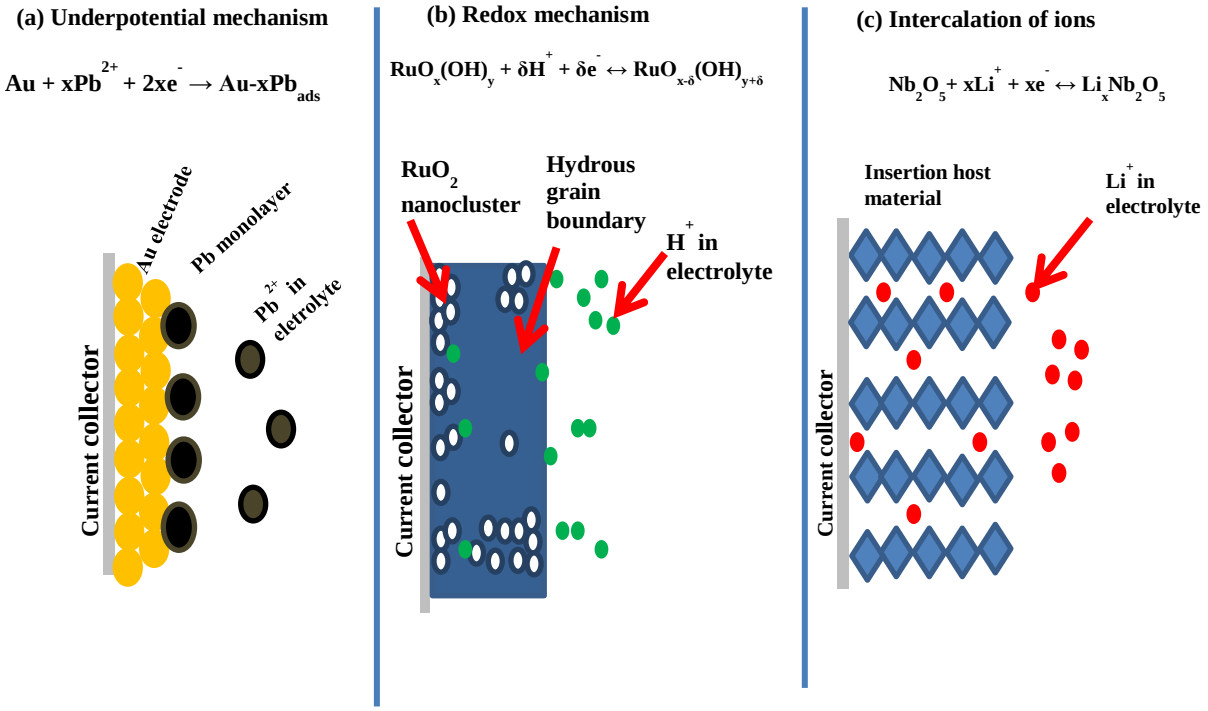


Figure 2. 9: Three types of mechanism used in pseudocapacitors [61].

2.3.3 Hybrid capacitors

Hybrid capacitors store energy by using the EDLCs and pseudocapacitor mechanism of faradaic and non-faradaic processes as shown in **Figure 2.10**. **Figure 2.10** describes the intercalation of a battery type material with EDLCs material. The activated carbon serves as

the positive electrode with graphite doped with Li-ions as the negative electrode [35, 62]. Both are submerged in an electrolyte solution (see **Figure 2.10**). There is no contact between the positive and negative electrodes because of a separator that prevents electrical contact. The amount of energy stored in hybrid capacitors is high because it involves cathode and anode materials that are different in conductivity, surface area, and stability which offers them greater advantages. Hence, most devices are built as hybrid capacitors due to their longer life cycle, high stability, high voltage, high capacitance etc. [62].

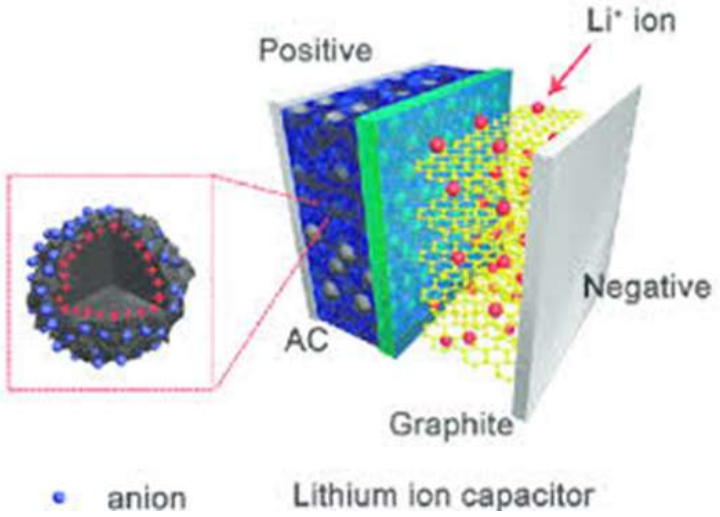


Figure 2. 10: Schematic representation of a hybrid capacitor [35].

2.4 Carbon nano-onions

Carbon nano-onions (CNOs) form part of the new carbon materials that have recently been prepared with unique physicochemical properties [63-66]. CNOs have fascinating features such as multi-layered carbon rings that are quasi-spherical in shape, resembling that of an onion. Attributable to their special physical and chemical properties, CNOs are suitable for application in electrochemical energy storage devices [67], hydrogen storage [68], magnetic fluids [69], sensing [70], plant productivity [71] and environment remediation [72]. CNOs are the electrode material of choice used in this study owing to their accessible outer surface area which delivers great power, high stability, high conductivity and pores which are able to

accommodate different sizes of electrolyte ions [73]. In addition, the electrochemical properties of CNOs can be tuned by doping.

2.4.1 Synthesis of carbon nano-onions

Production of CNOs can be accomplished using distinctive kind of strategies, for example, thermal annealing of nano diamonds [74], arc-discharge [75, 76], pyrolysis [77], ion implantation [78] and chemical vapour deposition (CVD) [79, 80]. The most used strategy for synthesis of CNOs is thermal annealing of nano-diamonds since it yields enormous amounts of CNOs with a yield near 100 % [81]. Notwithstanding, the technique is impeded because of the significant expense and that the strategy is used at moderately high temperatures. Arc-discharge is also one of the methods proposed by Sano *et al.* [82] for production of hollow core CNOs that have diameters between 15-20 nm as shown in **Figure 2.11d** [83]. The ion implantation method is likewise among the well-known techniques utilized for production of CNOs [84-86]. Creation of CNOs at high temperature using low ion implantation brings about disordered CNOs that are small in sizes [87]. Different synthetic methods to produce CNOs results in CNOs with different shapes and sizes of the onion like structure (**Figure 2.11**). Generation of CNOs from CVD is additionally viewed as a promising strategy [88]. The CVD method involves the use of a carbon source which is introduced inside a quartz tube containing a catalyst in order to promote growth of CNOs inside the furnace resulting in onion like structures with particle sizes ranging from 5 and 50 nm as shown in **Figure 2.11f**. However, CNOs synthesized from CVD requires purification steps involving harsh chemicals for removal of the catalyst [89].

Recently, a flame pyrolysis technique for the production of carbon nano-materials has been generally investigated because of its points of interest over the other generation strategies that use complicated setups and high temperatures. CNOs produced from the flame pyrolysis method have multiple layers connected to each other forming a partially spherical shape. Flame pyrolysis is a low cost method that is used to produce CNOs that do need purification steps because the material produced is not contaminated of other forms of carbon [90]. CNOs synthesized from the flame pyrolysis method are highly stable with no by-products [90]. Their structure can be modified by functionalization and doping to improve their conductivity. It was reported that a conductive carbon material is required in energy storage because it leads to high capacitance values improving the amount of energy storage [91].

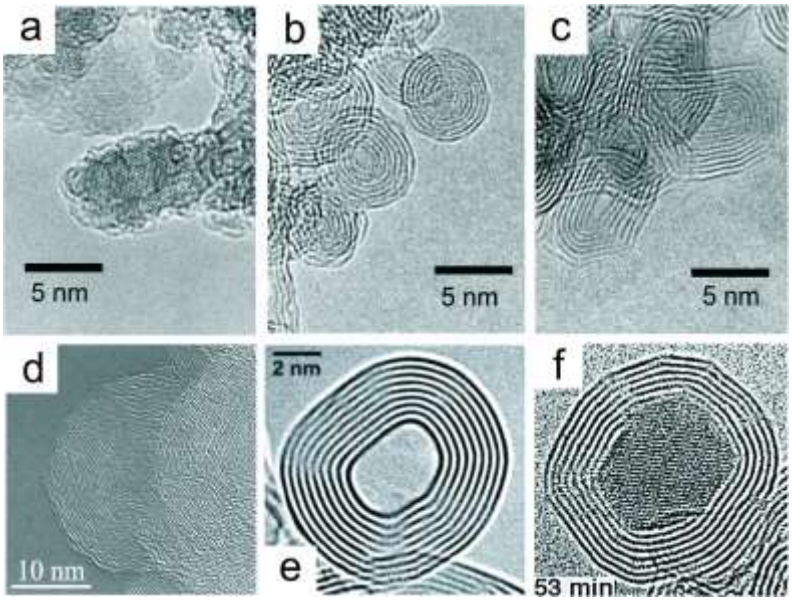


Figure 2. 11: High resolution TEM images of (a) nanodiamonds [92], (b-d) different sizes and shapes of CNOs [76, 91] and (e) metal encapsulated CNOs [89].

CNOs obtained from different synthetic procedures show that the materials are mostly full of defects with graphitic rings that are not perfectly enclosed [93]. Thus, CNOs can differ in the arrangement of the spherical carbon rings.

This study is mainly focused on the growth of CNOs using CVD and flame pyrolysis methods, and once made, their application in energy storage. CNOs have been applied before in SCs for energy storage [94, 95]. The electrochemical properties of CNOs have been reported in 2007 by Portet *et al* [73]. The CNOs delivered a high power density of 63 kW/kg with maximum specific capacitance of 40 and 30 F/g at low and high current density respectively [75]. Tthe pristine CNOs gave a low capacitance which requires functionalization or doping of the material.

2.4.2 Doping and functionalization of CNOs

CNOs are attractive carbon materials to use for energy storage in SCs due to their outer accessible surface area, high conductivity and high stability [96]. However, their hydrophobic nature limits their commercial utilization. CNOs can be made to be hydrophobic as shown in **Figure 2.12**.

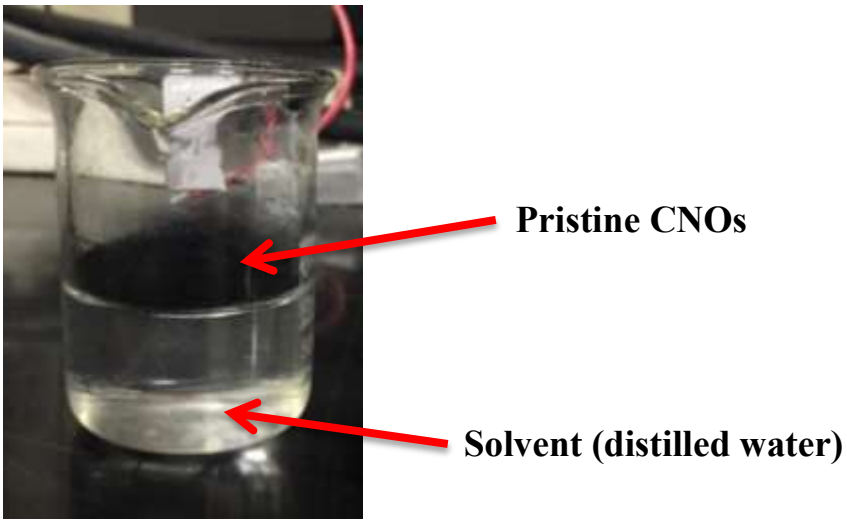


Figure 2. 12: Image showing CNOs in distilled water.

Hence, their hydrophobic nature can be overcome by introducing oxygen functional groups. The original structure of CNOs can be maintained by modification of non-covalent adsorption on the surface by using surfactants, polymers or biological macromolecules [97]. Oxygen functional groups can be introduced on CNOs by using chemicals such as HNO_3, $KMnO_4$, H_2SO_4 or a mixture of HNO_3 and H_2SO_4 98].

The presence of CNOs synthesized from the CVD method is mostly removed using harsh chemicals such as nitric acid [98]. However, it is rather difficult to remove the catalyst enclosed by carbon layers because this process disrupts the carbon layers changing the structure of CNOs thus increasing the resistivity of the material [99]. The increase in resistivity results in a smaller amount of energy stored in SCs [99].

Different dopants have been utilized to improve the amount of energy storage in SCs by tuning their electrochemical properties without altering the structure of the carbon material [100]. This can overcome the problem associated with resistivity [100]. The atomic size and mass of carbon is near to that of boron and nitrogen atoms making them appropriate among various dopants to replace carbon atoms in a structure [101]. The three valence electrons of boron make it an electron acceptor thus increasing the number of holes, which shifts the Fermi level to the valence band [102]. This process results in an improvement in conductivity of carbon materials [103]. Nitrogen has five valence electrons and it can act as electron donor by bonding with the four electrons of carbon leaving one electron which is free to move around. This process causes a change in the Fermi level thereby increasing the conductivity

[104]. Nitrogen is also known to increase the basicity of carbon materials thus improving the dispersion of CNOs in various solvents [105]. The presence of both boron and nitrogen in a carbon matrix can improve the electrochemical properties of CNOs [106, 107]. Since the specific capacitance obtained using CNOs raw soot is low, the material could be doped with various dopants to improve the specific capacitance leading to an increased amount of energy being stored.

2.4.3. Application of CNOs in supercapacitors

As mentioned, application of CNOs from flame pyrolysis and annealing of nano-diamonds in SCs has been widely studied for energy storage due to their high surface area and that they can accommodate different sized ion [108]. To the best of our knowledge, there are no reports based on application of CNOs synthesized from CVD because the mechanics of carbon nanotube and carbon onion nucleation and growth involve very complex and diverse phenomena occurring under extreme conditions and on the microcosmic scale, which still remains an open question. CNOs from annealing of nano-diamonds have been used as an electrode material in EDLCs since 2006. The type of electrolyte used were aqueous and organic [109]. The use of CNOs in SCs can be achieved in a wider temperature range (from -50 ℃ to 100 ℃) than other porous activated carbon materials which offers them better advantages where high temperatures, to operate SCs, are required [110]. Several studies have been conducted on SCs using CNOs [111, 112]. Mykhailiv *et al.* [111] reported a capacitance value of 20 F/g using onion-like-carbon annealed at 1650 ℃ in 1 M H_2SO_4 electrolyte. The capacitance decreased upon nitrogen doping giving 17 F/g as the capacitance value. CNOs were also doped with boron of different concentrations resulting in capacitance values of less than 31 F/g in a full symmetric cell [112]. The nitrogen and boron doped CNOs mentioned above differ from the doped CNOs reported in this study in terms of the type of methods used for the synthesis of pristine and doped CNOs, and the boron and nitrogen sources used. In this study, CNOs were synthesized via CVD and flame pyrolysis methods. Doping was conducted at lower temperature as compared to the high temperatures reported for doping of the CNOs from thermal annealing of nanodiamonds.

2.5 References

1. M. S. Halper, J. C. Ellenbogen. Supercapacitors: A Brief Overview, MITRE (2006).
2. D. Qu. *Power Sources* 109 (2002) 403.
3. J.A. Fernández, T. Morishita, M. Toyoda, M. Inagaki, F. Stoeckli, T.A. Centeno. *Power Sources* 175 (2008) 675.
4. C. Liu, Z. Yu, D. Neff, A. Zhamu, B. Z. Jang. *Nano Letters* 10 (2010) 4863.
5. A. Burke. *Electrochima Acta* 53 (2007) 1083.
6. H. Pan, J. Li and Y. Feng. *Nanoscale Research Letters* 5 (2010) 654.
7. J. Priestley. History and present state of electricity, 2nd Edition. London United Kingdom (1769) 86.
8. C. Dorsman, C.A. Crommelin. *Janus* 46 (1957) 275.
9. J.L. Heilbron. Electricity in the 17th and 18th Centuries: A Study of Early Modern Physics. University of California Press (1979) 309.
10. F. Michael. *Philosophical Transactions of the Royal Society* 124 (1834) 77.
11. M. Endo, T. Takeda, Y.J. Kim, K. Koshiba, K. Ishii. *Carbon Science* 3 (2001) 117.
12. P. Sharma, T.S. Bhatti. *Energy Conversion Management* 51 (2010) 2901.
13. Schneuwly, R. Gallay. Proceedings PCIM2000, Nürnberg (2000) 1.
14. M. Halper, J. Ellenbogen. Supercapacitors: A brief overview (2006).
15. P. Sharma, T.S. Bhatti. *Energy Conversion Management* 51 (2010) 2901.
16. H. Becker. *Low voltage electrolytic capacitor*, US Patent 2,800,616 (1957).
17. A. Burke. *Power Sources* 91 (2000) 37.
18. B.E. Conway. Electrochemical supercapacitor: scientific fundamentals and technological applications, New York (1999).
19. A. Chu, P. Braatz. *Power Sources* 112 (2002) 236.
20. P.S. Guin, S. Das, P.C. Mandal. *Electrochemistry* 23 (2011) 345.
21. P. P. Barker, R.W. De Mello. *Power Engineering Society* 3 (2000) 1645.
22. M.K. Kazimierczuk, R.C. Cravens. *Power Electronics* 1 (1996) 23.
23. J.R. Miller, A.F. Burke. *The Electrochemical Society's Interface* 17 (2008) 53.
24. C. Thomas, W. Martin. *Power Sources* 91 (2011) 210.
25. Z. Tehrani, D.J. Thomas, T. Korochkina, C.O. Phillips, D. Lupo, S. Lehtimaki, J. O'Mahony, D.T. Gethin. *Energy* 118 (2016) 1313.

26. D. Qu, H. Shi. *Power Sources* 74 (1998) 99.
27. Y. Huang, Y. Li, Q. Gong, G. Zhao, P. Zheng, J. Bai, J. Gan, M. Zhao, Y. Shao, D. Wang, L. Liu et al. *ACS Applied Material and Interfaces* 10 (2018) 16572.
28. Q. Zhaoxiang, M. Gary. *Vacuum Science and Technology, nanotechnology and Microelectronics* 35 (2017) 2166.
29. S.I Candelaria, Y. Shao, W. Zhou, X. Li, J. Xiao, J.G. Zhao, Y. Wang, J. Liu, J. Li, J. Gao. *Nano Energy* 1 (2012) 195.
30. J. Liu, J. Wang, C. Xu, H. Jiang, C. Li, L. Zhang, J. Lin, Z.X. Shen. *Advanced Science* 5 (2018) 1700322.
31. M.D. Stoller, S. Park, Y. Zhu, J. An, R.S. Ruoff. *Nano Letters* 8 (2008) 3498.
32. H. Helmholtz. *Annals of Physics* 89 *(*1853) 211 .
33. G. Gouy. *Theoritical and Applied Physics* 9 (1910) 457.
34. O. Stern. *Zeitschrift für Elektrochemie and Angewandte Physikalische Chemie* 30 (1924) 508.
35. C. Zhong, Y. Deng, W. Hu, J. Qiao, L. Zhang, J. Zhang. *Chemical Society Reviews* 44 (2015) 7484.
36. M. Li, Z. Wei, L. Jian. *Materials Chemistry* 18 (2008) 2276.
37. V. Augustyn, P. Simon, B. Dunn. *Energy Environmental Science* 7 (2014) 1597.
38. K. Fic, G. Lota, M. Meller, E. Frackowiak. *Energy Environmental Science* 5 (2012) 5842.
39. M. Zhi, C. Xiang, J. Li, M. Li, N. Wu. *Nanoscale* 5 (2012) 72.
40. S. Mondal, U. Rana, S. Malik. *Chemical Communication* 51 (2015) 12365.
41. R. Kotz, M. Carlen. *Elecrochimica Acta* 45 (2000) 2483.
42. A.M.R. Amaral, A.J.M. Cardoso. Instrumentation and Measurement Technology Conf. IMTC (2006) 1820.
43. E. Frackowlak. *Chemical Physics* 15 (2007) 1774.
44. M. Zhi, C. Xiang, J. Li, M. Li, N. Wu. *Nanoscale* (2012) 72.
45. N. A. Choudhury, S. Sampath, A. K. Shukla. *Energy and Environmental* 2 (2009) 55
46. V. Ruiz, C. Blanco, E. Raymundo-Piñero, V. Khomenko , F. Béguin , R. Santamaría. *Electrochimica Acta* 52 (2007) 4969.
47. V. Khomenko, E. Raymundo-Piñero, E. Frackowiak, F. Béguin. *Applied Physics* 82 (2006) 567.
48. L. Demarconnay, E. Raymundo-Piñero, F. Béguin. *Electrochem Communication* 12 (2010**)** 1275.

49. Q.Gao, L. Demarconnay, E. Raymundo-Pinero, F. Beéguin. *Energy and Environmental Science* 5 (2012**)** 9611.
50. M. Zeiger, D. Weingarth, V. Presser. *ChemElectroChem* 2 (2015) 1117.
51. J. Gamby, P. L. Taberna, P. Simon, J. F. Fauvarque, M. Chesneau. *Power Sources* 101 (2001) 109.
52. M. Arulepp , L. Permann , J. Leis , A. Perkson , K. Rumma , A. Jänes , E. Lust , J. *Power Sources* 133 (2004**)** 320 .
53. B.E. Conway, V. Birss, J. Wojtwicz. Power Sources 66 (1977) 1.
54. P. Liu, M. Verbrugge, S. Soukiazian. *Power Sources* 156 (2006**)** 712.
55. G. Lota, K. Fic, E. Frackowiak, *Electrochemistry Communications* 13 (2011) 38.
56. S. Yamazaki, T. Ito, M. Yamagata, M. Ishikawa, Electrochimica Acta 86 (2012) 294.
57. E. Frackowiak, K. Fic, M. Meller, G. Lota. *Chemistry and Sustainability Energy & Materials* 5 (2012) 1181.
58. K. H. An, K. K. Jeon, J. K. Heo, S. C. Lim, D. J. Bae, Y. H. Lee. *Electrochemical Society* 149 (2002) 1058.
59. B.E. Conway. Electrochemical Capacitors, Springer, New York (1999).
60. J. Garthwaite. How ultracapacitors work. Accessed 30th July 2019.
61. V. Augustyn, P. Simon, B. Dunn. *Energy Environmental Science* 7 (2014) 1597.
62. A.K. Shukla, A. Banerjee, M.K. Ravikumar, A. Jalajakshi. *Electrochimica Acta* 84 (2012) 165.
63. J. Bartelmess, S. Giordani. *Nanotechnology* 5 (2014) 1980.
64. N. Sano, H. Wang, M. Chhowalla, I. Alexandrou, G.A. Amaratunga. *Nature* 414 (2001) 506.
65. M.E. Plonska-Brzezinska, L. Echegoyen. *Materials Chemistry* 1 (2013) 13703.
66. J. Bartelmess, M. Baldrighi, V. Nardone, E. Parisini, D. Buck, L. Echegoyen, S. Giordani. *Chemical European* 21 (2015) 9727.
67. A. Tyagi, K.M. Tripathi, R.K. Gupta. *Materials Chemistry* 3 (2015) 22507.
68. C. Zhang, J. Li, E. Liu, C. He, C. Shi, X. Du, R.H. Hauge, N. Zhao. *Carbon* 50 (2012) 3513.
69. Y.V. Butenko, A.K. Chakraborty, N. Peltekis, S. Krishnamurthy, V.R. Dhanak, M.R.C. Hunt, L. Siller. *Carbon* 133 (2008) 1580.
70. J.P. Bartolome, L. Echegoyen, A. Fragoso. *Analytical Chemistry* 87 (2015) 6744.
71. S.K. Sonkar, M. Roy, D.G. Babar, S. Sarkar. *Nanoscale* 4 (2012) 7670.

72. C. Sakulthaew, S.D. Comfort, C. Chokejaroenrat, X. Li, C.E. Harris. *Chemosphere* 141 (2015) 265.
73. C. Portet, G. Yushin, Y. Gogotsi. *Carbon* 13 (2007) 2511.
74. E.Koudoumas, O. Kokkinaki, M. Konstantaki, S. Couris, S. Korovin, P. Detkov, V. Pustovoi. *Chemical Physics Letters* 357 (2002) 336.
75. J. Bartelmess; S. Giordani, Beilstein. *Nanotechnology* 5 (2014) 1981.
76. X. Chen, F. Deng, J. Wang, H. Yang, G. Wu, X. Zhang, J. Peng, W. Li. *Chemical Physics Letter* 336 (2001) 201.
77. A. Monila-ontoria, M.N. Chaur, M.E. Plonska-Brzezinska, l. Echegoyen. *Chemical Communication* 49 (2013) 2406.
78. J. Wang, S. Kaskel. *Materials Chemistry* 45 (2012) 23710.
79. N. Sano, H. Wang, M. Chhowalla, I. Alexandrou, G.A.J. Amaratunga. *Nature* 414 (2001) 506.
80. V.L. Kuznetsov, A.L. Chuvilin, Y.V. Butenko, L.Y. Mal'kov, V.M. Titov. *Chemical Physics Letter* 222 (1994) 343.
81. D. Roy, M. Chhowalla, H. Wang, N. Sano, I. Alexandrou, T. Clyne, G.A. Amaratunga, *Chemical Physics Letter* 373 (2003) 52.
82. N. Sano, H. Wang, I. Alexandrou, M. Chhowalla, K.B.K. Teo, G.A.J. Amaratunga, K. Iimura, *Applied Physics* 92 (2002) 2783.
83. A. Palkar, F. Melin, C.M. Cardona, B. Elliott, A.K. Naskar, D.D. Edie, A. Kumbhar, L. Echegoyen. *Chemistry Asian* 2 (2007) 62.
84. T. Cabioc'h, M. Jaouen, J.P. Rivière, J. Delafond, G. Hug. Diamond and Related Materials 6 (1997) 261.
85. H. Abe. *Diamond and Related Materials* 10 (2001) 1201.
86. T. Cabioch, A. Kharbach, A. Le Roy, J.P. Rivière. *Chemical Physics Letters* 285 (1998) 216.
87. T. Cabioch, M. Jaouen, J.C. Girard. *Carbon* 36 (1998) 499.
88. J. Du, R. Zhao, Z. Zhu. *Physica Status Solidi* 208 (2011) 878.
89. A.G. Nasibulin, A. Moisala, D.P. Brown, D. P.; Kauppinen, E. I. Kauppinen. *Carbo*n 41 (2003) 2711.
90. W. Merchan-Merchan, A.V. Saveliev, L.A. Kennedy, A. Fridman. *Chemical Physics Letter* 20 (2002) 354.

91. G. Luo, L. Liu, J. Zhang, G. Li, B. wang, J. Zhao. *ACS Applied Materials and Interface* 5 (2013) 11184.
92. S. Tomita, T. Sakurai, H. Ohta, M. Fujii, S. Hayashi. *Chemical Physics* 114 (2001) 7477.
93. Y. Liu, L.R. Vander Wal, V.N. Khabashesku, *Chemistry of Materials* 19 (2007) 778.
94. S. Juang, Y. Myung, G.S. Das, A. Bhatnagar, j. Park, K.M. Tripathi, T. Kim. *New Journal of Chemistry* (2020)
95. Y. Gao, Y.F. Lu. *Carbon* 51 (2013) 52.
96. R. Asahi, T. Morikawa, T. Ohwaki, K. Aoki, Y. Taga. *Science* 293 (2001) 269.
97. J. Cheng, K.A.S. Fernado, L.M. Veca,Y.P. Sun, A.I. Lamond, Y.W. Lam, S.H. Cheng. *ACS Nano* 2 (2008) 2085.
98. T.G. Ros, A.J. van Dillen, J.W. Geus, D.C. Koningsberger. *Chemical Europian Journal* 8 (2002) 1151.
99. S. Horike, D. Umeyama, S. Kitagawa. *Accounts of Chemical Research* 46 (2013) 2376.
100. J. Hao, J.Wang, S. Qin, D. Liu, Y. Li, W. Lei. *Materials Chemistry A* (2018) 8053.
101. P. Rani, V.K. Jindal. *Royal Society of Chemistry Advances* 3 (2013) 802.
102. A. Marchand. *Chemistry and Physics of Carbon* 7 (1971) 155.
103. E.J. Mele, J.J. Ritsko. *Physical Review B* 24 (1981) 1000.
104. L.Q. Jiang, L. Gao. *Carbon* 41 (2003) 2923.
105. Y.H. Lee, Y.F. Lee, K.H. Chang, C.C. Hung. *Electrochemical Communication* 13 (2011) 50.
106. D. Zhong, H. Sano, Y. Uchiyama, K. Kobayashi. *Carbon* 38 (2000) 1199.
107. O. Stephan, P.M. Ajayan, C. Colliex, P. Redlich, J.M. Lambert, P. Bernier, P. Lefin. *Science* 266 (1994) 1683.
108. J.K. McDonough, A.I. Frolov, V. Presser, J. Niu, C.H. Miller, T. Ubieto, M.V. Fedorov, Y. Gogotsi. *Carbon* 50 (2012) 3298.
109. E.G. Bushueva, A.V. Okotrub, P.S. GAlkin, V.L. Kuznetsov, S.I. Moseenkov. Nanoarbon nanodimond Conf. St. Petersburg, Russ. (2006) 11.
110. J.K. McDonough, Y. Gogotsi. *Electrochemical Society Interface* 22 (2013) 61.
111. O. Mykhailiv, K. Brzezinski, B. Sulikowski, Z. Olejniczak, M. Gras, G. Lota, A. Molina-Ontoria, M. Jakubczyk, L. Echegoyen, M.E. Plonska-Brzezinska, *Chemistry A Europian Journal* 23 (2017) 7132.

112. O. Mykhailiv, H. Zubyk, K. Brzezinsk, M. Gras, G. Lota, M. Gniadek, M. Romero, L. Echegoyen, M. E. Plonska-Brzezinska. *Chemistry of Nanomaterials* 23 (2017) 7132.

Chapter 3: Reaction optimization studies for the Fe-Co catalyzed synthesis of carbon nano-onions using a chemical vapor deposition technique

3. CNOs synthesized by CVD

This chapter presents the results and discussion of carbon materials synthesized using a CVD reactor and Fe-Co supported on $CaCO_3$ as a catalyst.

Different types of carbon nano-materials have consistently been utilized as cathode and anode terminal materials for vitality stockpiling, extending from the utilization of coal as the essential energy source to the use of carbon nano-onions (CNOs) in SCs [1]. New findings on using novel carbon materials (i.e. carbon nano-tubes, graphene and CNOs) has prompted investigation connected to the energy density properties [1]. Carbon nano-onions, have stood out in energy storage because of their open surface region that makes it simple for electrolyte particles to diffuse through the carbon framework and furthermore to present dopants, for example, boron or nitrogen [2-4]. Up to now, the chemical vapour deposition (CVD) technique has been demonstrated to be an inexpensive technique for creating carbon nano materials at an enormous scale [5]. Successful synthesis of carbon products has been reported by using bimetallic alloy catalysts such as Ni–Fe, Fe–Co, M–Cu and M–Al where M represents a transition metal, etc. [6-11]. To date, CNOs have been synthesized using CVD in the existence of an unsupported bimetallic (Fe-Ni) catalyst by pyrolysis of a CH_4/N_2 mixture after the reduction of the catalyst using H_2 [12], and by the decomposition of a C_2H_2-Ar mixture over a supported Fe/NaCl catalyst [13]. In the CVD process, transition metal particles are used. The mechanism either favours the formation of CNOs or CNTs/CNFs depending on the type of catalyst, carbon source and reaction parameters such as flow rates and temperature that are used.

The metal catalyst support also plays a significant role by affecting the product formed that depends on the catalytically active centre produced on the supported catalyst. Most of the catalyst supports reported in literature (i.e. SiO_2 and Al_2O_3) have good properties such as high surface area [14, 15]. However, their removal after synthesis poses a challenge. Hence, a catalyst needs to be supported with materials that are easily removed after synthesis. For example, Fe-Co has been supported on $CaCO_3$ because it is not effective when it is used

alone without a support [16]. So far, there is no report on the synthesis of CNOs using Fe-Co/$CaCO_3$. $CaCO_3$ is mostly used to support bimetallic catalysts because it is easy to remove after synthesis using chemicals such as HNO_3 and H_2SO_4. However, the use of harsh chemical activation procedures (H_2SO_4 and KNO_3) can disrupt the carbon structure increasing the resistivity of the materials, limiting the amount of energy stored in SCs [17, 18]. Again, the resulting carbon products after acid treatment contain many defects.

In this study, we report on the synthesis of CNOs by the decomposition of acetylene and hydrogen as the carbon and hydrogen source over the supported bimetallic catalyst (Fe-Co/$CaCO_3$, respectively. Parameters such a flow rates and temperatures influence the direction of the reaction.

3.1 Materials and Reagents

Table 3. 1: List of materials and reagents used in this study

Reagents and materials	Purity and speciation	Supplier
$Fe(NO_3)_3.9H_2O$	≥ 97%	Sigma-Aldrich
$Co(NO_3)_2.6H_2O$	≥ 99.99 %	Sigma-Aldrich
$CaCO_3$	≥ 99%	Sigma-Aldrich
Acetylene, C_2H_2	≥ 99%	Afrox
Hydrogen, H_2	≥ 99%	Afrox

3.2 Preparation of the supported bimetallic catalyst (10% Fe-Co/$CaCO_3$)

The bimetallic catalyst was synthesized following a procedure reported in literature [19]. In particular, the two salts (3.62 g of $Fe(NO_3)_3.9H_2O$ and 2.47 g of $Co(NO_3)_2.6H_2O$) were mixed together in 50 mL distilled water. The blend was permitted to mix for 30 min at room temperature. Approximately 10 g $CaCO_3$ was added to the blend and mixed for an extra 60 min. The darker slurry was separated and left to dry in air for 4 h. From that point onward, it was later dried in an oven at 120 ℃ for 12 h. The product was then crushed and screened through a 150 µm sieve. The final powder was exposed to heat for 16 h at 400 °C for elimination of the nitrate decomposition products [19].

3.3 Synthesis of CNOs using the supported bimetallic catalyst

The as prepared supported bimetallic catalyst was employed in a horizontal CVD reactor for synthesis of CNOs following a procedure reported in literature [20]. About 2.0 g of the bimetallic catalyst was placed in a quartz boat in the centre of the horizontal furnace. The Fe-Co supported catalyst was pre-reduced at 450 ℃ for 1 h in a flow of hydrogen gas (100, 200 and 300 mL/min). Then the growth of CNOs was conducted at 450 ℃, 550 ℃ and 650 ℃ for 1 h by introducing a mixture of C_2H_2/H_2 at a flow rate of 100/100 ml/min in the tube furnace. The **Table 3.2** below summarizes the reaction conditions used.

Table 3. 2: Reaction conditions for synthesis of CNOs

Type of material	Reduction temperature (℃)	H_2 flow rate (100 mL/min)	C_2H_2 flow rate (100 mL/min)	Synthesis temperature (℃)
Sample 1	450	100	100	450
Sample 2	450	200	100	450
Sample 3	450	300	100	450
Sample 4	450	300	100	550
Sample 5	450	300	100	650

The different samples synthesized at different flow rates and temperatures were labelled as sample 1-5.

3.4 Characterization techniques

This section involves the basic principles of microscopic, spectroscopic and thermal techniques used for the characterization of the CNOs.

3.4.1 Transmission electron microscopy (TEM)

The morphology of the synthesized materials were conducted using transmission electron microscopy (TEM) at 120 kV using a Tecnai Spirit T12 instrument. For better visualization of the materials, the morphology was conducted using high resolution transmission electron

microscopy (HRTEM) at 200 kV (Tecnai G2 30ST). For preparation of the materials, a copper grid was used and drop casted with a slurry prepared by sonicating 0.5 mg of the carbon material in a solvent (ethanol). The copper grid was dried at room temperature prior to analysis.

3.4.2 Scanning electron microscopy (SEM)

Scanning electron microscopy (SEM) (FEI Nova 600 instrument at 30 kV) was used for viewing the morphological and structural properties of the synthesized materials. The samples were prepared by placing the material on carbon tape attached to aluminium. Gold/palladium was used for coating the sample onto the tape.

3.4.3 X-ray diffraction (XRD)

The crystallinity nature of the materials were determined using X-ray diffraction (XRD). The XRD patterns were determined on a Bruker D2 phaser, operating using Cu-Kα radiation at 30 kV and 10 mA. The XRD patterns were carried out in the range of 10-90 2θ (0.026° step).

3.4.4 Raman analysis

Raman spectrometer (micro-Raman mode; Jobin-Yvon T64000, $\lambda = 532\, nm$) was utilized for producing the Raman spectra. The focal plane of the synthesized materials was at 1.5 μm in diameter.

3.4.5 Thermal gravimetric analysis (TGA)

The thermal stability of the synthesized materials were using thermal gravimetric analysis (TGA). The stability of the materials were conducted using Thermogravimetric analyser (Perkin Elmer 6000). Prior to the analysis, the sample (10 mg) was heated in an alumina cup at a temperature starting from range of 35 °C up to a maximum of 900 °C for 90 minutes per analysis.

3.4.6 Brunauer-Emmett-Teller (BET)

The pores of the materials were determined by Brunauer-Emmett-Teller (BET) using a Micromeritics Tristar 3000. The samples were outgassed at 150 °C for 4 h. Gas sorption was performed in liquid nitrogen (-195 °C).

3.5 Results and discussion

Results and discussion of the CNOs synthesized from the supported Fe-Co/$CaCO_3$ are presented in this section.

3.5.1 Morphology analysis

3.5.1.1 TEM analysis

Figure 3.1 shows the TEM images of CNOs grown at 450 °C with different flow rates (100 and 300 mL/min). There are two forms of carbon structures (i.e. CNOs and carbon nano-fibres (CNFs) seen in **Figure 3.1a, d**.

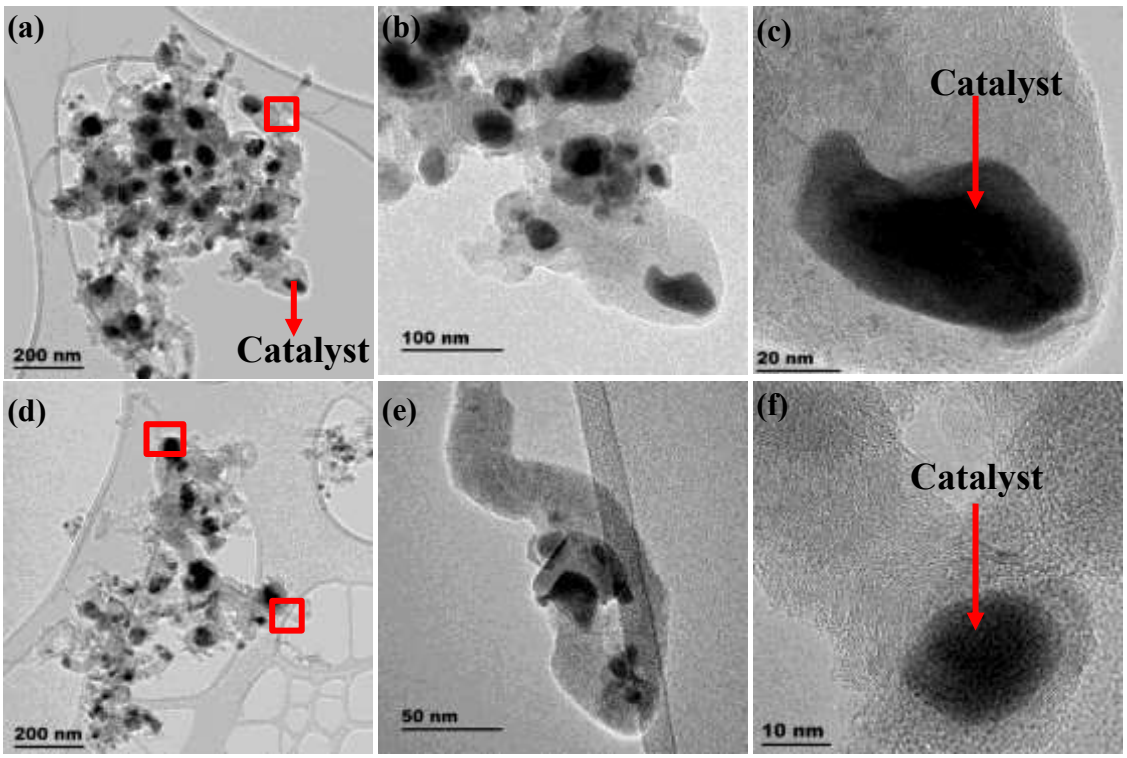


Figure 3. 1: (a-c) TEM images of sample 1 and (d-f) sample 3.

The area selected by a red frame shows that the tips of CNFs are attached to CNOs which is similar to results obtained by Zhang *et al*. [12]. It is also evident in **Figure 3.1b, c, f** that the CNOs have the metal catalyst encapsulated inside the carbon shell. The metal catalyst is encapsulated by different CNO shapes as shown in Figure 3.1b. The TEM micrographs at high magnification shown in **Figure 3.1c, f** reveal that the material has graphitic layers interconnected together resembling that one of an onion. The structure of a CNF shown in **Figure 3.1e** has a catalyst at the tip end which obviously formed from the Fe-Co/$CaCO_3$ catalyst.

An increase in temperature resulted in formation of CNTs as shown in **Figure 3.2e** (see supplementary **Figure S1a-c**). The CNTs have multiwalls as evident by the high magnification images as shown in **Figure 3.2e**. The multi-walled CNTs (MWCNTs) possess hollow and straight CNTs walls. **Figure 3.2c** shows that the CNOs synthesized at 550 ℃ have a quasi-spherical morphology with graphitic layers surrounding the catalyst (see **Figure S1d**). **Figure 3.2f** shows two typical CNOs structures; CNOs with a hollow core and the carbon made by catalyst encapsulating graphitic layers. These results are similar to what has been reported by Zhang *et al.* [12] that higher temperatures promoted the formation of MWCNTs (see **Figure 3.2e**) [12].

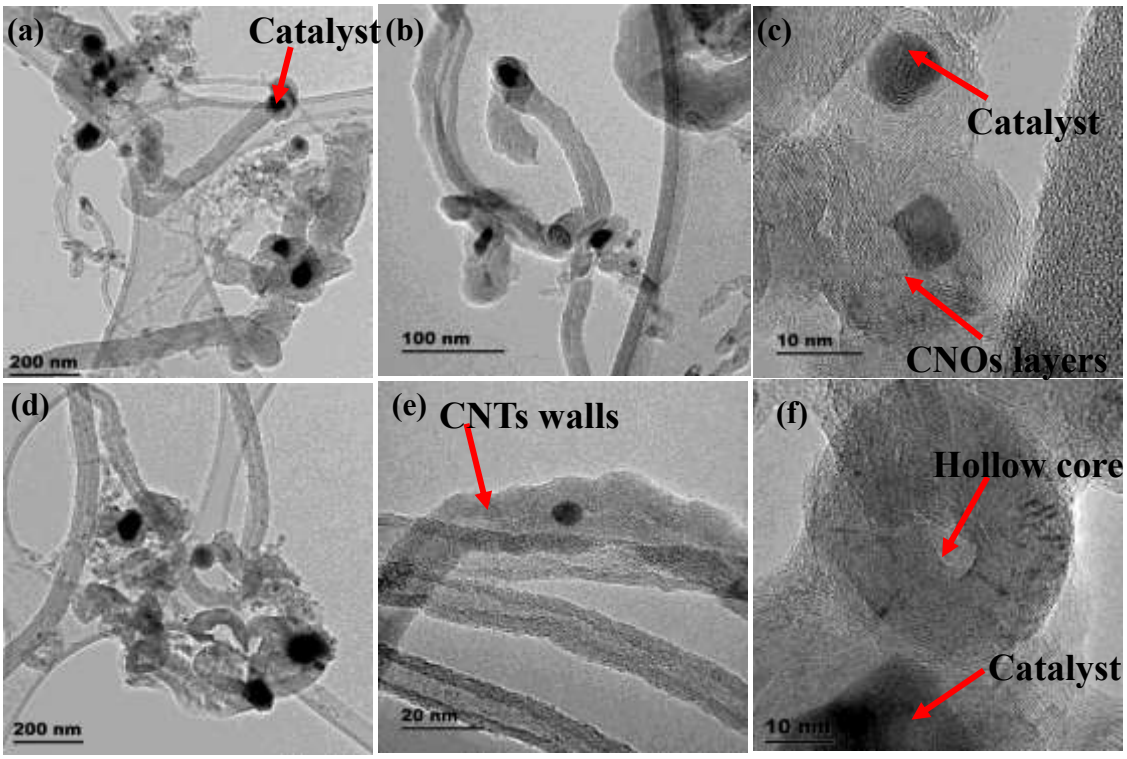


Figure 3. 2: (a-c) TEM images for sample 4 and (d-f) sample 5.

It is known that the activity of the catalysts is different in terms of their reaction temperatures [12]. Thus, at 450-650 ^{o}C, there is a formation of non-catalytic competing pathway which results in the formation of different nanostructures. These results indicate that the formation of CNOs depends on the control of the synthesis temperature. Thus, the formation of CNOs using Fe-Co/$CaCO_3$ requires growth temperatures of not greater than 650 ℃. These results show that the increase of temperature to 650 ℃ promotes the formation of MWNTs.

3.5.1.2 SEM analysis

SEM was used to study the structure of the two forms of carbon synthesized using the CVD reactor. The images in **Figure 3.3a,b** clearly show the presence of CNFs with the desired CNOs material. It is clear that these are nearly spherical shaped nanoparticles.

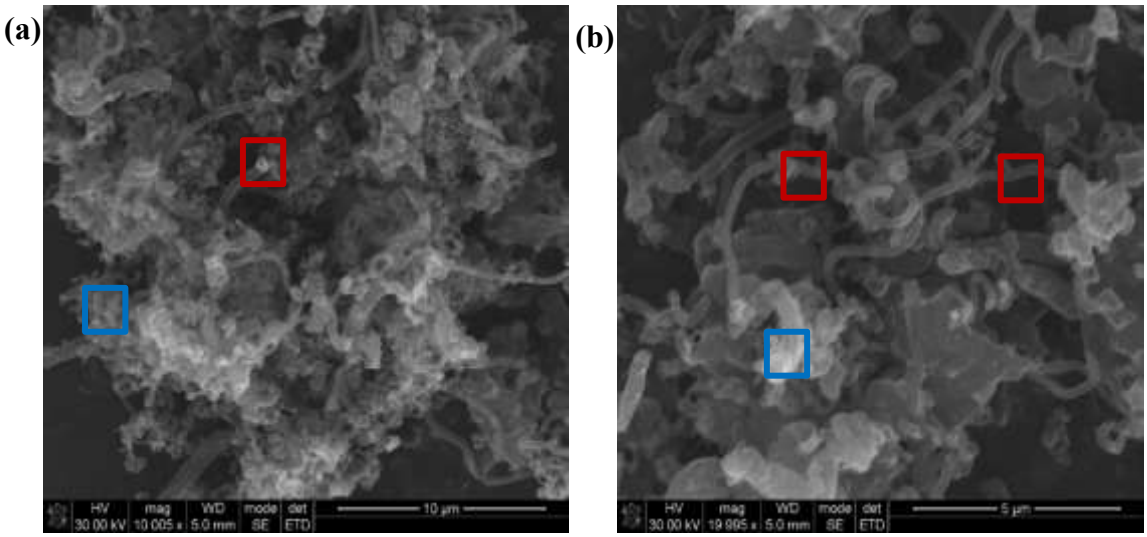


Figure 3. 3: (a, b) SEM images of sample 1.

The results also corroborate with the TEM images that there are two forms of carbon produced (CNOs and CNFs) with the base tips of CNFs interconnecting with the CNOs as shown in **Figure 3.3a, b** (red frame). Based on the results from SEM and TEM images, a proposed mechanism for the formation of the two carbons is shown in **Figure 3.4**.

Different morphologies can be obtained depending on the synthesis temperature and reduction of the catalyst. The growth mechanism follows the proposal made by Zhang and co-workers [12]. At low temperatures, the catalyst is reduced to its metal state under H_2 (g).

The introduction of the carbon source causes the dispersion of carbon atoms into the catalyst causing saturation. There is a low and high diffusion rate of carbon atoms at a temperature of 450 ℃. At a low diffusion rate, the entire catalyst is not surrounded by carbon atoms and it is oversaturated with the carbon atoms before the catalyst is filled with carbon which favours the formation of CNFs. The same mechanism occurs as the temperature increases to 550 ℃ and 650 ℃ favouring the formation of CNTs. Also, medium and high velocity movement of carbon atoms causes formation of two types of CNOs, i.e. hollow and catalyst encapsulated CNOs as shown in **Figure 3.4b, c** [21]. The CNOs with encapsulated catalyst are formed when the carbon atoms are oversaturated [21]. When carbon precipitation rates are high, the catalyst escapes from the graphitic cap before the first cap closes, therefore the new graphitic cap will connect with the first one. Therefore, CNOs form by the repetition of this process illustrated in **Figure 3.4c**.

Figure 3.4 summarizes a possible mechanism for the formation of CNFs/CNTs and CNOs. The mechanism for formation of CNFs follows the base tip growth of CNTs. CNTs develop when the tube becomes more grounded where the end tips of the nanotube connected to a catalyst are given carbon molecules [22].

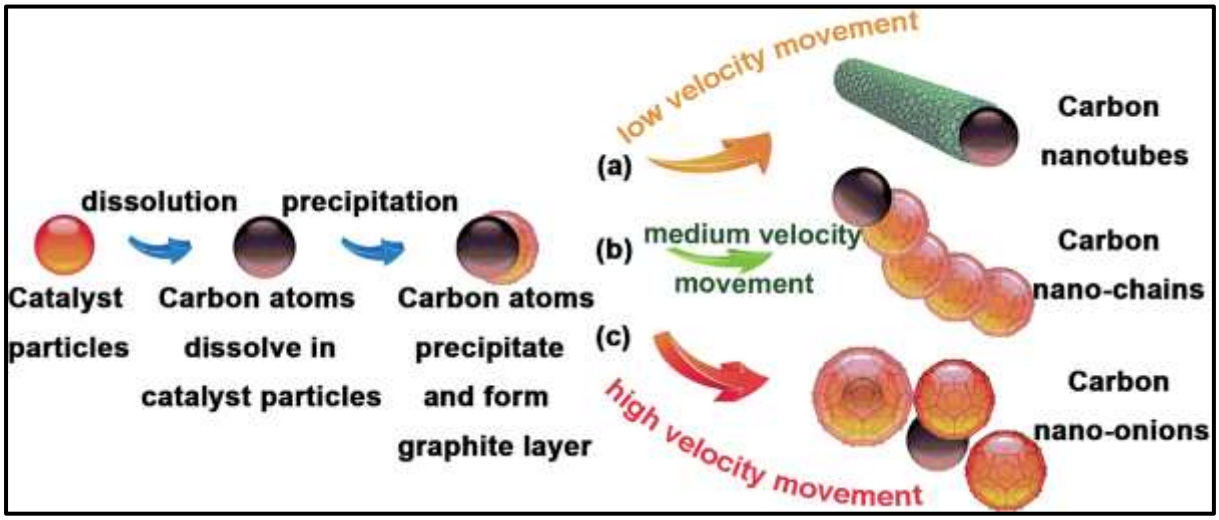


Figure 3. 4: Growth mechanism of carbon nanomaterials synthesized from CVD [23].

3.5.2 XRD

The phases present in the materials were determined from XRD measurements. The XRD data presented in **Figure 3.5a-c** show an intense peak positioned at 29-30° corresponding to the presence of $CaCO_3$ [24]. The mixed oxide phases (i.e. Fe_2O_3, CoO including $CaCO_3$ and $CoFe_2O_4$) are assigned at 2 theta value of 30-40°. During the calcination process, nitrates decompose and the metals form Fe_2O_3 and CoO. Bankole *et al*. [24] reported two main phases (i.e. $CaCO_3$ and $CoFe_2O_4$) from Fe-Co/$CaCO_3$ catalyst, which is in good agreement with the findings of the catalyst synthesized from this study. The graphite carbon at a 2 theta value close to 28° has been observed by several authors [26-01]. In this study, the (002) graphite peak was observed at 2 theta angle of 27.3^o for sample 1 as shown in **Figure 3.5a** which broadened with an increase in temperature (**Figure 3.5c**).

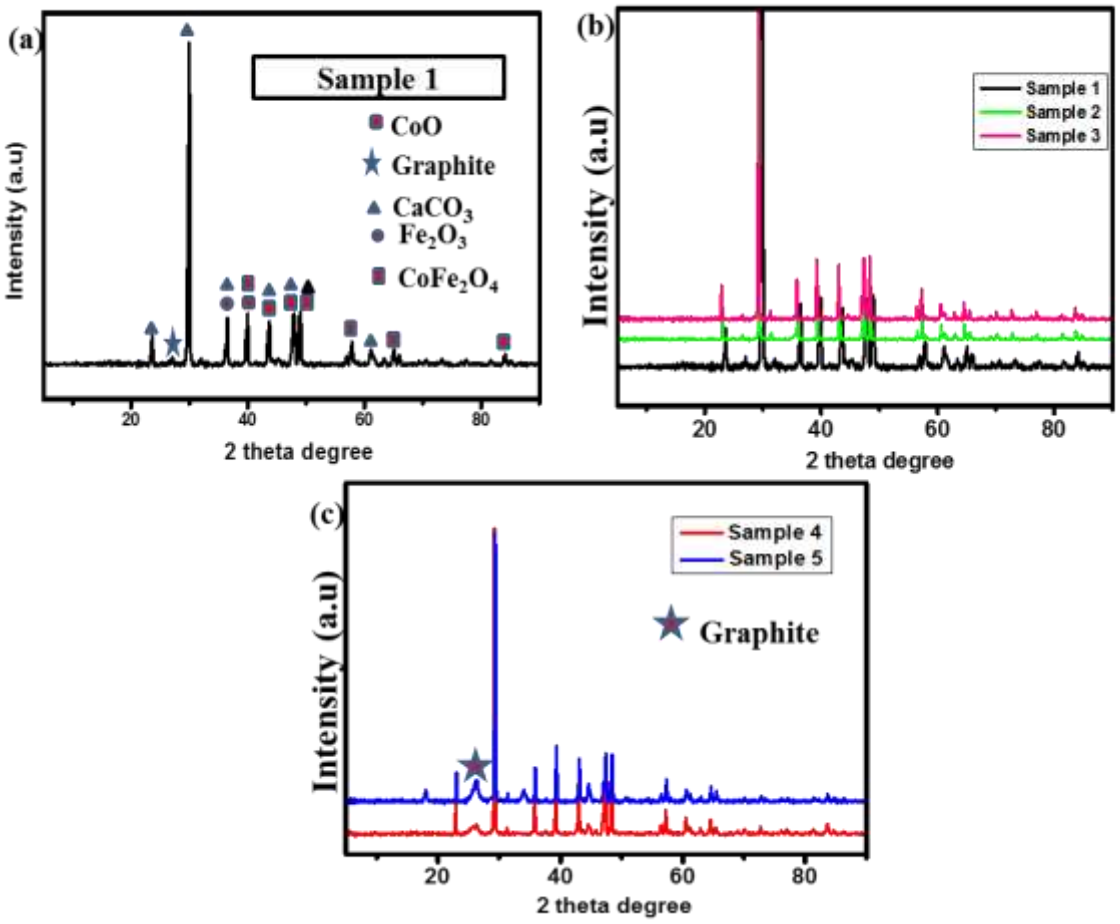


Figure 3. 5: (a-c) XRD pattern of samples 1-5.

XRD data were employed to calculate the mean crystallite sizes (D) by Debye-Scherrer's formula in the following equation [31]:

$$D = \frac{0.9\lambda}{\beta \cos\theta} \qquad \text{eqn 3.1}$$

Where D is the average crystal size, λ = 0.154 nm is the X-ray wavelength of CuKα, β is the full width of the peak measured at half maximum intensity and Θ is Bragg's angle of the peak.

One of the most important uses of XRD is ascertaining the crystalline nature of the CNOs and CNTs as opposed to amorphous carbon materials. According to the calculation, the average crystallite sizes of sample 1-5 were 28.3, 70.2, 54.1, 27.22 and 25.1 nm.

3.5.3 Raman spectroscopy analysis

The materials were analyzed using Raman spectra (**Figure 3.6** and **3.7)**. The sp^3 and sp^2 are distinguished by the D and G bands positioned at 1300 cm^{-1} and 1600 cm^{-1} [32]. Also, the defects present in the materials are distinguished by the ratio of the D and G band [32]. **Figure 3.6** illustrates the Raman spectra of carbon materials synthesized from CVD. The impurities present in the material are shown with four signals in the range 130-1100 cm^{-1}. The impurities correspond to the active Co_3O_4 modes positioned at 138.9, 268.0, 708.7 and 1079.1 cm^{-1} (**Figure 3.6a**). The medium intensity peaks located at 138.7 and 268.0 cm^{-1} correspond to the E_2g and $F_2g^{(2)}$ symmetry modes whereas the weak band positioned at 708.7 cm^{-1} has $F_2g^{(1)}$ symmetry. The octahedral sites have A_{1g} species, evident by the strong intense peak positioned at 1079.1 cm^{-1} [33]. The four peaks talked about are related with Co_3O_4 [34].

The presence of carbon in the synthesized material was confirmed by Raman peaks positioned at 1338.5 cm^{-1} (D-band) and 1583.9 cm^{-1} (G-band). The G-band is associated with sp^2 hybridized carbon and the D-band is assigned to structural defects present in the material [35, 36]. The degree of disorder in the material was measured by using the ratio of the D-band area and the G-band area. The calculated I_D/I_G ratios were 2.24, 2.33 and 2.39 for sample 1, 2 and 3, respectively (see **Table 3.3**).

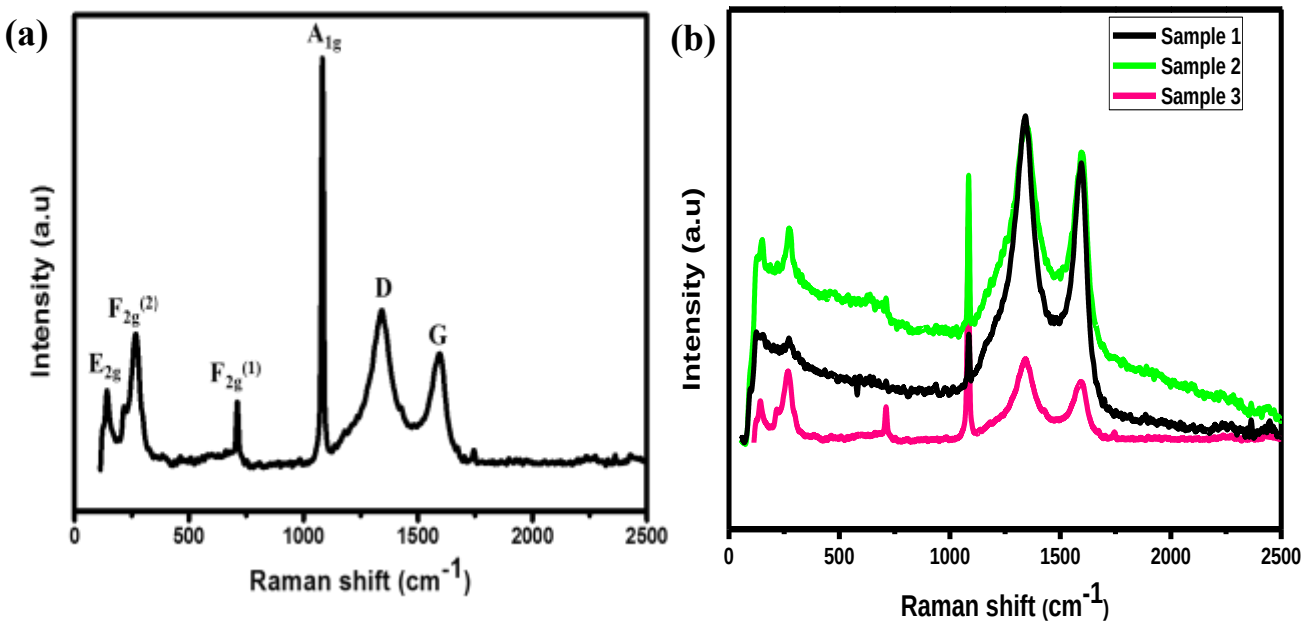


Figure 3. 6: (a, b) Raman spectrum of sample 1-5.

The area of the D-band which is associated with impurities decreased as the temperature increased from 550 ℃ and 650 ℃. Raman spectra of the CNOs synthesized at 550 ℃ and 650 ℃ (**Figure 3.7**) indicate that the value of the I_D/I_G ratio (**Table 3.3**) decreased to 1.70 (sample 4) and 0.93 (sample 5) as the synthesis temperature increased. The lowest I_D/I_G ratio for the sample synthesized at 650 ℃ indicated a lower amount of defects and improved crystallinity whereas the high I_D/I_G ratio of the samples synthesized at 450 ℃ is associated with defects caused by the disordered carbon nanostructures.

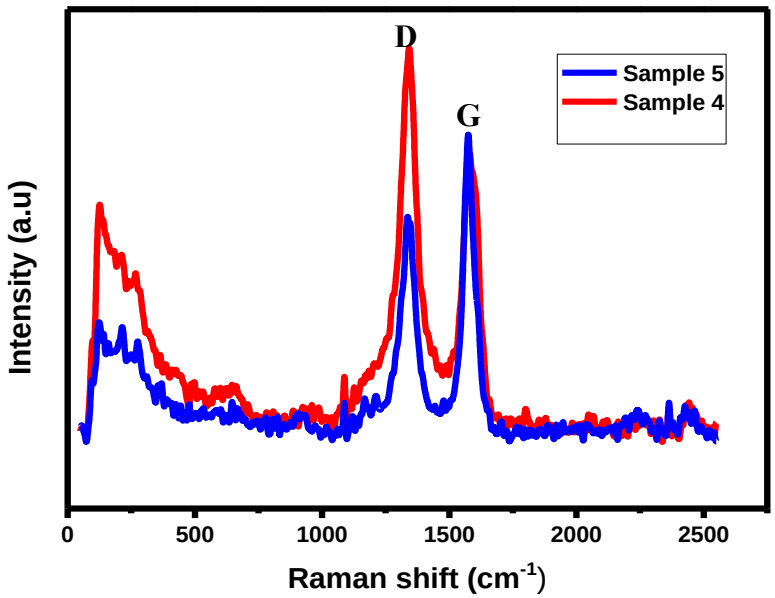


Figure 3. 7: Raman spectra of samples 4 and 5.

Table 3. 3: The Raman data for CNOs synthesized by CVD.

	D-band		G-band		
Sample type	**Raman shift (cm^{-1})**	**Area**	**Raman shift (cm^{-1})**	**Area**	**I_D/I_G**
Sample 1	1338.5	11157.3	1583.9	4976.9	2.24
Sample 2	1342.2	14272.1	1592.1	6122.3	2.33
Sample 3	1335.4	53907.1	1585.67	22553.0	2.39
Sample 4	1339.3	6804.9	1583.3	3991.7	1.70
Sample 5	1338.5	3271.0	1577.1	3535.9	0.93

3.5.4 Thermal stability

The thermal stability and purity of the synthesized material was evaluated using TGA. **Figure 3.8** depicts the TGA and derivative curve of CNOs synthesized using CVD. The maxima from the derivative curves were used to estimate the decomposition temperature. Amorphous carbon decomposes at temperatures below 400 °C [37, 38], whereas the synthesized CNOs containing a mixture of CNFs/CNTs started to decompose at a temperature above 400 °C indicating that there was no amorphous material present in the synthesized CNOs.

This is attributed to hydrogen etching of the amorphous carbon during the formation of CNOs, CNFs and CNTs. The stability of the materials depends mostly on the synthesis temperature and hydrogen gas flow rate. The thermal stability of the obtained materials changed as the flow rates changed. The prepared material (samples 1, 2, 3 and 4) show two decomposition temperatures (**Figure 3.8a,b**) while sample 5 (see **Figure 3.8b**) shows three decomposition temperatures. The incomplete oxidized metal oxide with the support was attributed at the decomposition temperature of 413-555 °C (sample 1), 425-591 ℃ (sample 2) and 422-575 ℃ (sample 3) with a weight loss of 6 %, 11 % and 8 %.

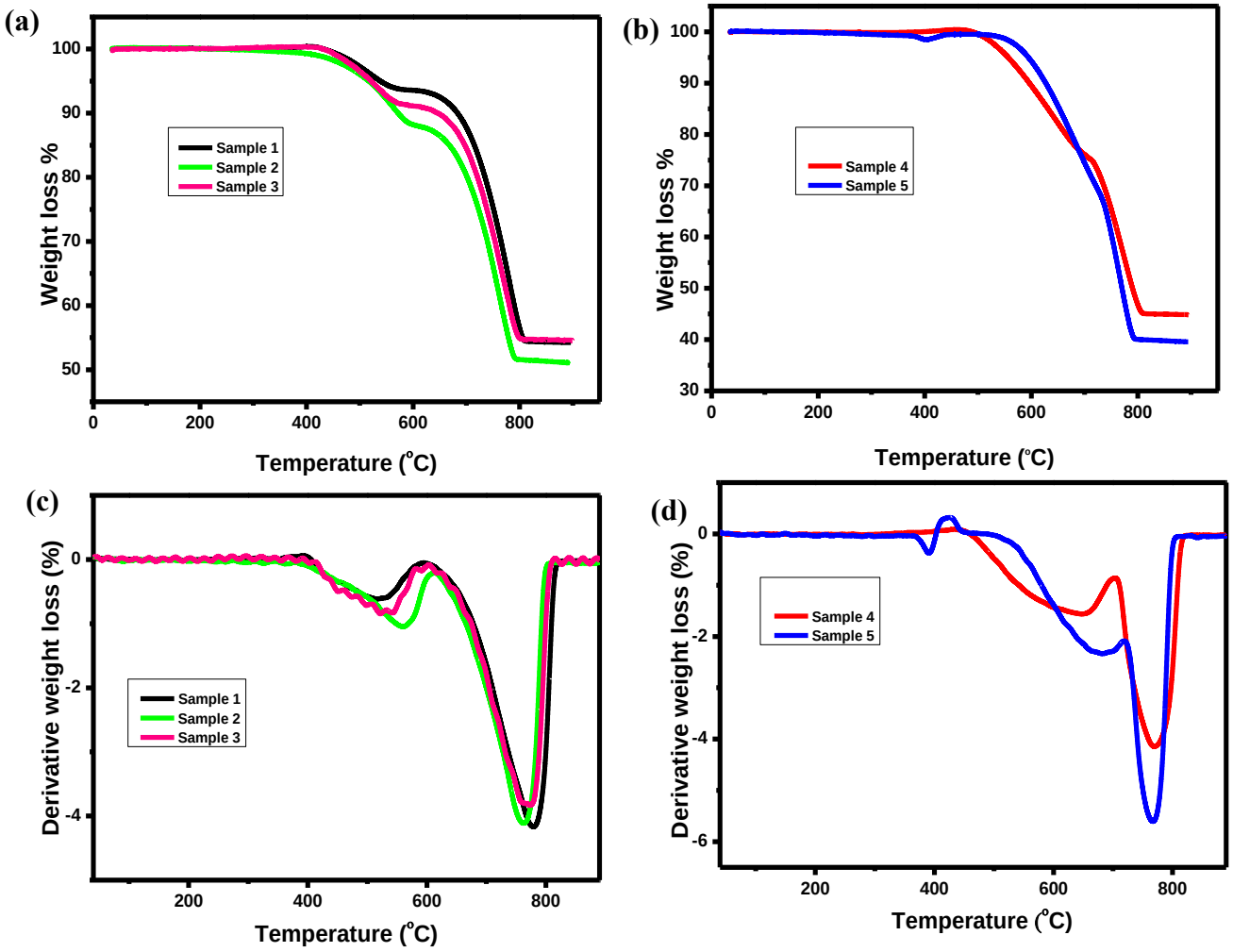


Figure 3. 8: (a, b) TGA and (c, d) TGA-derivative of samples 1-5.

The derivative peaks centered at 778 ℃, 762 ℃, 770 ℃, 770 ℃, 766 ℃ for sample 1, 2, 3, 4 and 5 respectively, can be attributed to the degradation of the outer layers of CNOs and outer shells of CNFs/MWCNTs. The remaining weight attributed to the residual catalyst and support is 54 % (sample 1), 51 % (sample 2), 55% (sample 3), 45 % (sample 4) and 48.6 % (sample 5) (see **Table 3.4**).

Table 3. 4: TGA data of the synthesized materials.

Samples	Derivative carbon decomposition temperature (℃)	Residual weight loss (%)
1	778	54
2	762	51
3	770	55
4	770	45

5	766	48

3.5.5 Surface area analysis

Table 3.5 lists the surface area, pore volume and pore sizes. The BET surface area of the materials were very low compared to carbon spheres (CSs) prepared by CVD [39]. This is due to the presence of high % of the metal catalyst supported on $CaCO_3$ confirmed by TGA and possibly due to the presence of bigger catalyst particle size as seen from the HRTEM images. The low surface areas will limit the application of the materials for use in energy storage.

Table 3. 5: BET surface area of the synthesized materials (samples 1-5).

Samples	**BET S.A (m^2/g)**	**Pore volume (cm^3/g)**	**Pore size (nm)**
Sample 1	41.0	0.08	5.5
Sample 2	13.6	0.10	28.1
Sample 3	12.9	0.08	23.9
Sample 4	28.9	0.22	29.9
Sample 5	20.6	0.12	24.6

3.5.6 Carbon material yield

CNOs were synthesized by varying parameters such as the flow rates and temperature. **Table 3.6** shows the percentage yield of the carbon materials.

Table 3. 6: Percentage (%) yield of the synthesized carbon materials.

Temperature (℃)	H_2 flow rate (mL/min)	Mass of Fe-Co/$CaCO_3$ used (g)	Mass of carbon material obtained (g)	Carbon material % yields
450	100	2	2.8	40
450	200	2	2.6	30
450	300	2	2.5	25
550	300	2	2.8	40
650	300	2	3	50

The percentage yield of the carbon materials was estimated by using **equation 3.2** [40, 41].

$$\text{Carbon material yield (\%)} = \frac{m_f - m_i}{m_i} \times 100 \qquad \text{eqn 3.2}$$

Where m_f is the total carbon material and residual catalyst obtained (g), m_i is the initial mass of the catalyst (g).

The total % yield of the synthesized materials were low which was also supported by the low specific surface area. The low % yield of the carbon material might be due to a less contact time given for the carbon material to form on the catalyst.

3.5.7 Summary of the results

This study was based on the low temperature (450 ℃) syntheses of CNOs. However, the low temperature (450 ℃) gave a mixture of carbon products. Hence, high temperatures were also investigated to check which kind of carbon products are favoured as the synthesis temperature increases (550 ℃ and 650 ℃).

Summary results obtained in **Figure 3.1-3.8** and **Table 3.3-3.4** are summarized as flows:

Table 3.7: Summary results of the materials synthesized at different temperatures.

Techniques	**Low temperature synthesis (450 ℃)**	**High temperature synthesis (550 ℃ and 650 ℃)**
TEM	Two kinds of carbon structures are formed (i.e. CNFS and CNOs).	MWCNTs started to form as a mixture of products with CNOs.
SEM	CNFs are shown to attach to the outer layers of CNOs.	-
XRD	Graphite peak is not clearly pronounced with metal active catalyst peaks present.	Graphite peaks tends to be broader and pronounced. The active faces are still of a metal catalyst.
Raman analysis	The I_D/I_G ratio is greater than 1 indicating more structural defects.	The I_D/I_G ratio at 550 ℃ is less than 1 indicating a graphitic material.
TGA	Carbon decomposition temperature occurs at low temperature with higher residual % due to the supported catalyst.	Carbon decomposition temperature occurs at high temperature with low residual % of the supported catalyst.

3.6 Conclusions

In this work, a bimetallic catalyst (Fe-Co) supported on $CaCO_3$ was synthesized, characterized and employed for the production of different carbon nanostructures. The synthesis of CNOs using a CVD method was investigated at different flow rates and temperature. The study was conducted using hydrogen gas as a reducing agent for the bimetallic catalyst. The findings from the study are summarized as follows: (i) The catalytic decomposition of acetylene over the supported catalyst at low temperature and at high temperatures formed different carbon nanostructures that encapsulated the catalyst, (ii) TEM and SEM images confirmed the formation of the two products with the tips of CNFs attached

to the CNOs, (iii) XRD revealed that the most active phase of the supported catalyst present was $CoFe_2O_4$, (iv) Raman analysis demonstrated the quality of metal encapsulated CNOs and CNFs/MWCNTs. The supported catalyst served as a growing particle for the carbon materials (CNOs and CNFs/CNTs).

However, it is clear that this method is not appropriate for making large quantities of pure CNOs. Hence, flame pyrolysis method (Chapter 4) was used for synthesis of pure CNOs.

3.7 References

1. H. C. Neto. *Materials Today* 13 (2010) 12.
2. D. Pech, M. Brunet, H. Durou, P.H. Huang, V. Mochalin, Y. Gogotsi, P. Tarbena, P. Simon. *Nature Nanotechnology* 9 (2010) 651.
3. C. Portet, G. Yushin, Y. Gogotsi. *Carbon* 13 (2007) 2511.
4. L.N. Han, X. Wei, Q.C. Zhu, S.M. Xu, K.X. Wang and J.S. Chen. *Materials Chemistry A* 4 (2016) 16698.
5. C.N. He, N.Q. Zhao, X.W. Du, C.S. Shi, J. Ding, J.J. Li *et al*. *Scripta Materialia* 4 (2006) 689.
6. W.Q. Shen, F.K. Huggins, N. Shah, G. Jacobs, Y.G. Wang, X.B. Shi. *et al*. *Applied Catalysis A : General* 1 (2008) 102.
7. N.M. Rodriguez, M.S. Kim, F. Fortin, I. Mochida and R.T.K. Baker. *Carbon* 49 (2011) 1151.
8. S. Herreyre and P. Gadelle. Carbon 2 (1995) 234.
9. M.S. Kim, N.M. Rodriguez and R.T.K. Baker RTK. *J. Catalysis* 1 (1991) 60.
10. N. Krishnankutty, N.M. Rodriguez, R.T.K. Baker. *J. Catalysis* 1 (1996) 217.
11. G.H. Luo, Z.F. Li, F. Wei, L. Xiang, X.Y. Deng and Y. Jin. *Physica B* (2002) 314.
12. C. Zhang, J. Li, C. Shi, E. Liu, X. Du, W. Feng and N. Zhao. **Carbon** 49 (2011) 1151.
13. L. Chen, C. Wang and G. Chen. *Applied Mechanics and Materials* 184 (2012) 1294.
14. S.D. Mhlanga, K.C. Mondal, R.Carter, M.J. Witcomb and N.J. Coville. *South African Journal of Chemistry* 62 (2009) 67.
15. C.J. Lee, J. Park, J.A. Yu. *Chemical Physic letters* 360 (2002) 250.
16. E. Dervishi, Z. Li, A.R. Biris, D. Lupu, S.S. Trigwell, Z.U. Rahman. *Carbon* 44 (2006) 2032.
17. M.E. Plonska-Brzezinska, J. Mazurczyk, B. Palys, J. Breczko, A. Lapinski, A.T. Dubis, L. Echegoyen. *Chemistry: A Europian Journal* 1 (2012) 2600.
18. M.E. Plonska-Brzezinska, A. Palkar, K. Winkler, L. Echegoyen. *Solid-State Letters* 13 (2010) 35.
19. A.S. Afolabi, A.S. Abdulkareem, S.D. Mhlanga, S.E. Iyuke. *NanoScience* 6 (2011) 248.
20. M.F.L. De Volder, S.H. Tawfick, R.H. Baughman, J. Hart. *Science* 339 (2013) 535.

21. J. Kang, J. Li, X. Du, C. Shi, N. Zhao, P. Nash. *Materials Science and Engineering A* 475 (2008) 136.
22. S. Amelinckx, X. Zhang, D. Bernaerts, X. Zhang, V. Ivanov, J. Nagy. *Science* 265 (1994) 635.
23. M. Zhang, N. Zhao, J. Sha, E. Liu, C. Shi, J. Lia and C. He. *Materials Chemistry A* 2 (2014) 16268.
24. S. Haffer. Mesoporous Spinel-type Cobalt Oxide, Cobalt Ferrite and Alumina by Nanocasting, PhD Thesis, Paderborn University, Paderborn (2013).
25. M.T. Bankole, I.A. Mohammed, A.S. Abdulkareem, J.O. Tijani, S.S. Ochigbo, O.K. Abubakre, A.S. Afolabi. *Journal of Alloys and Compounds* 749 (2018) 85.
26. S.D. Mhlanga, N.J. Coville. *Diamond and Related Materials* 17 (2008) 1489.
27. M.A.M. Motchelaho, H. Xiong, M. Moyo, L.L. Jewell, N.J. Coville. J. *Molecular Catalysis Chemistry* 335 (2011) 189.
28. N. Chiwaye, L.L. Jewell, D.G. Billing, D. Naidoo, M. Ncube, N.J. Coville. *Materials Research Bulletin* 56 (2014) 98.
29. Z. Li, E. Dervishi, Y. Xu, X. Ma, V. Saini, A.S. Biris. *J. Chemical Physics* 129 (2008) 747.
30. A.M. Pander, A. Hatta, H. Furuta. *Applied Surface Science* 1 (2016) 37.
31. P.Scherrer. *Mathematich-Physikalische Klasse* 2 (1918) 98.
32. F. Tuinstra, J.L. Koenig. J. *Chemical Physics* 53 (1970) 1126.
33. J. Jiang, L. Li. *Materials Letters* 6 (2007) 4894.
34. V. G. Hadjiev, M. N. Iliev, I. V. Vergilov. *J. Physical Chemistry: Solid State Physics* 21 (1988) 199.
35. C. Ferrari. Solid State Communication 143 (2007) 47.
36. M. A. Pimenta, G. Dresselhaus, M. S. Dresselhaus, L. G. Cancado, A. Jorio and R. Saito. *Chemical Physical* 9 (2007) 1276.
37. B.J. Landi, C.D. Cress, C.M. Evans, R.P. Raffaelle. *Chemistry of Materials* 17 (2005) 6819.
38. Z.J. Shi, Y.F. Lian, F.H. Liao, X.H. Zhou, Z.N. Gu, Y. Zhang, S. Iijima, H.D. Li *et al*. *Physical Chemistry* 61 (2000) 1031.
39. B.K. Mutuma, R. Rodrigues, K. Ranganathan, B. Matsoso, D. Wamwangi, I. A. Hümmelgen, N. J. Coville. *J. Materials Chemistry* 5 (2017) 2539.
40. S. Bhoware, M.S. Maubane. T. Phaahlamohlaka. A. Shaikjee, N.J. Coville. *Chemical Physics Letters* 577 (2013) 72.

41. H. Kathyayini, N. Nagaraju, A. Fonseca *et al*. *Molecular Catalysis A: Chemical* 223 (2003) 851.

Chapter 4: Synthesis of CNOs by flame pyrolysis

4. Introduction

The interesting applications of carbon materials in electrochemical energy storage [1], biomedical imaging [2], water treatment [3] etc. has prompted the large scale preparation of these materials. Carbon nano-onions (CNOs) have a multi-layered structure with unique physical and chemical properties [4]. The multi-layered structure of the carbon resembles that of onions, thus the origin of the name, carbon nano-onions. The structure of the multi-layered onion is observed in a nano-range, usually less than 100 nm [5]. The generation of CNOs in the 1980's was hard to accomplish in high yield, for the most part since they were seen with different types of carbon, for example, carbon black [6]. The formation of CNOs were later observed formed by irradiation of carbon in an electron microscope [7]. Due to the intensity of the focused ion beam, the graphitized carbon began to curl and after some time the onion closed on itself under an electron beam [7]. However, for a material to be applied in industry, production of large quantities are required and the method proposed by Ugarte was not sufficient to produce large yields of CNOs. In 1994, nanodiamond annealing turned into a famous technique for creating huge amounts of CNOs with particle sizes of 6-8 nm [8-10]. Sano *et al*. at that point utilized a comparable strategy for vacuum annealing of nanodiamond creating huge amounts of CNOs with greater particle sizes going from 4-36 nm. Their strategy in this manner had incredible potential in the industrial application for the generation of large amount of CNOs [11]. However, the raw nanodiamond materials used for the production of CNOs are expensive. Besides vacuum annealing of nanodiamond [12], CNOs can also be synthesized using electron beam irradiation [13], use of a plasma [14], chemical vapor deposition (CVD) [15] etc. However, all the above mentioned processes require a high energy input and usually the as synthesized material is contaminated with other forms of carbon or the catalyst used (as in the CVD method). Furthermore, removal of the unwanted by-products or the catalyst has an impact on the yields of CNOs and also their presence increases the resistivity of the material [13]. Therefore, the large scale production of CNOs requires a method that is simple to use and is cheap. The use of the flame method is considered a potential method for producing CNOs in large quantities because it is cheap, easy to use and it does not produce any by-products. CNOs can be produced in large

quantities without the use of an advanced vacuum chamber [16]. From the flame pyrolysis reaction, reactive radicals are promoted by the high flame temperature, resulting in the growth of CNOs that are quasi-spherical in shape. Different types of sources have been used to produce CNOs of different sizes where the flames are irradiated or modulated with a laser beam and acoustic excitation [17-21]. The flame pyrolysis method produces onion like structures that are not contaminated with other forms of carbon. Hence, removal of the unwanted materials using harsh chemicals is not required. Mohapatra *et al*. reported the synthesis of CNOs from an "oil-wick" method [16]. Their method produced CNOs that are crystalline with no by-products and no need for purification of the raw soot and the method does not involve any catalyst as required in a CVD method. In addition, a report on annealing of CNOs by Mongwe *et al.* has shown that the pore volume of the material increases upon annealing under an inert atmosphere, depending on the type of collecting plate used (i.e. brass plate) [22].

A conductive material that has a high surface area is required for energy storage in supercapacitors. The conductivity of the raw soot can be improved by using dopants. As discussed in **Chapter 2**, both boron and nitrogen can easily replace the carbon in a carbon network since their atomic masses are close to that of carbon [23]. Their replacement in a carbon matrix can lead to an alteration of the Fermi level by both nitrogen and boron, thus improving the conductivity of the material [24].

In this work, CNOs synthesized from a flame ("wick-oil" method) were doped with both nitrogen and boron and their properties were explored. Grapeseed oil was chosen as a carbon source due to its long carbon chains which can be pyrolysed to form carbon nano-onions.

4.1 Materials and reagents

Table 4. 1: Materials and reagents used in this study

Reagents and materials	Purity and speciation	Supplier
Grapeseed oil	-	Dischem, South Africa
Argon, $Ar_{(g)}$	≥ 99%	Afrox
Ammonia, $NH_{3(g)}$	≥ 99%	AFrox

Trimethyl borate, $(CH_3O)_3B$	≥ 98%	Sigma- Aldrich

4.2 Synthesis of CNOs using flame pyrolysis

CNOs were synthesized by an "oil-wick'' method using grapeseed oil as a carbon precursor [25]. A pure wick was immersed inside the glass pot containing the grapeseed oil (see **Figure 4.1**). The exposed part of the wick was ignited and the soot was collected using brass as the collecting plate. The raw soot was labelled as pristine CNOs.

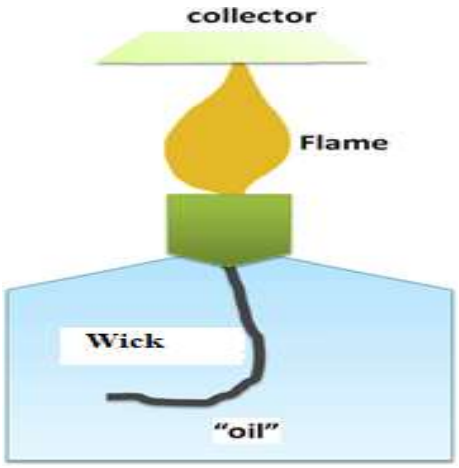


Figure 4.1: Flame pyrolysis method for synthesis of CNOs [16].

4.3 Annealing of the raw soot

The raw soot was annealed under a flow of Ar gas. About 0.2 g of the raw soot was set in a quartz boat in the centre of a quartz tube. The synthesis temperature was raised to 750 ℃ at 10 ℃/min under Ar gas flow (100 mL/min) for 2 h. The annealing method was repeated at different temperatures (850 ℃ and 950 ℃) for different times (2 h and 4 h).

4.4 Boron doped raw soot

The B-CNOs were synthesized following a procedure reported in literature [26]. The synthesis procedure was followed by adding 0.2 g of the raw soot in a quartz boat and placed in a quartz tube positioned in a furnace. Argon gas and trimethyl borate ($(CH_3O)_3B$ were used as a carrier gas and boron source respectively. The synthesis temperature was raised to a temperature of 750 ℃ under Ar gas flow (100 mL/min). Ar gas (100 mL/min) was then bubbled through $(CH_3O)_3B$ for 2 h at a temperature of 750 ℃. After this, the $(CH_3O)_3B$ feed was discontinued and the system was cooled under Ar gas. The product was labelled as B-CNOs.

4.5 Nitrogen doped raw soot

Nitrogen doping was conducted following a procedure reported in literature [27]. For the synthesis, about 0.2 g of the raw soot was placed in a quartz tube in the centre of the furnace. The synthesis temperature was elevated to 750 ℃ under Ar gas flow (100 mL/min). The doping was achieved by passing ammonia (NH_3) gas (100 mL/min) together with Ar gas (100 mL/min) through the quartz tube for a period of 2 h. The NH_3 gas feed was stopped and the furnace was cooled to a temperature of 25 ℃ under Ar gas flow. The product was labelled as N-CNOs.

4.6 Results and discussion

4.6.1 TEM analysis of the pristine, annealed and doped CNOs

The TEM images of the pristine and annealed CNOs are shown in **Figure 4.2**. The low magnification TEM images (**Figure 4.2a**) show an overview of the CNO particles. As can be seen from **Figure 4.2a**, the particles are agglomerated with a spherical morphology (20 ± 4.5 nm). A histogram of the particle size is shown in **Figure 4.3** obtained from image J (about 100 particles).

At higher magnification (**Figure 4.2b,c**), the pristine CNOs possess graphitic layers in an interconnected network structure, as shown in **Figure 4.2b** by the yellow circle (see also supplementary **Figure S2a**). The distance of 0.34 nm (shown by yellow lines in **Figure 4.2c**) corresponds to the distance between carbon layers [28]. The graphitic layers form an interconnected coalescence region with other particles. This can be seen from **Figure 4.2d-f** for annealed CNOs at 750 °C (2 h) where the bigger particles tend to form an interconnected network with smaller particles as seen in the yellow circle in **Figure 4.2d**. The distance between the graphitic layers is 0.35 nm for the annealed CNOs (marked by yellow lines in **Figure 4.2f**). The concentric graphitic layers which are features of CNOs are clearly visible in all HRTEM images (see **Figure 4.2b-f**) [29, 30]. These results are similar to results for CNOs reported in literature using different carbon precursors [16, 22].

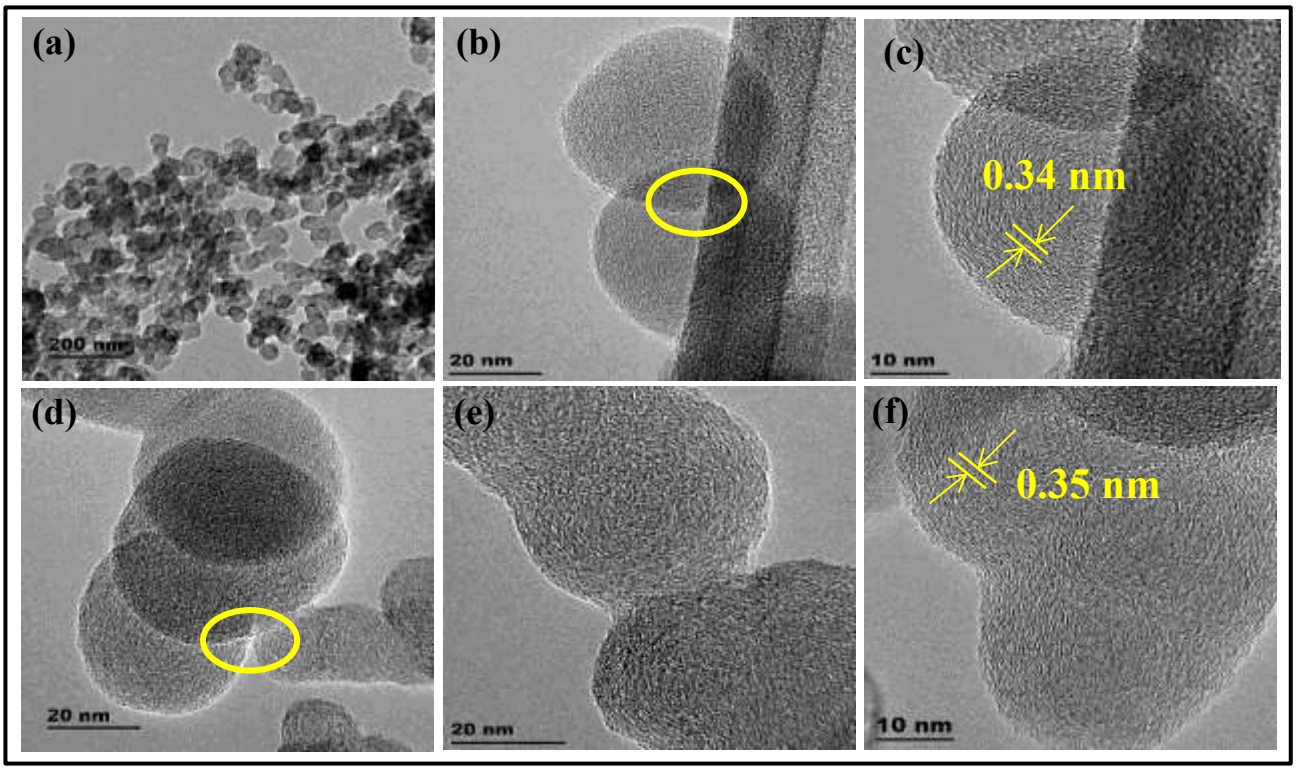


Figure 4.2: (a-c) TEM images of the pristine and (d-e) annealed CNOs at 750 ℃-2 h.

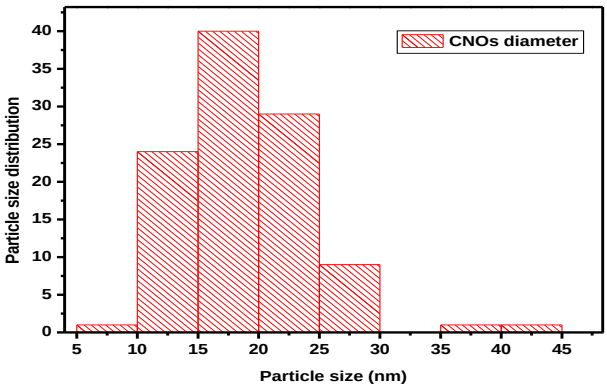


Figure 4.3: Particle size distribution of pristine CNOs.

The B-doped and N-doped CNOs also show multi-layered concentric layers (**Figure 4.4a-f**). The boron and nitrogen doping did show smaller particles coupled with bigger particles indicated by the yellow circle shown in **Figure 4.4a,d** (see also **Figure S2b**). No obvious changes in the CNO surface was observed after doping with nitrogen and boron (**Figure 4.4a-f**). These results are consistent with the work reported by Shaikh and co-workers where N-doping on the surface of CNOs did not alter the structure of the carbon material [31].

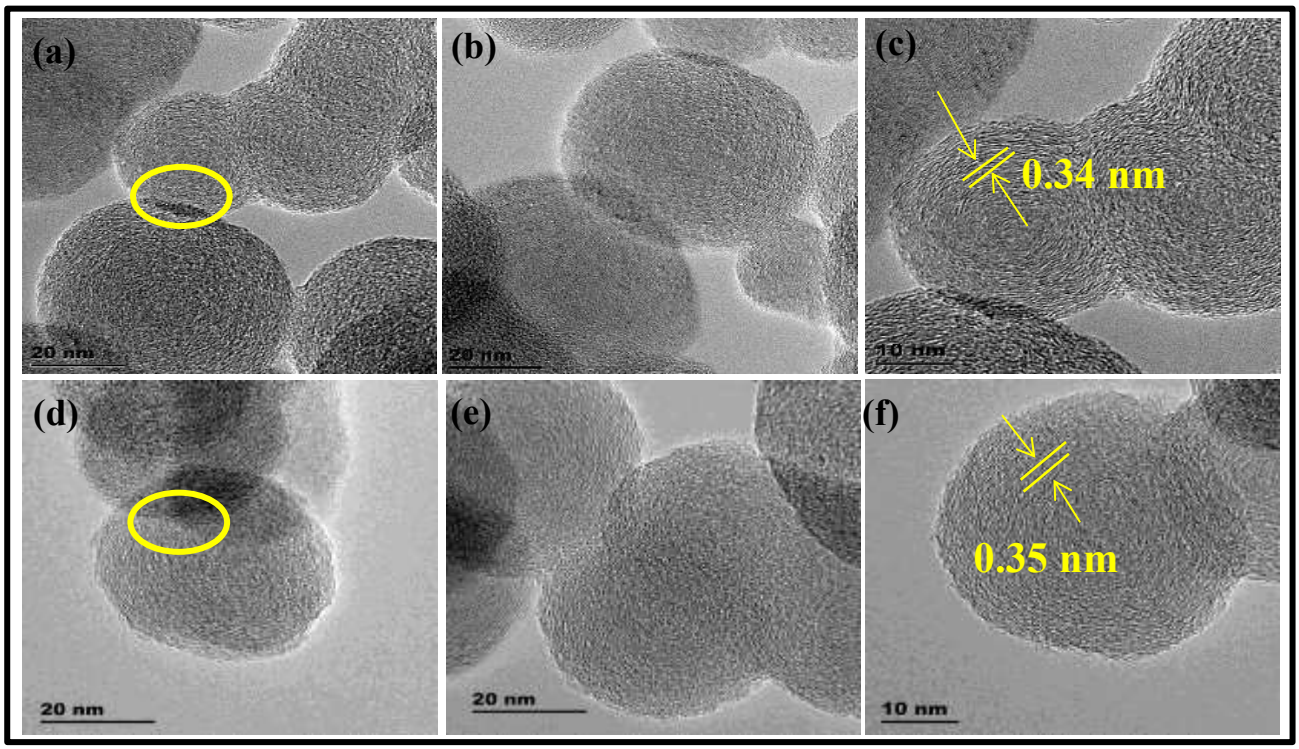


Figure 4.4: (a-c) High magnification TEM images of N-doped CNOs and (d-f) B-doped CNOs.

The key findings from **Figure 4.2-4.4** are summarized as follows:

(a) CNOs were successsfully synthesized from flame pyrolysis with multi-layered carbon structure and a a particle size of < 100 nm with d-spacing of 0.34 nm.

(b) Annealing at 750 ℃-2 h, boron and nitrogen doping did not appear to disrupt the structure of the pristine CNOs as shown from the TEM images.

4.6.2 Raman analysis of pristine, annealed and doped CNOs

The Raman spectra for all the materials (pristine and annealed CNOs) show two peaks (G and D band) in the 500-2000 cm^{-1} region (see **Figure 4.5a**). The D band arises from structural defects. The G-band corresponds to the graphitic band [32]. The intense D-band arises when the number of structural defects increases and is not present in an oriented pyrolytic graphite (HOPG) [33]. Therefore, the number of defects in carbon nanomaterials can be measured by using the area ratio of the D and G-bands. The band ratio is summarised in **Table 4.2**. From **Table 4.2**, it can be seen that the I_D/I_G ratios vary between 0.21 and 2.17. Also, the I_D/I_G ratio decreases upon annealing at different temperatures and times due to the ordering of the carbon particles [34]. As seen from **Table 4.2**, a downshift of the D-band position is observed upon graphitization of the material. These results are in accordance with previous results when the I_D/I_G ratio decreased upon annealing at high temperatures [35, 36]. The FWHM of the G-band in the carbon material can also be used to measure the ordering of the material. In this study, the FWHM of the G-band of the pristine CNOs is 105 cm^{-1} (see **Figure S3**) which is seven times wider than HOPG (FWHM 15 cm^{-1}) but comparable to CNOs synthesized from other sources [37, 38].

The Raman spectra of the B-doped and N-doped CNOs also exhibited two main peaks, the defect D-band and the graphitic G-band in the region 1300-1600 cm^{-1} as shown in **Figure 4.5b**. The area and peak positions of the D-band and G-band was affected by doping of the carbon nanostructure. Upon N-doping of the CNOs, the area of the D-band increased suggesting an increase in structural defects due to the shorter carbon-nitrogen bond being formed [39]. The position of the G-band upshifted which can be attributed to the shift of the Fermi level during the doping process [40, 41].

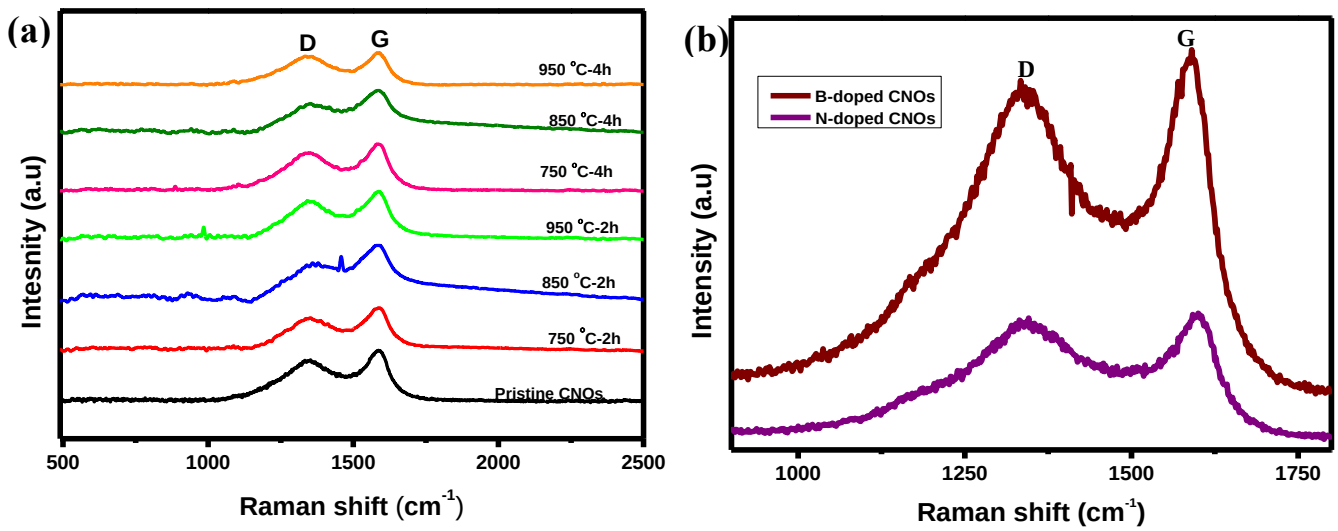


Figure 4.5: (a) Raman spectra of pristine, annealed and (b) B-doped and N-doped CNOs.

The I_D/I_G ratio increased upon N-doping due to the presence of more structural defects found in the pristine CNOs (see **Table 4.2**). It is importatnt to note the introduction of defects by boron doping in the carbon matrix resulted in an upshift of the G-band. The increase in the area of the D-band is also due to the increase in structural defects formed through C-B bond formation as confirmed by the increase in I_D/I_G ratio [42]. Besides determining the amount of defects present in the material using the I_D/I_G ratio, the crystallite size, L_a, of the material can also be used. According to the equation described by the Tuinstra−Koenig relationship [43], La is inversily proportional to the I_D/I_G ratio and is calculated using the following **equation 4.1**:

$$L_a = (2.4 \times 10^{-10})\lambda^4 \left(\frac{I_D}{I_G}\right)^{-1} \qquad \text{eqn 4.1}$$

In this study, the excitation wavelength (λ) used is 532 nm.

The L_a values calculated from the above equation 4.1 are 8.86 nm, 6.75 nm and 5.77 nm for the pristine, B-doped and N-doped CNOs respectively. The decrease in L_a suggest smaller domains present in the carbon material after introdcution of boron and nitrogen [44].

Table 4. 2: Raman data for pristine, annealed, B-doped and N-doped CNOs.

	D-band		G-band		
Type of material	**Raman shift (cm^{-1})**	**Area**	**Raman shift (cm^{-1})**	**Area**	**I_D/I_G**
Pristine CNOs	1355.4	36192.5	1587.1	16643.4	2.17
750 ℃-2h	1354.4	23892.7	1581.3	16329.9	1.46
850 ℃-2h	1327.4	10140.2	1559.2	47983.5	0.21
950 ℃-2h	1354.7	26657.9	1579.7	19352.5	1.38
750 ℃-4h	1350.6	30779.6	1582.1	16741.5	1.84
850 ℃-4h	1346.4	14612.3	1577.4	24633.7	0.59
950 ℃-4h	1346.9	21797.4	1582.9	10435.2	2.09
B-doped CNOs	1345.8	200607.8	1584.8	70333.2	2.85
N-doped CNOs	1353.8	81732.5	1594.6	24551.4	3.33

Results obtained from **Figure 4.5** and **Table 4.2** are summarized as follows:

(a) Annealing resulted in a decrease in the I_D/I_G ratio due to an ordering of the material.

(b) Doping of the materials resulted in smaller domains, as seen from the decrease of L_a.

4.6.3 XRD analysis of pristine, annealed and doped CNOs

The crystallinity of the CNOs was studied by XRD. **Figure 4.6a,b** show the structural features of the CNOs after annealing and doping with boron and nitrogen. The XRD patterns of the pristine and annealed CNOs all have a broad graphitic peak positioned at 2 theta angle of 23.69° associated with the (002) reflection [45]. However, a shift to higher 2Θ of 28.70° was observed for the annealed CNOs (750 °C-4 h). This behaviour can be due to the packing of the sample during analysis.

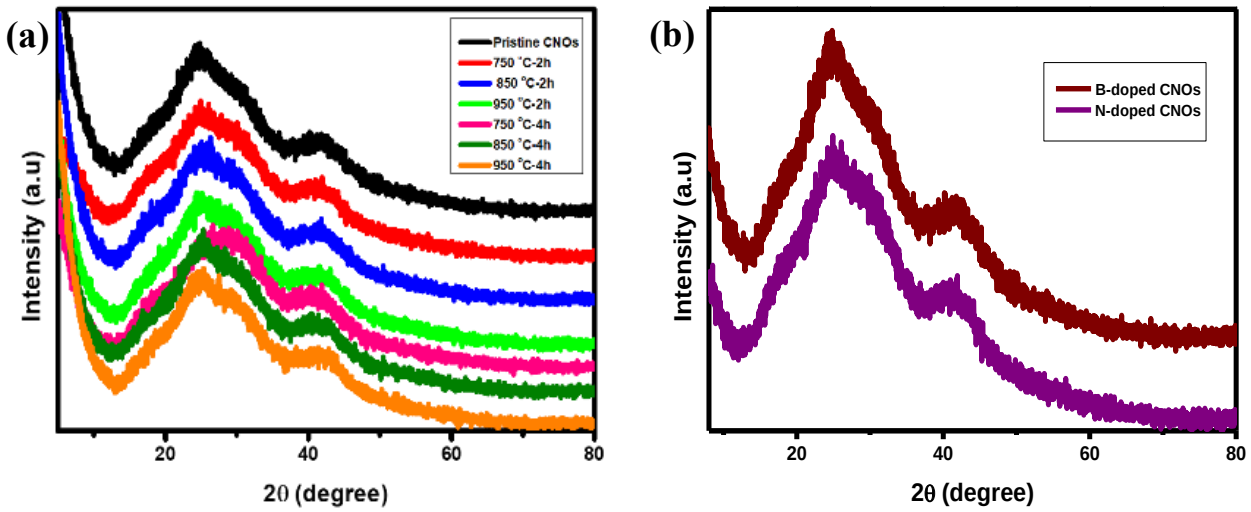


Figure 4.6: (a) XRD patterns of pristine, annealed and (b) B-doped and N-doped CNOs.

The low intense peak at 2Θ of 41.43° corresponds to the (100) reflection. The calculated interlayer spacing from the (002) reflection peak is 3.75 Å which is comparable to the d - spacing of OLCs from vacuum annealing of nanodiamonds [46] but higher than the graphite value (3.36 Å). The presence of structural defects from the materials resulted in a higher d-spacing than for the graphite material. The XRD patterns for B-doped and N-doped onions did not show any significant changes, with a broad peak positioned at 2Θ of 28.70° from the contributions of the sp^2 bonded carbons (see **Figure 4.6b**). The broadness of the peaks arises from the sizes of the nanoparticles and can also be due to the defects in the material and shells that are incompletely formed, having smaller domains when compared to the pristine CNOs.

4.6.4 Thermal stability of pristine and annealed CNOs

The thermal stability of the synthesized materials was determined by using TGA. As shown in **Figure 4.7a, b**, the TGA profiles for the pristine and annealed CNOs are similar with variable decomposition temperatures. It can be seen, that the materials prepared are purely carbonaceous since they decompose completely leaving no residual mass. The maxima from the derivative plots were used to estimate the decomposition temperature of the synthesized materials. The onset decomposition temperatures of the pristine and annealed CNOs were above 400 ℃ confirming from TEM studies that there was no amorphous carbon present. According to the results presented by Chen *et al*. [47], better graphitized materials are oxidized at higher temperatures. However, the annealed materials at 750 ℃ and 850 °C for 2

h and 4 h had lower decomposition temperatures compared to the pristine CNOs suggesting that materials annealed at 750 ℃ and 850 °C for 2 h and 4 h might have more multiple centres or structural disorder caused by the presence of oil residue. This can be further confirmed by the HRTEM images of the annealed CNOs at 750 °C-2 h which have smaller and bigger particles after pyrolysis under an inert atmosphere [48]. Furthermore, the stability of the materials annealed at 950 °C for 2 h and 4 h was higher than the pristine CNOs which can be attributed to the increase in the number of concentric layers [49]. The pristine CNOs has a wider full width at half maximum (FWHM ca 161) compared to the annealed CNOs (FWHM ca. 130, 750 °C-2 h), (FWHM ca. 110, 850° C-2 h), (FWHM ca. 131, 950 °C-2 h), (FWHM ca. 109, 750 °C-4 h), (FWHM ca. 113, 850 °C-4 h), (FWHM ca. 141, 950 °C-4 h) indicating that the annealing process resulted in formation of concentric layers that are stable, leading to a slower decomposition occurring for the annealed materials.

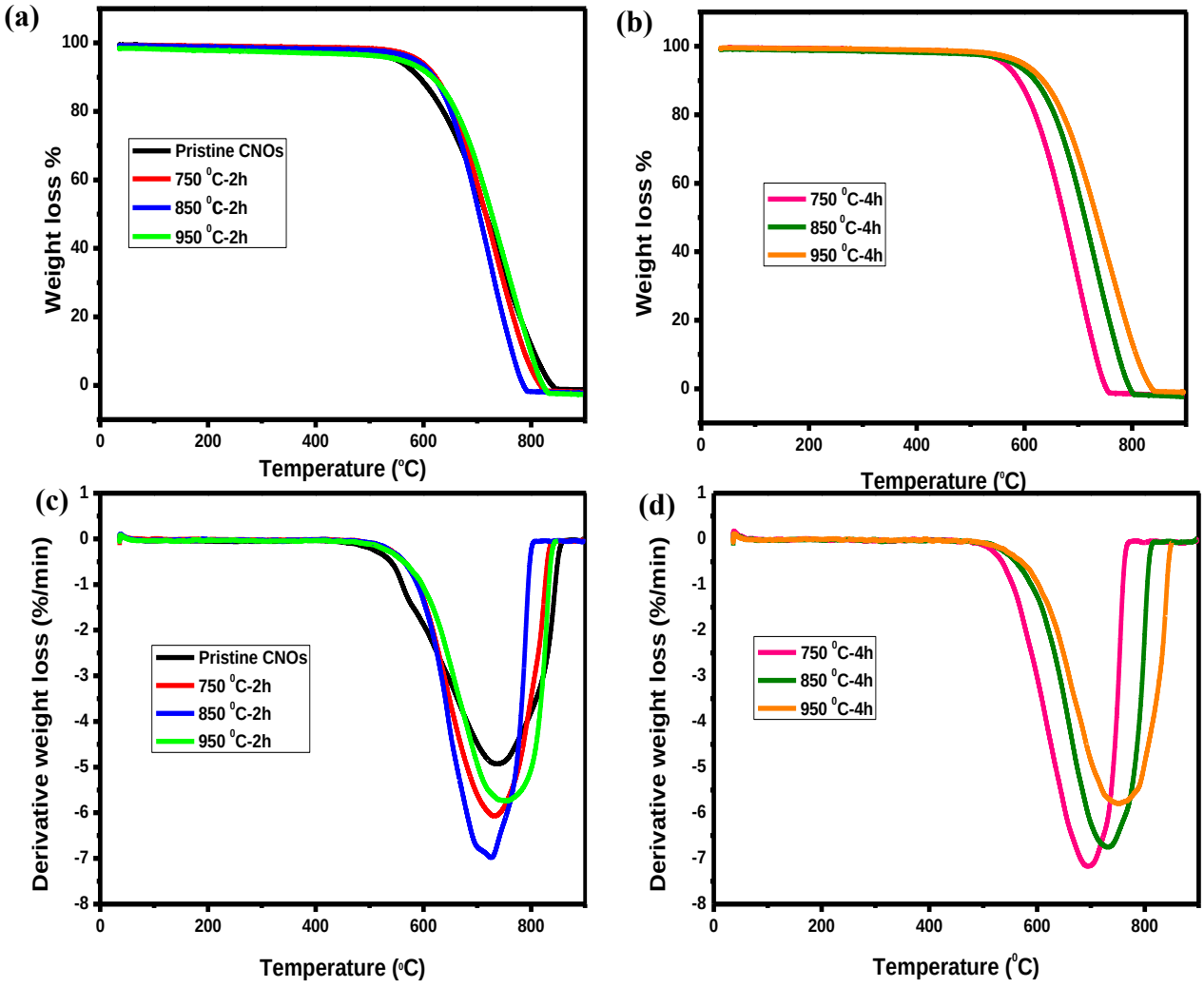


Figure 4.7: (a, b) TGA and (c, d) TGA-derivative plots of the pristine and annealed CNOs.

The overall purity of the B-doped and N-doped CNOs was evaluated using TGA. The TGA profiles and the corresponding derivative curves are shown in **Figure 4.8a, b**. The maxima from the derivative plots were used to estimate the decomposition temperature of the B-doped and N-doped CNOs. The B-doped and N-doped CNOs were less thermally stable compared to the pristine CNOs which can be attributed to the increase in structural defects and disorder introduced by the reactive sites in B-doped and N-doped CNOs. The onset decomposition temperature observed for N-doped and B-doped CNOs are 687 ℃ and 635 ℃ respectively (**Table 4.3**).

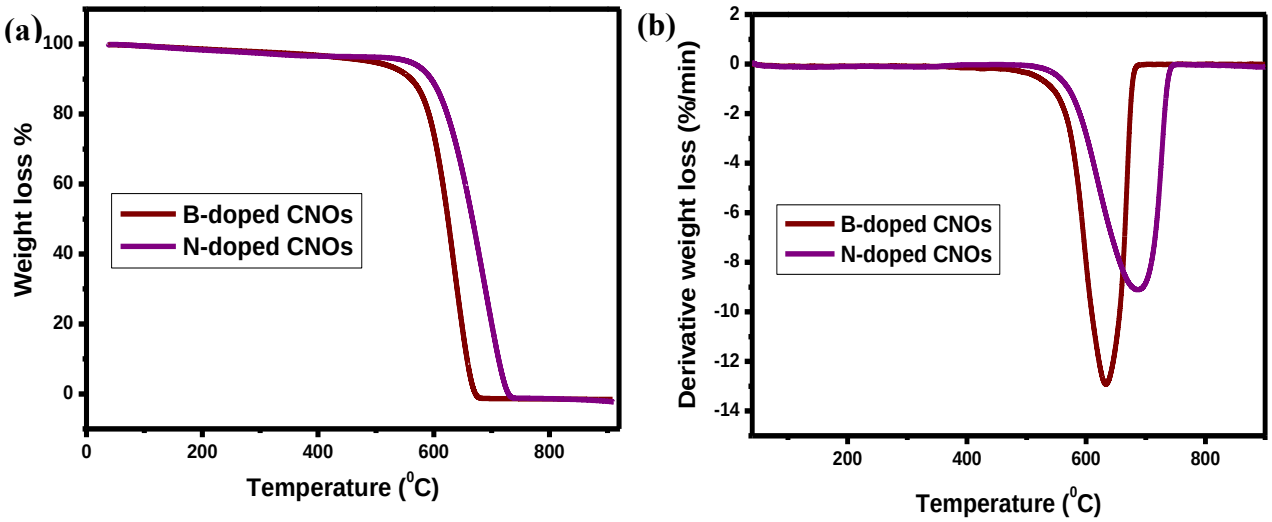


Figure 4.8: (a) TGA data and (b) TGA-derivative plots for B-doped and N-doped CNOs.

Table 4. 3: Decomposition temperatures (determined by the derivative TGA) for the pristine, annealed CNOs at different temperatures and time and B-doped and N-doped CNOs.

Type of material	Decomposition temperature (°C)
Pristine CNOs	724
750 °C-2 h	721
850 °C-2 h	710
950 °C-2 h	737
750 °C-4 h	699

850 °C-4 h	719
950 °C-4 h	744
B-doped CNOs	635
N-doped CNOs	687

Results shown in **Figure 4.7** and **4.8** are summarized as follows:

(a) Annealing affects the physical properties of CNOs which resulted in a more stable material at 950 ℃-4 h due to the ordering of the materials for a longer time.

(b) The boron and nitrogen doped materials were less stable compared to the pristine material due to the increase in structural defects.

4.6.5 CN and XPS elemental analysis of the pristine and N-doped CNOs

The mol % of nitrogen formed in the CNOs upon doping was evaluated using both CN and XPS elemental analyses (**Table 4.4**). The incorporation of nitrogen was confirmed by the CN elemental analysis (N = 1.67%). This is similar to data reported by Lin *et al.* (2.1 mol % N) after nitrogen was doped into CNOs using ammonia (NH_3) on oxygen functionalized CNOs [27].

Table 4. 4: CN measurements of the pristine and N-doped CNOs.

	CN analysis		**XPS analysis**		
	C (%)	**N (%)**	**C (%)**	**N (%)**	**O (%)**
Pristine CNOs	91.6	0.37	89.9	-	10.0
N-doped CNOs	96.0	1.67	93.4	1.7	4.6

The survey scans of the pristine and N-doped CNOs are shown in **Figure 4.9**. Both the materials have two distinct peaks corresponding to C1s and O1s positioned at 284.3 eV and 532.6 eV.

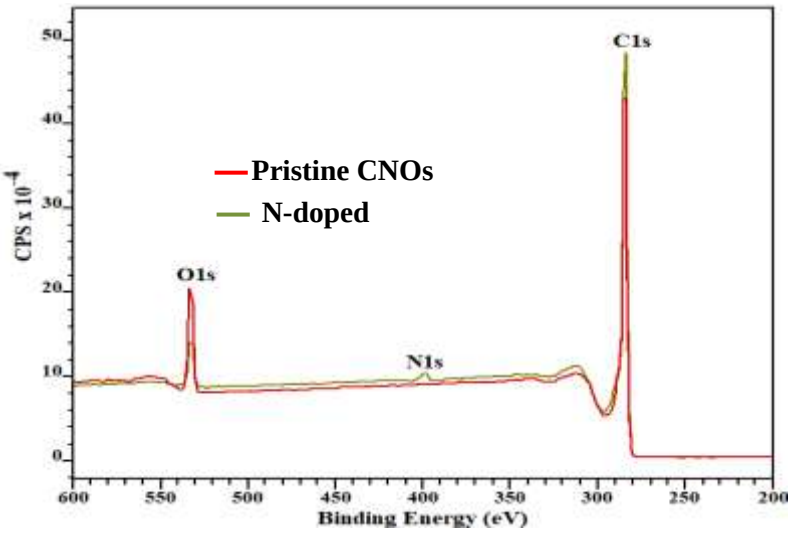


Figure 4. 9: XPS survey spectra of pristine and N-doped CNOs.

The small peak corresponding to N1s in N-doped CNOs is positioned at 398.9 eV and it was not observed in the pristine CNOs spectrum indicating successful introduction of nitrogen on the surface of CNOs. The C1s, O1s and N1s were deconvoluted from the XPS survey scans.

The deconvolution of the C1s for pristine CNOs gave rise to signals represented in **Figure 4.10a**. The signals comprise of sp^2 C-C (283.95 eV), sp^3 C-C (248.89 eV) [50], C-O (286.14 eV), O-C=O (288.43 eV) [51]. The O1s peak from the XPS survey scan was also deconvoluted and represented in **Figure 4.10b**. The oxygenated carbon atoms are positioned at 533.33 eV for O-C=O and 531.93 for C-O-C (**Table 4.5**) [52, 53].

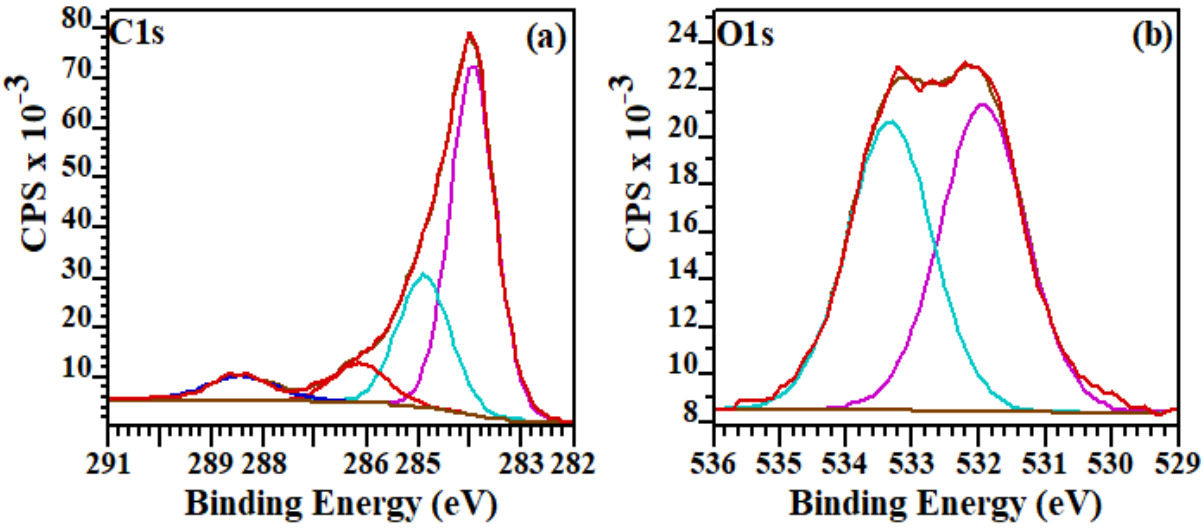


Figure 4. 10: (a) The C1s and (b) O1s deconvoluted spectra of pristine CNOs.

The C1s peak for N-doped CNOs was also deconvoluted which gave rise to five peaks for sp^2-C-C (283.96 eV), sp^2-N-C (284.87 eV), sp^3-C-C/sp^3-C –N (285.57 eV), C-O (287.14 eV), O-C=O/N-C=O (289.43 eV) (**Figure 4.11a**) [51]. The deconvolution of the O1s from the survey scan of the N-doped CNOs gave rise to three peaks of O-C-O (531.45 eV), O-C=O (533.16 eV), C-O-C (532.19 eV) (**Figure 4.11b**) [52, 53]. The deconvolution of the N1s peak gave rise to four peaks for pyrrolic-N (397.86 eV), pyridinic-N (399.08 eV), graphitic-N (399.91 eV) and oxygenated pyridinic-N (NOx, 400.92 eV) represented in **Figure 4.11c** with the data represented in **Table 4.5** [54, 55].

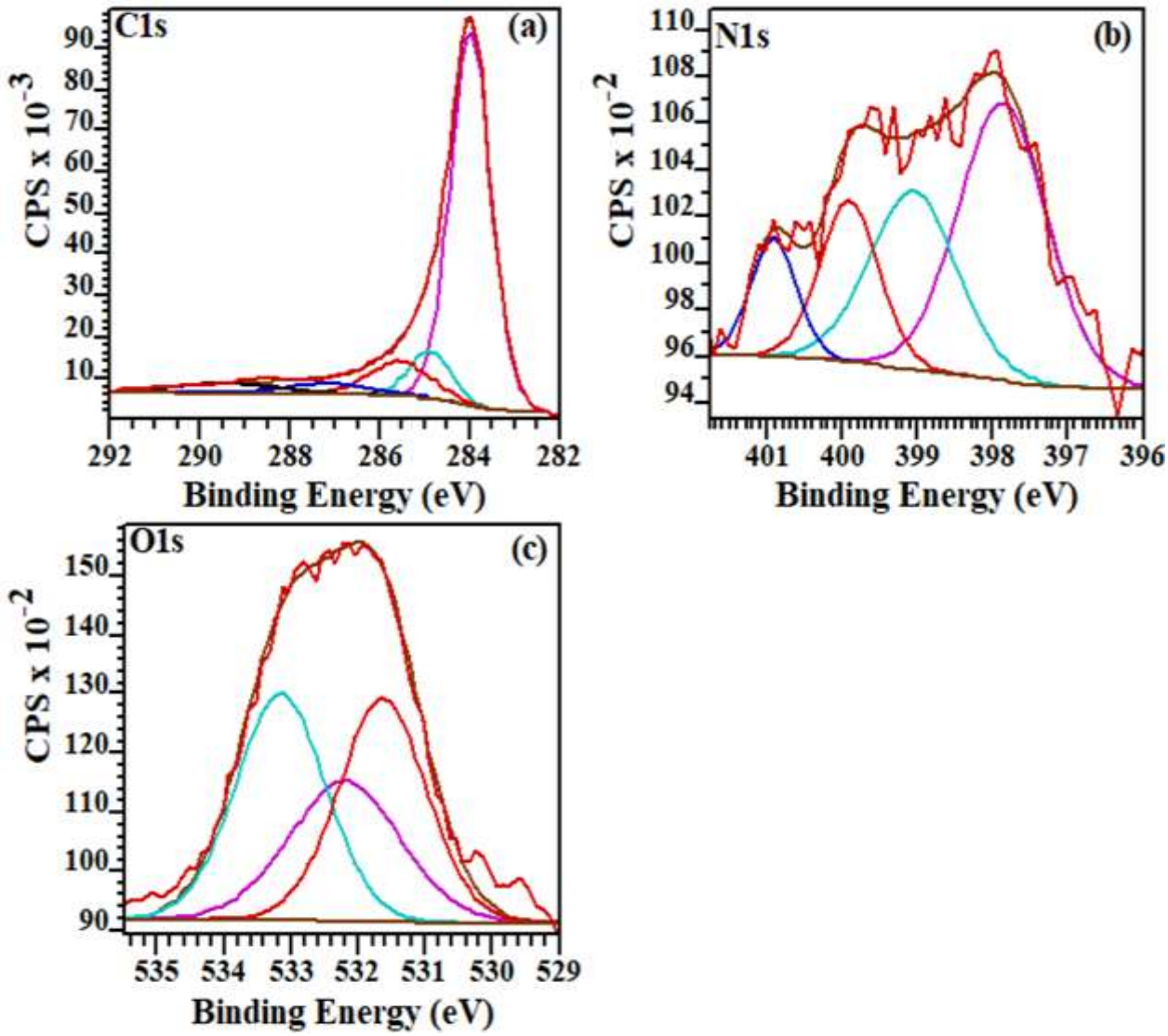


Figure 4. 11: (a) C1s, (b) O1s and (c) N1s deconvoluted spectra of N-doped CNOs.

Table 4. 5: XPS component peak positions (eV).

Samples	sp^2-C-C	sp^2-N-C	sp^3-C-C/ sp^3-C-N	C-O	O-C=O/ N-C=O	Pyrr-N	Pyri-N	Gra-N	NOx	O-C-O	O-C=O	C-O-C
Pristine	283.9	-	284.8	286.1	288.4	-	-	-	-	-	533.3	531.9
N-doped	283.9	284.8	285.5	287.1	289.4	397.8	399.0	399.9	400.9	531.4	533.1	532.1

The average % concentrations of the atoms present in both samples (pristine and N-doped CNOs) are represented in **Table 4.6**. The % concentration of the sp^3 decreased when doping with nitrogen. There was a decrease in % concentration of oxygenated groups when doping with nitrogen. This can be attributed to two main reasons: (i) nitrogen doping under inert gas promotes the removal of oxygen atoms from the surface hence the decrease in oxygen atoms, (ii) NH_3 reacted with the oxygen species on the surface during the N-doping processes [56].

Table 4. 6: Summary of % concentration of all bonds in the samples.

Samples	sp^2-C-C	sp^2-N-C	sp^3-C-C/ sp^3-C-N	C-O	O-C=O/ N-C=O	Pyrr-N	Pyri-N	Gra-N	NOx	O-C-O	O-C=O	C-O-C
Pristine	58.8	-	25.6	8.3	7.1	-	-	-	-	-	48.2	51.7
N-doped	70.0	9.4	10.2	4.7	5.5	44.7	28.2	17.1	9.8	35.3	36.5	28.0

4.6.6 Surface area analysis of pristine, annealed, B-doped and N-doped CNOs

The specific capacitance of carbon materials is affected by the pore volume, pore size and surface area of the carbon. At a low flame temperature, there is residual oil left behind in the raw soot. When not removed this lowers the BET surface area (see **Table 4.7**). Upon annealing at 750 °C for 2 h, the BET surface area increased slightly. Also, the N-doping of the carbon materials increased the surface area of the pristine material. The same trend was observed for the pore volumes which increased from 0.07 cm^3/g for the pristine CNOs to 0.11 cm^3/g for the N-doped CNOs. However, B-doping decreased the specific surface area of the carbon particles. This might be due to the defects present in the material.

Table 4. 7: BET surface areas and pore volumes of the pristine, annealed, B-doped and N-doped CNOs.

Type of material	BET S.A (m^2/g)	Pore volume (cm^3/g)	Pore size (nm)
Pristine CNOs	89.8	0.07	3.2
750 °C-2h	94.2	0.09	3.7
B-doped CNOs	73.2	0.18	8.6
N-doped CNOs	116.4	0.11	3.4

4.7 Growth mechanism of CNOs synthesized from flame pyrolysis

The formation of CNOs by flame pyrolysis is proposed to occur by a bottom-up approach (**Figure 4.12**) [57]. Formation of the different sizes and shapes of the carbon rings are due to the highly reactive radicals that are formed by the breakdown of molecules in the luminescent flame [58, 59]. Larger CNOs are then promoted by aggregation of multi-layered CNOs that form when the carbon lattices forms form the polycyclic aromatic hydrocarbons (PAHs) [60].

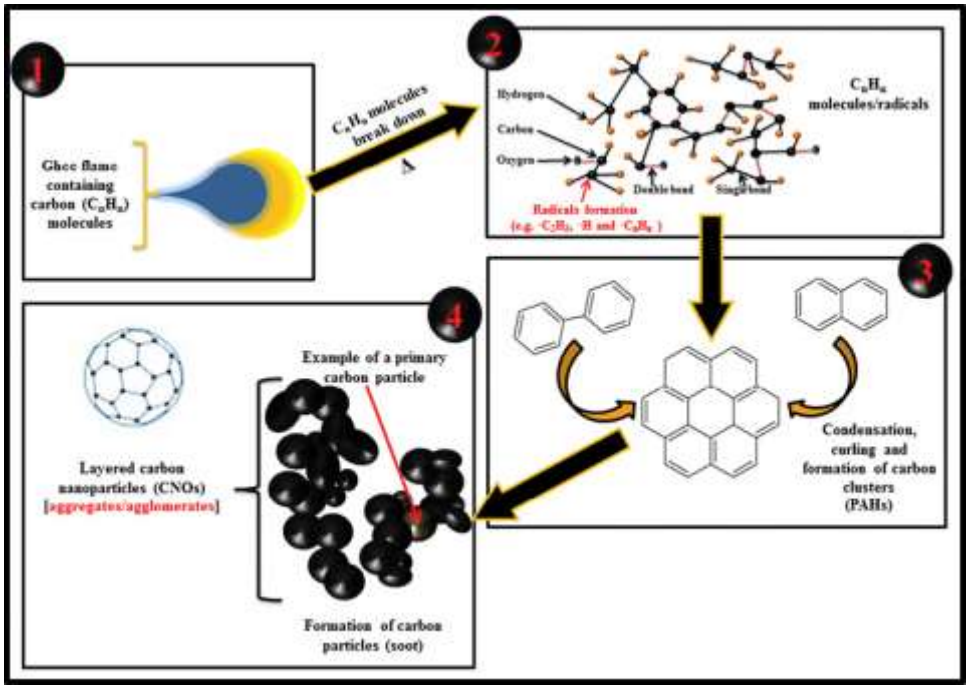


Figure 4. 12: Growth mechanism of CNOs via the bottom-up approach [22].

4.8 Conclusions

The flame pyrolysis method has been successfully used for the synthesis of CNO nanoparticles using grapeseed oil as a carbon precursor. Their onion like structure were obtained with a particle size of 20 ± 4.5 nm as confirmed by HRTEM studies. The CNOs synthesized are not contaminated with any other form of carbon, as confirmed by TGA results. Annealing, and boron and nitrogen doping does not alter the structure of CNOs as seen from the HRTEM images. Raman and XRD data indicated the presence of defects in the CNO materials which can serve as reactive sites for electrolyte adsorption in energy storage application. The XPS data shows that nitrogen was successfully doped on the carbon matrix with a mol% of 1.7. Annealing and doping of the CNOs affected the microporosity/mesoporosity as seen from the BET results. To summarize, the physico-chemical properties of CNOs are both affected by the annealing temperature and doping.

4.9 References

1. M. Inagaki, H. Konno, O. Tanaike. *J. Power Sources* 195 (2010) 7880.
2. J. Bartelmess, S. Giordani. *J. Nanotechnology* 5 (2014) 1980.
3. S. Porada, L. Borchardt, M. Oschatz, M. Bryjak, J. Atchison, K. Keesman *et al*. *Energy Environmental Science* 6 (2013) 3700.
4. X. Huang, X. Qi, F. Boey, H. Zhang. *Chemical Society Reviews* 41 (2012) 666.
5. V. Presser, M. Heon, Y. Gogotsi. *Advanced Functional Materials* 21 (2011) 810.
6. S. Iijima. *J. Crystal Growth* 50 (1980) 675.
7. D. Ugarte. *Nature* 359 (1992) 707.
8. B. Xu, S.I. Tanaka. *Acta Materials* 46 (1998) 5249.
9. A.G. Nasibulin, A. Moisala, D.P. Brown, E.I. Kauppinen. *Carbon* 41 (2003) 2711.
10. V.L. Kuznetsov, A.L. Chuvilin, Y.V. Butenko, I.Y. Mal'kov, V.M. Titov. *Chemical Physics Letters* 222 (1994) 6144.
11. N. Sano, H. Wang, M. Chhowalla, I. Alexandrou, G.A..J. Amaratunga. *Nature* 414 (2001) 506.
12. K. Makgopa, P.M. Ejikeme, C.J. Jafta, K. Raju, M. Zeiger, V. Presser, K.I. Ozoemena. *Materials Chemistry A* 3 (2015) 3480
13. M. Choi, I.S. Altman, Y.J. Kim, P.V. Pikitsa, S. Lee, G.S. Park, T. Jeong, J.B. Yoo. *Advanced Materials* 16 (2004) 1721.
14. E. Koudoumas, O. Kokkinaki, M. Konstantaki. *Chemical Physical Letters* 357 (2002) 336.
15. F.D. Han, B. Yao, Y.J. Bai. *J. Physical Chemistry* 115 (2011) 8923.
16. D. Mohapatra, S. Badrayyana, S. Parida. *Chemical Physics* 174 (2016) 112.
17. P. Dubey, K.M. Tripathi, S.K. Sonkar. *RSC Advances* 4 (2014) 5838.
18. S.Y. Sawant, R.S. Somani, A.B. Panda, H.C. Bajaj. *Materials Letters* 94 (2013) 132.
19. S.S. Hou, D.H. Chung, T.H. Lin. *Carbon* 47 (2009) 938.
20. W.C. Hu, S.S. Hou, T.H. Lin. J. *Nanoscience Nanotechnology* 14 (2014) 5363.
21. M. Choi, I.S. Altman, Y.J. Kim, P.V. Pikhitsa, S. Lee, G.S. Park, T. Jeong, J.B. Yoo. *Advanced Materials* 16 (2004) 1721.
22. T.H. Mongwe, B.J. Matsoso, B.K. Mutuma, N.J. Covillea, M.S. Maubane. *Diamond & Related Materials* 90 (2018) 135.
23. P. Rani, V.K. Jindal. Designing band gap of graphene by B and N dopant atoms. *RSC Advances* 3 (2013) 802.

24. L.S. Panchakarla, K.S. Subrahmanyam, S.K. Saha, A. Govindaraj, H.R. Krishnamurthy, U.V. Waghmare, U.V. *Advanced Materials* 46 (2009) 4726.
25. V. Dhand, J.S. Prasad, M.V. Rao, S. Bharadwaj, Y. Anjaneyulu, P.K. Jain. *Materials Science and Engineering C* 33 (2013) 758.
26. Z.N. Tetana, S.D. Mhlanga, G. Bepete, R.W.M. Krause, N.J. Coville. *South African Journal of Chemistry* 65 (2012) 39.
27. Y. Lin, X. Pan, W. Qi, B. Zhang, D.S. Su. *Materials Chemistry* 2 (2014) 12475.
28. L. Joly-Pottuz, B. Vacher, N. Ohmae, J. Martin, T. Epicier. *Tribology Letters* 3 (2008) 69.
29. J. Breczko, K. Winkler, M.E. Plonska-Brzezinska, A. Villalta-Cerdas, L. Echegoyen. *Material Chemistry* 20 (2010) 7761.
30. J.K. McDonough, Y. Gogotsi. *Electrochemical Society Interface* 22 (2013) 61.
31. A.Shaikh, B.K. Singh, D. Mohapatra, S. Parida. *Electrocatalysis* 3 (2019) 222.
32. D. Roy, M. Chhowalla, H. Wang, N. Sano, I. Alexandrou, T. Clyne, G. Amaratunga. *Chemical Physics Letters* 373 (2003) 52.
33. M. Pimenta, G. Dresselhaus, M.S. Dresselhaus, L. Cancado, A. Jorio, R. Saito. *Chemical Physics* 9 (2007) 1276.
34. C. Portet, G Yushi, Y. Gogotsi. *Carbon* 45 (2007) 2511
35. V. Kuznetsov, S. Moseenkov, A. Ischenko, A. Romanenko, T. Buryakov and O. Anikeeva *et al*. *Physica Status Solidi B* 245 (2008) 2051.
36. S. Tomita, T. Sakurai, H. Ohta, M. Fujii and S. Hayashi. *Chemical Physics* 114 (2001) 7477.
37. M. Dresselhaus, A. Jorio, R. Saito. *Annual Review of Condensed Matter Physics* 1 (2010) 89.
38. M. Pimenta, G. Dresselhaus, M.S. Dresselhaus, L. Cancado, A. Jorio, R. Saito. *Physical Chemistry Chemical Physics* 9 (2007) 1276.
39. L. S. Panchakarla, K. S. Subrahmanyam, S. K. Saha, A. Govindaraj, H. R. Krishnamurthy, U. V. Waghmare, C. N. R. Rao. *Advanced Materials* 21 (2009) 4726.
40. X. Ling, J. Wu, L. Xie and J. Zhang. *J. Physical Chemistry C* 117 (2013) 2369.
41. J. Yan, Y. Zhang, P. Kim and A. Pinczuk. *Physical Review letters* 98 (2007) 166.
42. Y. A. Kim , K. Fujisawa , H. Muramatsu , T. Hayashi , M. Endo , T. Fujimori , K. Kaneko, M. Terrones , J. Behrends , A. Eckmann , C. Casiraghi , K. S. Novoselov , R. Saito and M. S. Dresselhaus. *ACS Nano* 6 (2012) 6293.

43. L.G. Cançado, K. Takai, T. Enoki, M. Endo, Y.A. Kim, H. Mizusaki, A. Jorio, L.N. Coelho, R. Magalhães-Paniago, M.A. Pimenta. *Applied Physical Letters* 88 (2006) 163106.
44. C. Zhang, L. Fu, N. Liu, M. Liu, Y. Wang, Z. Liu. Advanced Materials 23 (2011) 1020.
45. S. Tomita, A. Burian, C. Dorec, D. LeBollochd, M. Fujii, and S. J. Hayashi. *Carbon* 9 (2002) 1469.
46. D. Pech, M. Brunet, H. Durou, P. Huang, V. Mochalin, Y. Gogotsi, P.L. Taberna, P. Simon. *Nature Nanotechnology* 5 (2010) 651.
47. C.M. Chen, Y.M. Dai, J.G. Huang, J.M. Jehng. *Carbon* 44 (2006) 1808.
48. C.M. Long, M.A. Nascarella, P.A. Valberg. *Environmental Pollution* 181 (2013) 271.
49. A.Y. Watson, P.A. Valberg. *Industrial Hygiene Association* 62 (2001) 218.
50. J. Díaz, G. Paolicelli, S. Ferrer, F. Comin. *Physical Review B* 54 (1996) 8064.
51. C. Yuan, X. Liu, M. Jia, Z. Luo, J. Yao. *Material Chemistry A* 3 (2015) 3409.
52. P. Mérel, M. Tabbal, M. Chaker, S. Moisa, J. Margot. *Applied Surface Science* 136 (1998) 105.
53. Y. Kang, Z. Chu, D. Zhang, G. Li, Z. Jiang, H. Cheng. *Carbon* 61 (2013) 200.
54. B.J. Matsoso, K. Ranganathan, B.K. Mutuma, T. Lerotholi, G. Jones, N.J. Coville. *New Journal of Chemistry* 41 (2017) 9497.
55. L. Wang, P. Yu, L. Zhao, C. Tian, D. Zhao, W. Zhou, J. Yin, R. Wang, H. Fu. *Scientific Reports* 4 (2014) 5184.
56. Rinaldi, B. Frank, D. S. Su, S. Hamid, R. Schlogl. *Chemistry of Materials* 23 (2011) 926.
57. K.H. Homann, H.G. Wagner. *Proceedings of the Royal Society of London Series A* 307 (1968) 141.
58. C.R. Shaddix, T.W. Williams. *American Scientist* 5 (2007) 232.
59. M. Frenklach. *Physical Chemistry Chemical Physics* 4 (2002) 2028.
60. A.Y. Watson, P.A. Valberg. *American Industrial Hygiene Association* 62 (2001) 218.

Chapter 5: Application of CNOs in supercapacitors

This chapter presents the electrochemical results from studies of undoped, B-doped and N-doped CNOs using a symmetric system in 2 M KOH.

5. Introduction

The world of today demands energy, however, the energy is mostly dominated by the burning of fossil fuels such as coal. If energy is to be generated from renewable sources such as the sun and the wind then storage of energy will be important. Supercapacitors (SCs) and batteries are energy storage systems that play an important role in today's modern society. In this work, we have focused on energy storage by means of SCs. This is because SCs can be operated over a wide temperature range resulting in high power densities with long life cycles [1]. SCs use three mechanisms for energy storage. As mentioned in **Chapter 2**, EDLCs are one of the ways in which SCs store energy. Carbon materials are mostly used in EDLCs due to their high surface area that can accommodate a large number of electrolytes ions [2]. However, EDCLs store less energy as compared to pseudocapacitors that store energy by Faradaic charge storage whereas hybrid capacitors store energy by Faradaic and non-Faradaic processes [3, 4]. Besides the low amount of energy EDCLs store, they are commonly used in energy sectors because they are technically mature, giving longer life cycles and stability.

Based on the discussion above, this research mainly focuses on CNOs that are applicable for use in EDLCs. The key significant issue in SCs is the connection that happens at the interface of the cathode, anode and the electrolyte. Consequently, it is critical to coordinate the size of the electrolyte particle with that of the pores of the cathode and anode materials since the specific capacitance is affected by how the electrolyte ions diffuse into the pores of the active electrode material. Moreover, the internal resistance of the active material in SCs plays an important role in the amount of energy being stored and it is mainly affected by the ionic conductivity of the electrolyte ions. Ideal electrolytes are of great importance in the application of SCs although each has its own advantages and disadvantages. For example, the use of aqueous electrolytes in laboratories provides easy fabrication and low costs, despite their low energy densities due to their lower operating voltages. Generally, there are different kinds of aqueous electrolytes used, such as the alkaline, acidic and neutral solutions like H_2SO_4, KOH and Na_2SO_4. The conductivity and radii of the hydrated ions in neutral

electrolytes are different. For example, K^+ in KOH has the highest radii of 3.31 Å compared to the radii of H^+ in H_2SO_4 [5]. The hydrated ion in H_2SO_4 has the highest conductivity of 35 mSm^2mol^{-1} compared to the low conductivity of Na^+ in Na_2SO_4 [6]. Besides the high conductivity of H_2SO_4, its corrosion characteristics are still a major problem. Hence, in this report, KOH was investigated for SCs application using a full symmetric device. Electrolyte decomposition needs to be evaluated in SCs because they sometimes lead to failure of operation of SCs resulting in lower capacitance values [7]. Other type of electrolytes (i.e. organic, ionic liquids, redox-type electrolytes, and solid or semi-solid electrolytes) have been explored in the energy sector [8]. Each electrolyte operates in a specific voltage range. For example, neutral aqueous electrolytes can operate at a voltage up to 2 V, with ionic liquids operating up to a wider voltage range of 4 V [9, 10]. Despite the high operating voltage of ionic liquids in SCs, the drawbacks of applying this type of electrolyte commercially is their low conductivity and high viscosity [11]. Furthermore, the advantage of applying semi-state electrolytes in SCs is that there is no liquid leakage [12, 13]. Redox-type electrolytes have also been reported to give rise to high energy densities due to the addition of a pseudocapacitance behaviour from the electrolyte redox reaction at the interface [14].

The use of CNOs as electrode material in EDCLs has been reported, with a large power density at a discharging rate of up to 200 mV/s [15, 16]. The advantages of using CNOs as an electrode material is their outer accessible surface area that gives high power densities. CNOs can be tuned with various activating agents and dopants so as to improve their conductivity. Recent work on boron-doped CNOs for electrochemical energy storage has been reported using 1 M H_2SO_4 electrolyte with a specific capacitance of 27 F/g at a current density of 0.1 A/g [17]. Nitrogen-doped CNOs have also been applied in energy storage systems using a two electrode system. The specific capacitance reported on nitrogen-doped CNOs by Mykhailiv *et al.* [18] was 17 F/g at a current density of 0.1 A/g in 1 M H_2SO_4, with pristine CNOs (without doping) giving 20 F/g. These electrochemical results indicated a slight decrease of specific capacitance upon nitrogen doping.

In this report, KOH was investigated for SCs application using a two electrode system. Pristine CNOs, annealed CNOs at 750 ℃ for 2 h as well as B-doped and N-doped CNOs were applied for energy storage in SCs using 2 M KOH in a full symmetric cell. CNOs from CVD were not applied in this study because of their lack of purity and their low specific surface area.

5. 1 Electrochemical characterization procedure

5.1.1 Fabrication of undoped, B-doped and N-doped CNOs electrodes in a full symmetric cell

Electrochemical measurements were performed in a two electrode system using a T-type cell configuration (see **Figure 5.1a**). A slurry was prepared by sonicating 2.0 mg of the prepared nanomaterials in 1 mL ethanol for 30 min. The resulting slurry was coated on a carbon paper (12 mm x 12 mm) using a plastic dropper. The electrodes were dried at 80 ℃ in a vacuum oven for 12 h before electrochemical testing. A Whatman® microfiber filter was soaked in 2 M KOH and sandwiched between the coated electrodes (see **Figure 5.1b**) for application in SCs.

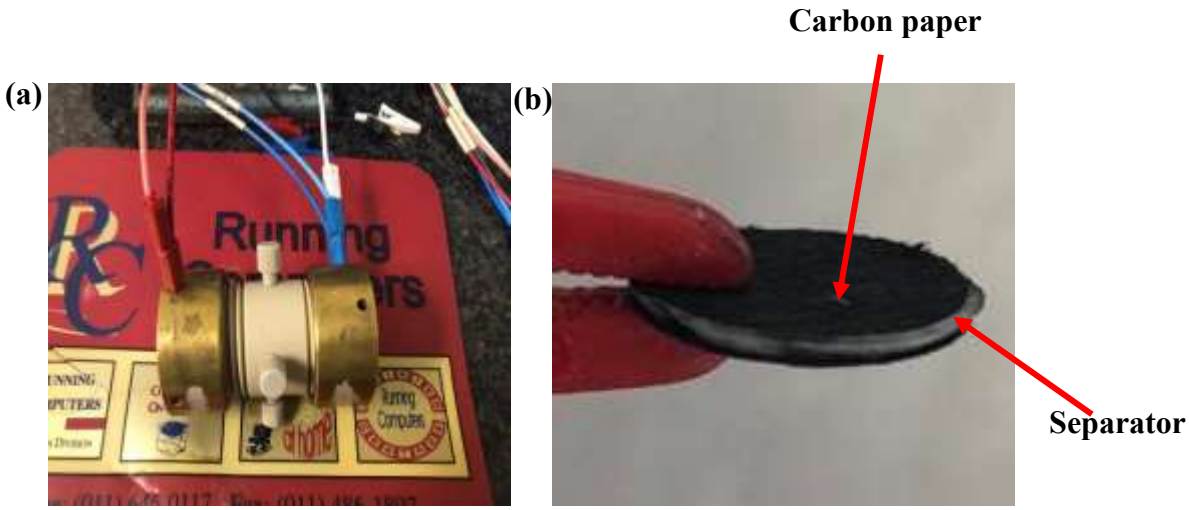


Figure 5. 1: (a) T-type cell used in this study and (b) coated carbon papers (electrodes) with a separator sandwich between the two electrodes.

5.1.2 Screening of materials using a three-electrode system

Screening was conducted using the pristine and annealed CNOs at 750 ℃, 850 ℃ and 950 ℃ for 2 h in 2 M KOH and 2 M H_2SO_4 electrolytes. In particular, a slurry was prepared by dissolving 0.2 mg of the active material in 2 ml DMF. The mixture was sonicated for 30 min.

Glassy carbon (GC) electrode (0.071 cm^2) was used as a working electrode (WE) and it was washed with aluminium powder before use. About 10 µL of the prepared solution was drop-casted on the GC electrode. The solvent was evaporated using an oven at 60 ℃ for 10 min. A silver/silver chloride (Ag/AgCl, saturated 3.0 M KCl) was used as a reference electrode (RE) and platinum wire was used as a counter electrode (CE), all soaked in the electrolyte (see **Figure 5.2**). **Figure 5.2** shows the setup for a three-electrode system used for screening of the materials. Cyclic voltammetry (CV) was used to compare the current responses of the active materials.

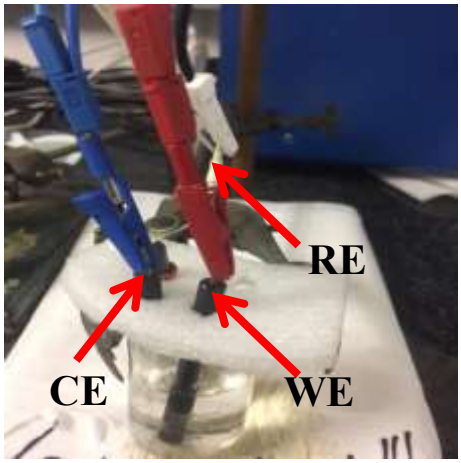


Figure 5. 2: Screening method using a three electrode system.

5.2. Two electrode measurements

A Bio-Logic SP 300 potentiostat (driven by EC-Lab® v 10.40 software) was used to carry out all the electrochemical measurements in a two-electrode system. The electrolyte used was 2 M KOH with Whatman® microfiber filters serving as a porous glass fiber separator. The mass of the pristine, annealed CNOs at 750 ℃ -2 h, B-doped and N-doped CNOs were in a range of 1.0 to 1.2 mg. The electrochemical tests were carried out using three techniques namely CV, GCD and EIS. CV measurements were conducted at potential range of 0.0 to 0.8 V at various scan rates (i.e. 10 mV/s to 100 mV/s). GCD curves were measured at current densities between 0.1 A/g and 10 A/g. EIS measurements were carried out in an open circuit potential in the frequency range from 0.1 Hz to 100 kHz. The EIS data was fitted using Z-fit tool.

The specific capacitance, energy and power density were calculated using **equation 5.1-5.3** [19, 20]:

$$C_{el} = \frac{4I\Delta t}{m\Delta V} \text{ F/g} \qquad \text{eqn 5.1}$$

$$Es = \frac{C_{el}(\Delta V)^2}{28.8} \text{ Wh/kg} \qquad \text{eqn 5.2}$$

$$Ps = \frac{3600E_s}{\Delta t} \text{ W/kg} \qquad \text{eqn 5.3}$$

where C (F/g) is the gravimetric capacitance, I (A) is the applied current, Δt (s) is the discharge time, ΔV (V) is the voltage applied, m(g) is the combination of the two electrode, E_s (Wh/kg) is the specific energy and P_s (W/kg) is the power density.

5.3 Cyclic voltammetry (CV) analysis of the pristine and annealed CNOs

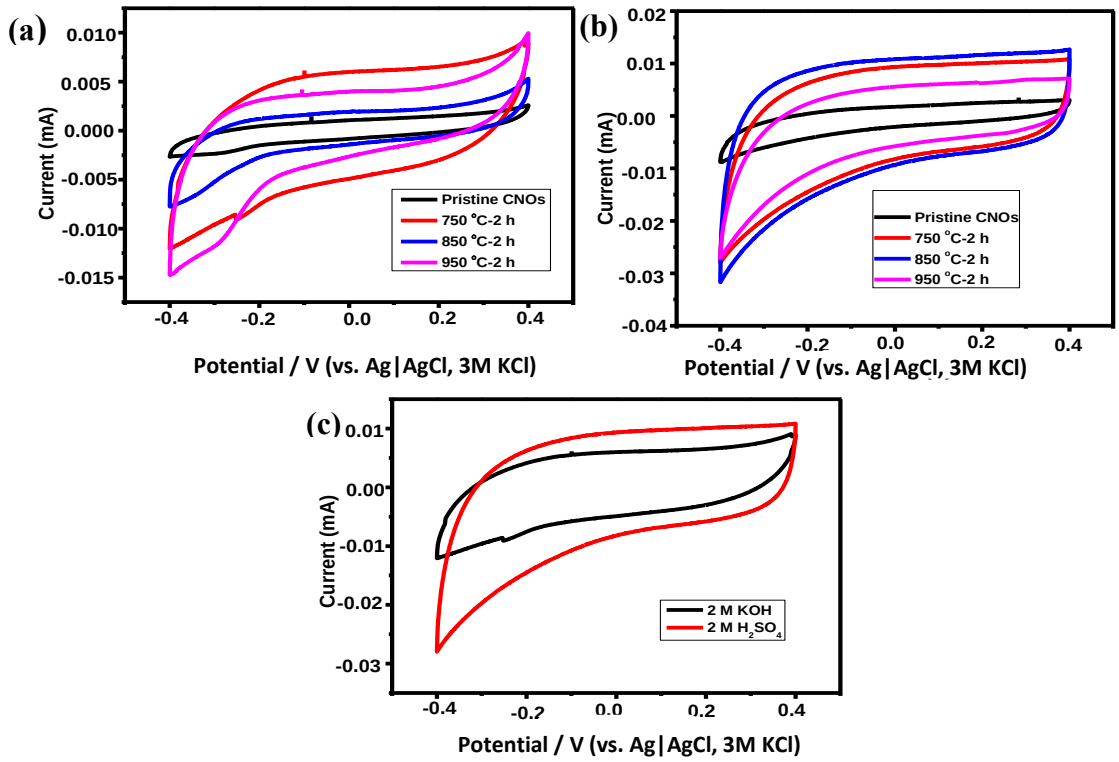


Figure 5. 3: (a) CV curves of pristine and annealed CNOs in 2 M KOH, (b) 2 M H_2SO_4 and (c) Comparison of annealed CNOs at 750 ℃ (2 h) in 2 M KOH and 2 M H_2SO_4. Scan rate: 25 mV/s using a three electrode system.

Screening was conducted using a three-electrode system in either 2 M KOH or 2 M H_2SO_4. The CV curves of the four materials (pristine and annealed CNOs at 750 ℃, 850 ℃ and 950 ℃ for 2 h) (**Figure 5.3a, b**). **Figure 5.3a, b** shows that annealed CNOs at 750 ℃ and 850 ℃ (2 h) had a higher current response compared to the pristine and annealed CNOs at 950 ℃

for 2 h. This can be attributed to the higher conductivity of the materials resulting in a high current response. Lastly, annealed CNOs at 750 ℃ (2 h) in 2 M KOH and 2 M H_2SO_4 were compared as shown in **Figure 5.3c**. The 2 M H_2SO_4 showed better current response which is attributed to the higher ionic conductivity of H_2SO_4 than KOH.

5.4 Cyclic voltammetry (CV) analysis of undoped, B-doped and N-doped CNOs

The experiment used for obtaining the CV curves below was conducted in a two electrode system. The comparison of the CV curve in Figure 5.4 was utilized in a 2 M KOH.

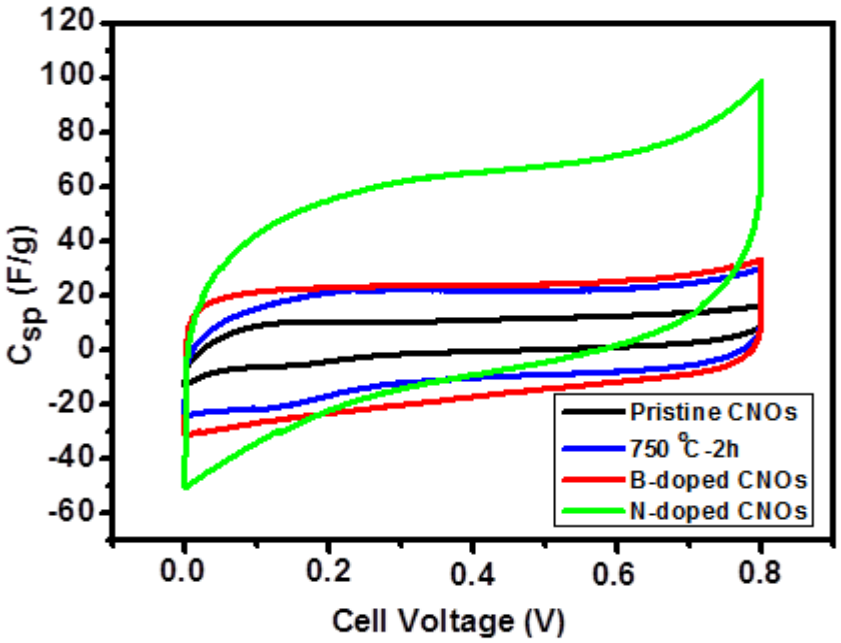


Figure 5. 4: Comparative cyclic voltammograms for pristine CNOs, annealed CNOs at 750 °C (2 h), B-doped CNOs and N-doped CNOs in 2 M KOH at a scan rate of 10 mV/s.

The CV curves of the materials have a quasi-rectangular shape that show the energy storage mechanism is of an electric double layer capacitance (EDLC) [21]. The doping of boron and nitrogen resulted in higher capacitance values with N-doped CNOs outperforming all the other materials. The materials showed better electrochemical performance as compared to the pristine CNOs. The results observed in **Figure 5.4** show that annealing and doping with boron and nitrogen have enhanced the electrochemical performance of the pristine material resulting in an improved specific capacitance.

Scan rate studies were then carried out (10-100 mV/s) as shown in **Figure 5.5** using 2 M KOH in a full symmetric cell at the potential range of 0.0-0.8 V. The increase in scan rates shows that the materials have quasi-rectangular shapes.

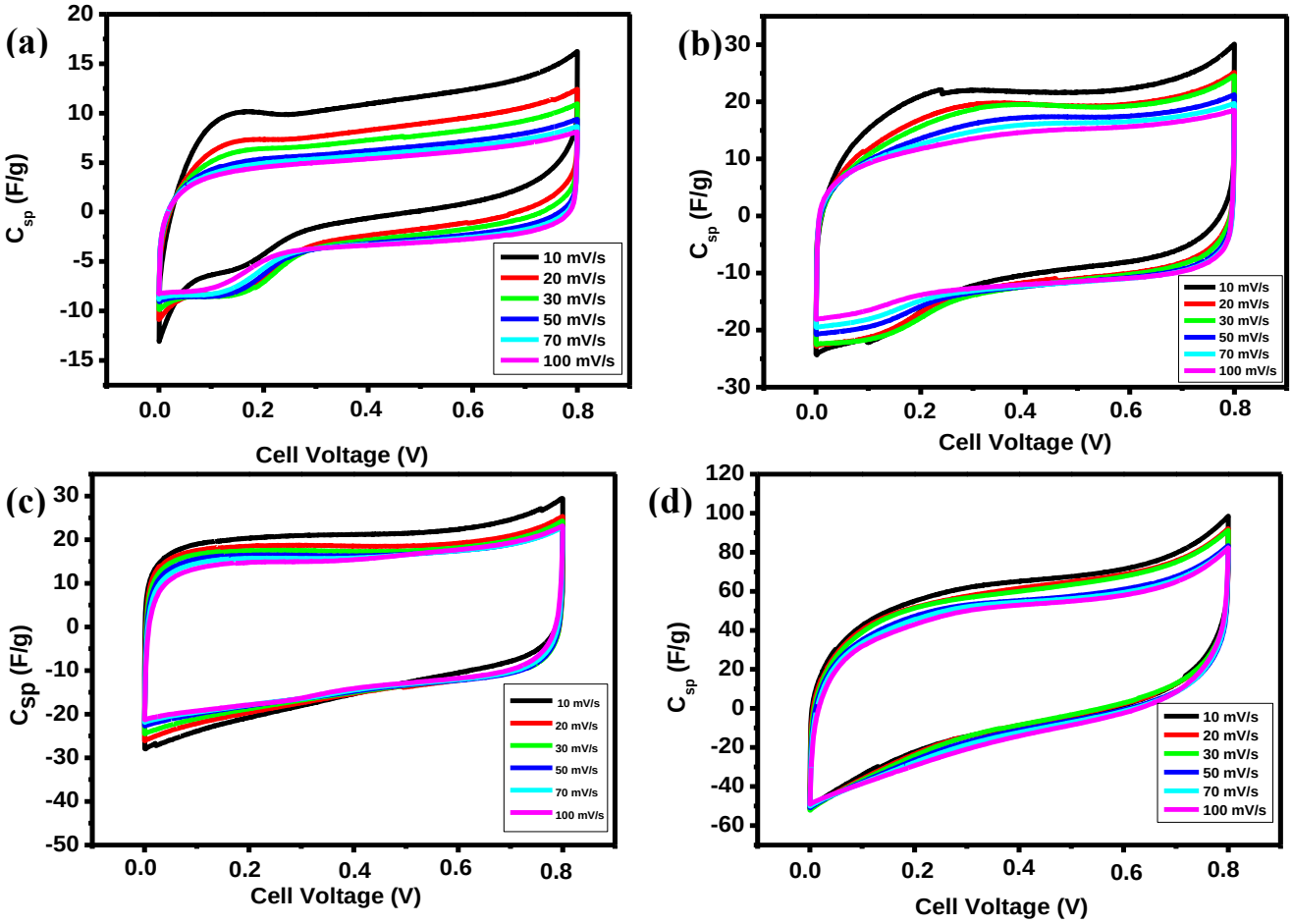


Figure 5. 5: (a) Comparison of cyclic voltammograms for pristine CNOs, (b) annealed CNOs at 750 °C (2 h), (c) B-doped CNOs and (d) N-doped CNOs at various scan rates in 2 M KOH.

The CV curves of the pristine and other CNOs show that the contribution of annealing, as well as boron and nitrogen doping, had a significant effect in the specific capacitance of the pristine material. Although the surface area of B-doped CNOs (73.2 m^2/g) is lower than pristine CNOs (89.9 m^2/g), the B-doped CNOs showed higher capacitance values at all scan rates than pristine CNOs. The total specific surface area is not equivalent to the surface area that is open to electrolyte particles for adsorption; subsequently properties, for example, the structure and layer thickness are considered [22]. The contribution of the higher capacitance of the B-doped CNOs can be attributed to the increase in conductivity of the material. Moreover, the increase in I_D/I_G ratio of the B-doped CNOs (Chapter 4) caused high affinity

for the electrolyte ions. In addition, the decrease of specific capacitance values at high scan rates is because at higher current rates, there is a short time frame for the movement of electrolyte ions into the pores of the anode and cathode material. Furthermore, the CV curves of all the materials retained their rectangular shape at a higher scan rate of 100 mV/s indicating a good capacitive behaviour and that the materials are promising for application in high rate SCs. N-doped CNOs portrayed a higher current response than the other materials which is due to the high specific surface area (116.4 m^2/g) and the improved wettability of the due to the occurrence of nitrogen introducing defects on the carbon surface.

5.5 Galvanostatic charge-discharge of undoped, B-doped and N-doped CNOs

The GCD curves of undoped, B-doped and N-doped CNOs were all linear indicating an EDLC mechanism (**Figure 5.6**). All the GCD curves were performed at numerous current densities stretching from 0.1 to10 A/g. The voltage used was in a range of 0-0.8 V.

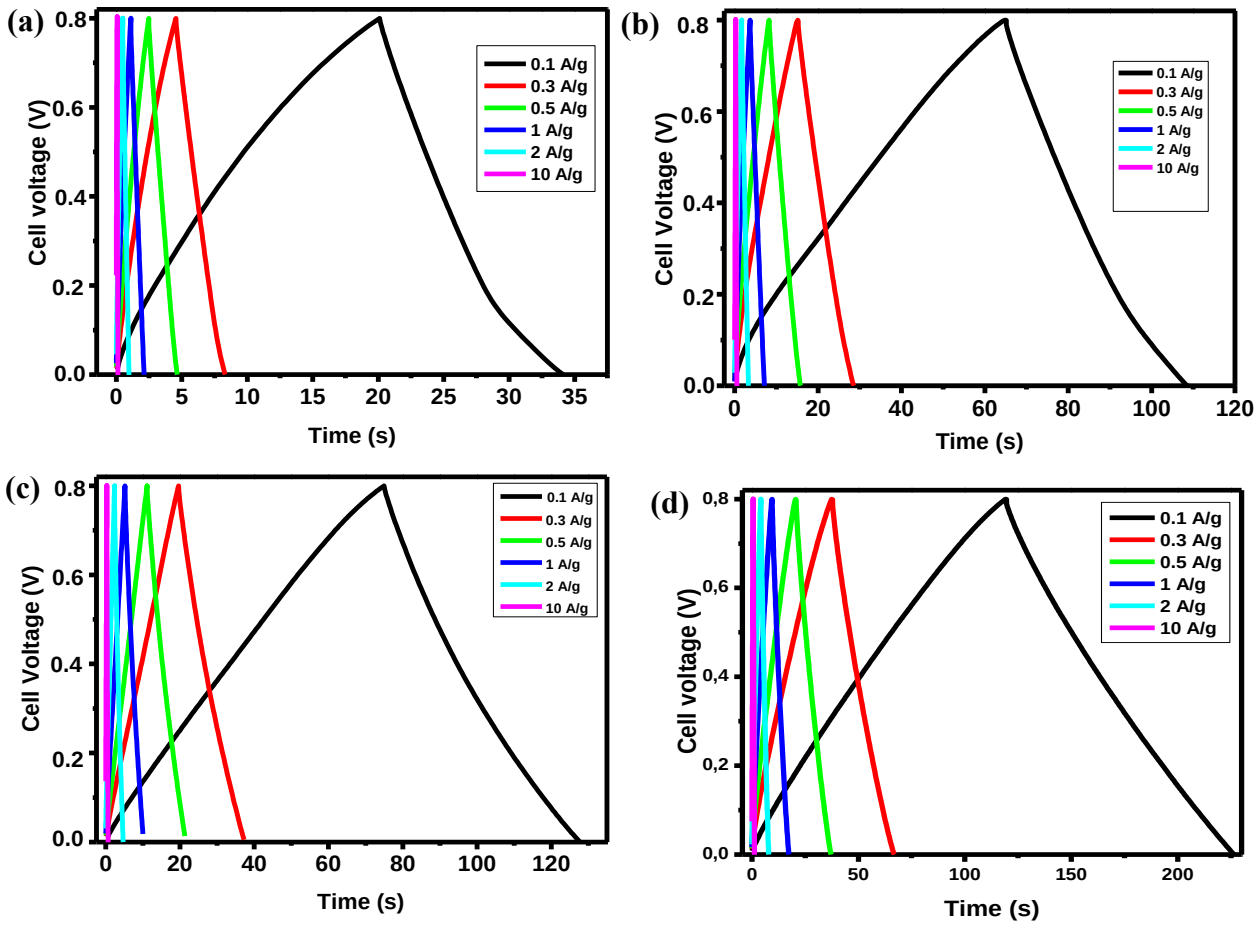


Figure 5. 6: (a) Comparison of galvanostatic charge-discharge at various current densities for pristine CNOs, (b) annealed CNOs at 750 ℃ for 2 h, (c) B-doped CNOs and (d) N-doped CNOs. Electrolyte: 2 M KOH.

The calculated values of the specific capacitances are represented in **Table 5.1** with GCD curves of pristine CNOs shown in **Figure 5.6a**, annealed CNOs at 750 ℃- 2 h (**Figure 5.6b**) as well as B-doped CNOs (**Figure 5.6c**) and N-doped CNOs (**Figure 5.6d**). The improved specific capacitance values of the B-doped and N-doped CNOs can be attributed to the high I_D/I_G ratio (data represented in **Chapter 4**) and the low thermal stability (data presented in **Chapter 4**) that caused the electrolyte ions to have a high affinity to diffuse on the surface of the electrode material. Secondly, the increase in surface area of the N-doped CNOs allowed the electrolyte ions to have easier access to the materials. These results support the CV data, that increasing current results in a decrease in contact time for the movement of electrolyte ions. This then led to lower capacitance values at higher current densities.

Table 5. 1: Specific capacitance (F/g) of the undoped, B-doped and N-doped CNOs at various current densities.

Material	Csp (F/g) at various current densities					
	0.1 A/g	**0.3 A/g**	**0.5 A/g**	**1 A/g**	**2 A/g**	**10 A/g**
Pristine CNOs	7.5 F/g	5.9 F/g	5.5 F/g	5.2 F/g	4.8 F/g	3.1 F/g
Annealed CNOs at 750 ℃ – 2 h	22.5 F/g	20.1 F/g	18.75 F/g	16.5 F/g	14.1 F/g	13 F/g
B-doped CNOs	28 F/g	27 F/g	25 F/g	23 F/g	20 F/g	16 F/g
N-doped CNOs	54 F/g	45 F/g	40.8 F/g	39.3 F/g	36.6 F/g	29.2 F/g

The GCD curves of pristine and CNOs annealed at 750 °C for 2 h as well as B-doped and N-doped CNOs were compared and are shown in **Figure 5.7a** at a current density of 0.1 A/g in 2 M KOH at a potential range of 0.0-0.8 V. All the GCD curves are linear in the potential range of 0.0-0.8V supporting the CV curves, that the energy storage mechanism is that of EDLC. The data from the GCD curves are in agreement with the data from the CV plots that showed that N-doped CNOs gave a better electrochemical performance as compared to the

other carbon materials as shown in **Figure 5.7a.** The N-doped CNOs have the longest discharge time at a current density of 0.1 A/g (green GCD curve). The specific capacitance of the materials calculated from GCD curves (**Figure 5.6**) are shown in **Figure 5.7b**. This supports CV data that the increase in current results in a reduction of the capacitance owing to the limited time given for the flow of electrolyte ions to the surface of the anode and cathode material.

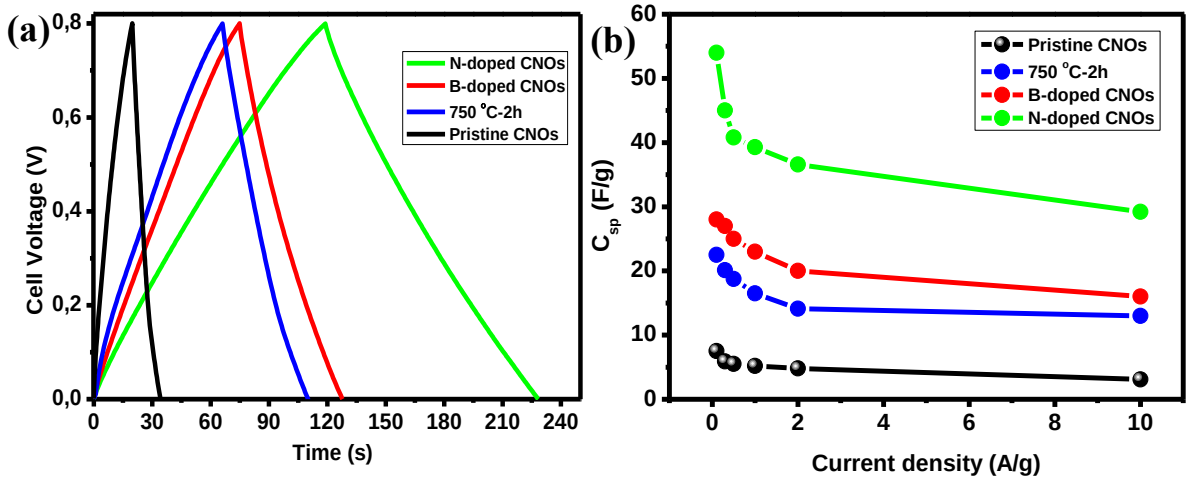


Figure 5. 7: (a) Comparative GCD curves and Csp VS current density (F/g) for pristine CNOs, annealed CNOs at 750 °C-2 h, B-doped CNOs and N-doped CNOs in 2 M KOH at 0.1 A/g.

5.6 Electrochemical impedance spectroscopy analysis of undoped, B-doped and N-doped CNOs

EIS is an important technique for determining the resistivity of the active electrode material, electrolyte and the interaction that occurs at the electrode surface as the electrolyte ions flow to the surface of the material. The Nyquist plots of the undoped, B-doped and N-doped CNOs are represented in **Figure 5.8a**. At high-frequency region, all the materials have a semicircle and a straight line in the low-frequency region called the Warburg resistance. The Warburg resistance is influenced by how electrolyte ions draw in the pores of the material [23]. EIS is used to determine charge transfer resistance (R_{ct}) represented by a semicircle at the high-frequency region [24]. The R_{ct} of each material was measured by using the diameter of the circle from the Nyquist plots. The R_{ct} of the annealed CNOs electrode was 4.33 Ω, followed

by N-doped CNOs with 4.42 Ω, B-doped CNOs with 6.38 Ω and pristine CNOs with 11.23 Ω indicating an improvement in conductivity with all the fitted data presented in **Table 5.2**.

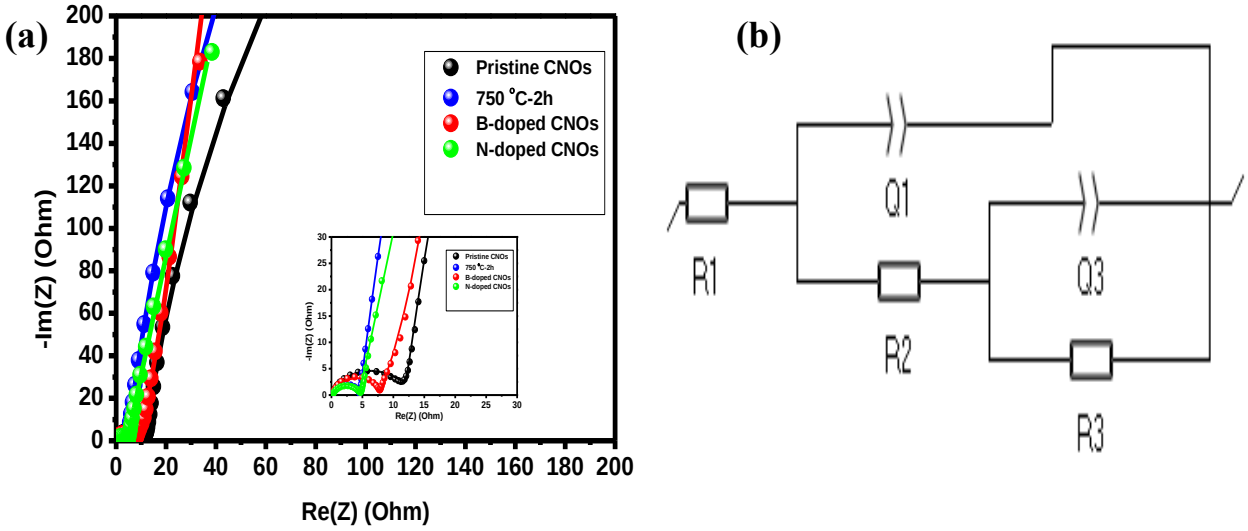


Figure 5. 8: (a) Nyquist plot of pristine, annealed, B-doped and N-doped CNOs after cycling with the inset representing the expanded portion of the high frequency and (b) electrical equivalent circuit (EEC) used to fit the experimental data.

The introduction of nitrogen into the carbon matrix resulted in an improved charge transfer between the electrode material and the electrolyte. From the imaginary impedance axis (y-axis), N-doped, B-doped and annealed CNOs all showed a slight deviation of the curve as compared to the pristine CNOs indicating a short diffusion path length. It is also worth mentioning that the values of η for all the materials are close to 1 indicating an ideal capacitor [25]. The annealed and N-doped CNOs all had the same η_1 and η_2 fitted values indicating almost no change (**Table 5.2**). This indicates a fast redox mechanism which can also be seen from the lower R_{ct} values. The pristine and B-doped CNOs show a change from η_1 to η_2 indicating a resistive charge transfer mechanism [26].

Table 5. 2: Parameters values obtained from the experimental data fitted using EEC.

Parameter	Pristine CNOs	750 ℃-2 h	B-doped CNOs	N-doped CNOs
R_s/Ω	0.23	0.26	0.25	0.25
$Q_1/mF.s^{(\propto-1)}$	15.55×10^{-6}	7.41×10^{6}	15.2×10^{-6}	22.02×10^{-6}

η_1	0.92	0.94	0.93	0.90
R_{CT}/Ω	11.23	4.33	6.38	4.42
Q_3/ mF.$s^{(\propto-1)}$	1.52×10^{-6}	4.38×10^{-3}	4.68×10^{-3}	8.2×10^{-3}
η_2	0.90	0.94	0.86	0.90
R_{CT2}/Ω	1881	2717	0.15×10^{24}	12813

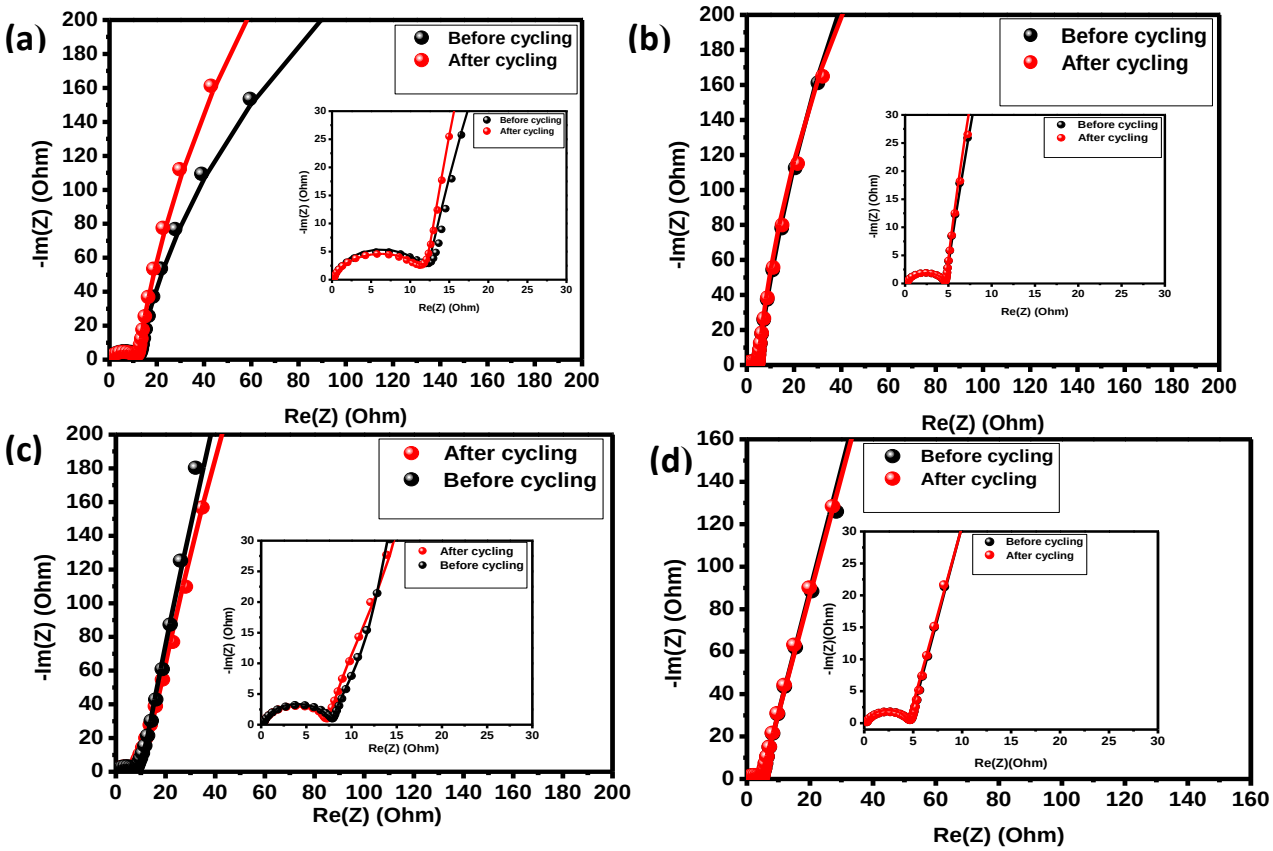


Figure 5. 9: (a) Nyquist plots of the pristine, (b) annealed CNOs, (c) B-doped and (d) N-doped CNOs with the inset representing the expanded portion of the high frequency region before and after cycling.

The behaviour of the materials was studied using EIS plots before and after cycling as shown in **Figure 5.9**. It is worth mentioning that annealed and N-doped CNOs showed no significant change of the straight line before and after cycling (see **Figure 5.9b, d**) which also supports the smaller R_{ct} values obtained after the fitting process. The pristine and B-doped CNOs show a significant change of the EIS plots before and after cycling. This negligible change in EIS

plots of annealed and N-doped CNOs shows that the materials were less resistive before and after cycling.

5.7 Cyclic stability of N-doped CNOs

The cyclic stability of N-doped CNOs was conducted at 2 A/g for 10,000 cycles. **Figure 5.10** shows the capacitance retention of the N-doped CNOs after 10,000 cycles. The coulombic efficiency observed was stable with a value of 99.99% at 10,000 cycle. The N-doped CNOs are highly stable with capacitance retention of 89.8%. The stability of the N-doped CNOs indicates that the material is promising for use in high rate SCs.

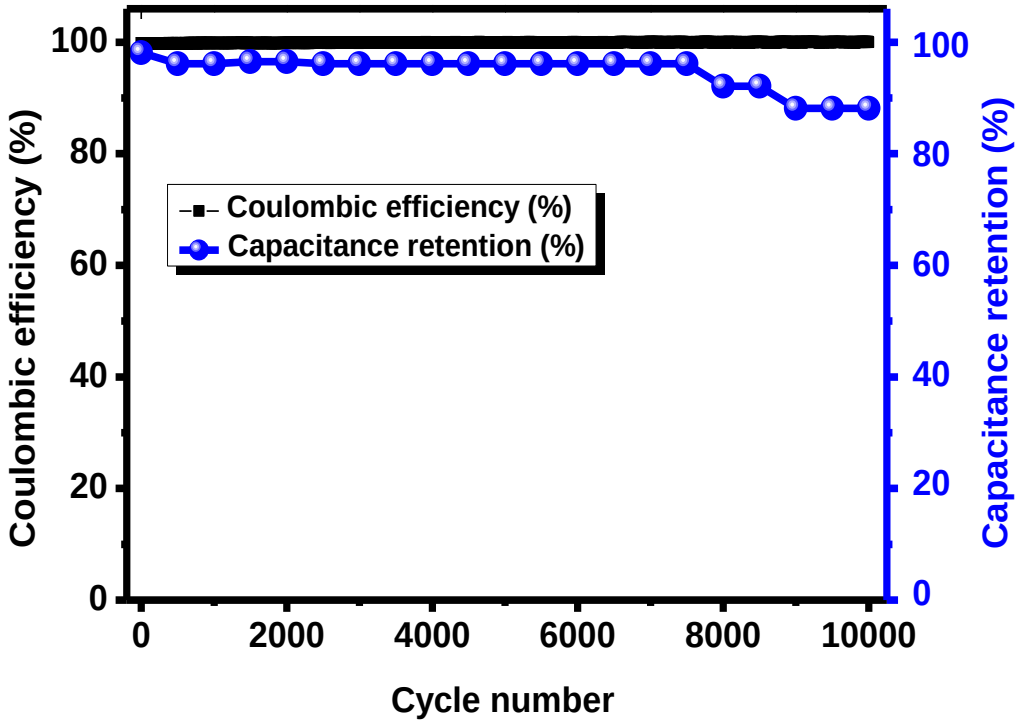


Figure 5. 10: Cycling stability of the N-doped CNOs after 10,000 cycles.

5.8 Ragone plot of undoped, B-doped and N-doped CNOs

It is important to determine how much charge is stored and how fast the charge can be stored and released in energy storage devices. Hence, the performance of SCs can be evaluated

using two parameters; energy and power density. The Ragone plot of the pristine, annealed CNOs at 750 ℃ for 2 h, B-doped CNOs and N-doped CNOs is shown in **Figure 5.11**. As shown from the CV and GCD, the N-doped CNOs performed better with regard to the electrochemical performance as compared to the other materials.

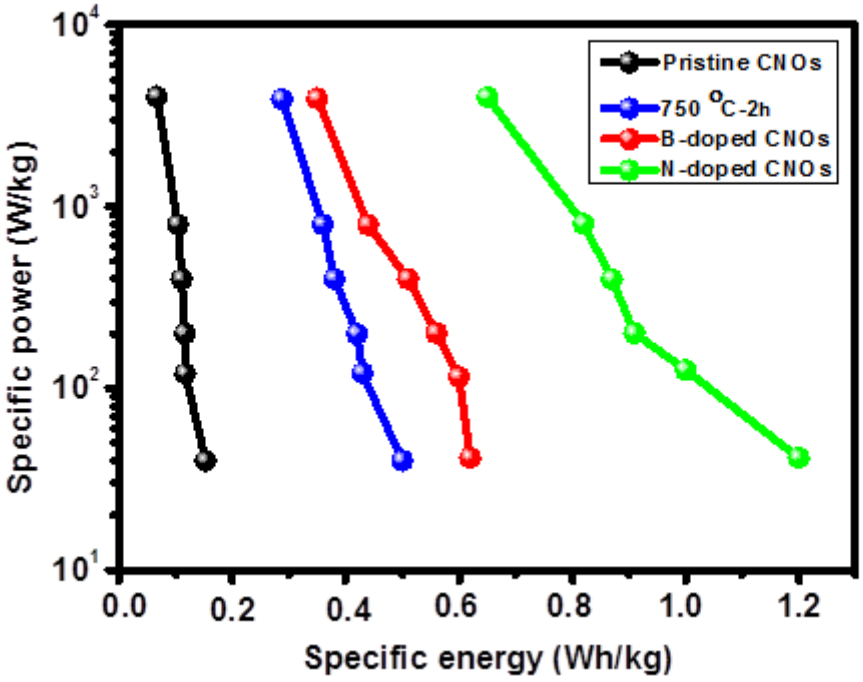


Figure 5. 11: Ragone plot of pristine, annealed, B-doped and N-doped CNOs. Electrolyte: 2 M KOH electrolyte.

The maximum energy density is high for the N-doped CNOs with a value of 1.2 Wh/kg. The B-doped CNOs showed a maximum energy density of 0.62 Wh/kg followed by annealed CNOs at 750 ℃ with 0.5 Wh/kg and pristine CNOs with a maximum energy density of 0.15 Wh/kg all at a current density of 0.1 A/g. However, the power density decreased with an increase in energy density with a value of 4002 W/kg (at 10 A/g) for all the materials. The increase in energy densities observed with the N-doped CNOs shows that indeed nitrogen improved the wettability of the material which resulted in improved electrolyte ion adsorption on the electrode surface. The achieved power density of the materials was relatively high despite the low energy density. For example, Mohapatra *et al*. reported the power density of 1224 W/kg for CNOs synthesized from flame pyrolysis [27]. Again, Mykhailiv *et al*. reported a power density of 4900 W/kg for boron-doped CNOs at a current density of 30 A/g [17].

The key findings from **Figure 5.4-5.11** can be summarized as follows:

(i) The specific capacitance, charge-separation, energy density of the CNOs was improved by dopants such as nitrogen and boron.

(ii) The N-doped CNOs showed better electrochemical performance compared to the other materials followed by B-doped CNOs.

(iii) The lowest electrochemical performance was from the pristine CNOs and annealed CNOs (750 ℃ for 2 h).

As mentioned in the literature review (**Chapter 2**), both nitrogen and boron have a significant effect on the specific capacitance of carbon materials. Thus, the role of boron and nitrogen doping on carbon surface had gained tremendous attention over recent years. The surface area and dopant content are key factors in the electrochemical performance of doped carbon materials. To date, a large number of boron and nitrogen doped carbon materials for application in SCs has been reported in literature and their capacitive performance are summarized in **Table 5.3.**

Table 5. 3: Summary of specific capacitance of boron and nitrogen doped carbon material together with their specific surface area and pore volume.

Type of material	**S.A (m^2/g)**	**Pore volume (cm^3/g)**	**Pore size (nm)**	**N/B (%)**	**Electrolyte**	**Current density (A/g)**	**Specific capacitance (F/g)**	**Ref**
Pristine material	89.8	0.07	3.2	-	2 M KOH	0.1	7.5	This study
B-doped CNOs	73.24	0.18	8.6	-	2 M KOH	0.1	28	This study
N-doped CNOs	116.4	0.11	3.4	1.7	2 M KOH	0.1	54	This study
B-CNOs	288	1.305	17	0.76	1 M H_2SO_4	0.1	27	[17]
1650 - CNOs	454	1.660	12	-	1 M H_2SO_4		20	[18]
1650-N-	383	1.534	16	-	1 M H_2SO_4		17	[18]

CNOs								
CSs	41.2	-	-	-	1 M H_2SO_4	0.1	13.4	[28]
N-CSs	93.7	-	-	2.5	1 M H_2SO_4		42.7	[28]
CNTs	106	0.63	-	-	6 M KOH	0.25	3	[29]
N-CNTs	225	0.37	-	2.5	6 M KOH	0.25	41	[29]

(Key: CNOs= carbon nano-onions; CSs= carbon spheres; CNTs= carbon nano-tubes)

The results represented in **Table 5.3** show that nitrogen and boron improve the specific capacitance of the pristine material. The B-CNOs reported in literature delivered similar specific capacitances to the B-doped CNOs reported in this work. Moreover, the N-CNOs showed superior specific capacitance than other reports on related materials.

5.9 Conclusions

In this work, the electrochemical properties of the pristine, annealed, B-doped and N-doped CNOs were investigated using 2 M KOH electrolyte in a two-electrode system. The N-doped CNOs in a two-electrode system showed better electrochemical performance as compared to the other carbon materials. In particular, N-doped CNOs showed the longest discharge time from the GCD curves at all current densities. Moreover, the N-doped CNOs gave a capacitance retention of 89.8% after 10,000 cycles at a specific current density of 2 A/g. The role of annealing, as well as boron and nitrogen doping, has demonstrated their significant role in modifying the electrochemical properties of CNOs. The significant role of annealing, boron and nitrogen doping provides advantages on the use of CNOs as energy storage materials.

5.10 References

1. W. Gu, G. Yushin. *WIREs Energy Environmental* 3 (2014) 424.
2. F. Béguin, V. Presser, A. Balducci, E. Frackowiak. *Advanced Materials* 14 (2014) 2219.
3. V. Ruiz, C. Blanco, E. Raymundo-Piñero, V. Khomenko, F. Béguin, R. Santamaría. *Electrochimica Acta* 15 (2007) 4969.
4. S. B. Ma, K. W. Nam, W. S. Yoon, X. Q. Yang, K. Y. Ahn, K. H. Oh, K. B. Kim. *Electrochemistry Communication* 9 (2007) 2807.
5. E. R. Nightingal. *Physical Chemistry* 63 (1959)1381.
6. R. D. Shannon. *Acta Crystallographica A* 32 (1976) 751.
7. S.I. Fletcher, F.B. Sillars, R.C. Carter, A.J. Cruden, M. Mirzaeian, N.E. Hudson, J.A. Parkinson, P.J. Hall. *Power Sources* 195 (2010) 7484.
8. C. Zhong, Y. Deng, W. Hu, J. Qiao, L. Zhangd, J. Zhang. *Chemical Society Review* 44 (2015) 7484.
9. K. Fic, G. Lota, M. Meller, E. Frackowiak. *Energy and Environmental Science* 5 (2012) 5842.
10. R. Y. Lin, P. L. Taberna, S. Fantini, V. Presser, C. R. Perez, F. Malbosc, N. L. Rupesinghe, K. B. K. Teo, Y. Gogotsi, P. Simon. *Physical Chemistry Letters* 2 (2011) 2396.
11. A. Brandt, S. Pohlmann, A. Varzi, A. Balducci, S. Passerini. *MRS Bulletin* 38 (2013) 554.
12. N. A. Choudhury, S. Sampath, A. K. Shukla. *Energy and Environmental* 2 (2009) 55.
13. H. Gao, K. Lian. *RSC Advances* 4 (2014) 33091.
14. G. Lota, E. Frackowiak. *Electrochemistry Communications* 11 (2009) 87.
15. D. Pech, M. Brunet, H. Durou, P.H. Huang, V. Mochalin, Y. Gogotsi, P.L. Taberna, P. Simon. *Nature Nanotechnology* 5 (2010) 651.
16. Y. Gao, Y.S. Zhou, M. Qian, X.N. He XN, Redepenning J, Goodman P, Li HM, Jiang L, Lu YF. *Carbon* 51 (2013) 52.
17. O. Mykhailiv, H. Zubyk, K. Brzezinsk, M. Gras, G. Lota, M. Gniadek, M. Romero, L. Echegoyen, M. E. Plonska-Brzezinska. *Chemistry of Nanomaterials* 23 (2017) 7132.

18. O. Mykhailiv, K. Brzezinski, B. Sulikowski, Z. Olejniczak, M. Gras, G. Lota, A. Molina-Ontoria, M. Jakubczyk, L. Echegoyen, M.E. Plonska-Brzezinska. *Chemistry A Europian Journal* 23 (2017) 7132.
19. W. Yang, W, Z. Gao, J. Wang, J. Ma, M. Zhang, L. Liu. *ACS Applied Materials and Interfaces* 5 (2013) 5443.
20. Y.J. Kang, H. Chung, C.H. Han, W. Kim. *Nanotechnology* 8 (2012) 065401.
21. P. Simon, Y. Gogotsi. *Nature Materials* 7 (2008) 845.
22. W. Li, G. Reichenauer, J. Fricke. *Carbon* 40 (2002) 2955.
23. Z.P. Li, Y.J. Mi, X.H, Liu, S. Liu, S.R. Yang, J.Q. Wang. *Materials Chemistry* 8 (2011) 14706.
24. A. Lasia. Electrochemical Impedance Spectroscopy and its Application, Springer, (2014) 177.
25. P. Sarma, N. Hylten-Cavallius. *IEEEE Transactions on Power Apparatus and Systems* 94 (1975 1708.
26. L.L. Zhang, X.S. Zhao. *Chemical Society Reviews* 38 (2008) 2520.
27. D. Mohapatra, S. Badrayyana, S. Parida. *Chemical Physics* 174 (2016) 112.
28. W. Lee and J. Moon. *ACS Applied Materials and Interface* 6 (2014) 13968.
29. L. Liao, C. Pan. *Soft NanoScience Letters* 1 (2011) 16.

Chapter 6: General conclusions and recommendations

This chapter gives the general conclusions on the work reported in this study. The shortcomings of this study have been discussed followed by the presentation of research ideas that could be done to improve what has been reported in this study.

6.1 Properties of CNOs synthesized from CVD method

CNOs were synthesized at different temperatures (450 ℃-650 ℃). The CNOs synthesized gave rise to a mixture of products such as CNFs and CNTs. The type of carbon nanostructure obtained using CVD gave a lower specific surface area compared to CSs. The method does not provide pure CNOs in high yield.

6.2 Properties of CNOs synthesized from flame pyrolysis method

CNOs synthesized from the flame pyrolysis method have quasi-spherical shape with a particle size less than 100 nm. The synthesized material was purely carbonaceous as confirmed by TGA. Annealing of the materials resulted in a more graphitized material as confirmed by Raman spectra. Boron and nitrogen doping did not disrupt the structure of the CNOs as confirmed by TEM images. The doping process resulted in an increase in structural defects confirmed by the high I_D/I_G ratio from Raman spectra. CNOs synthesized from flame pyrolysis exhibited a high surface area compared to CNOs synthesized from the CVD method.

6.3 Application of CNOs in SCs

The main objective in this study was to improve the surface area and conductivity by annealing at different temperatures and times. The incorporation of boron and nitrogen into the lattice of CNOs was achieved through doping which also improved the conductivity of the CNOs. It was observed that both annealing and doping improved the surface area of the CNOs thus increasing the capacitance leading to an improved amount of energy storage.

6.4 Recommendations

Based on the findings from this study, CNOs are promising energy storage materials that can be improved in order to increase the amount of energy stored. The amount of energy stored could be improved by using higher concentrations of dopants at higher temperatures.

Another strategy will be to use a more conductive electrolyte (i.e. 6 M KOH) or electrolytes that operate at a wider voltage to increase the amount of energy storage.

Finally, to achieve a greater energy density, the electrode material can be mixed with conductive carbon acetylene black to improve the conductivity of the CNOs material.

Appendix A: Supplementary Information

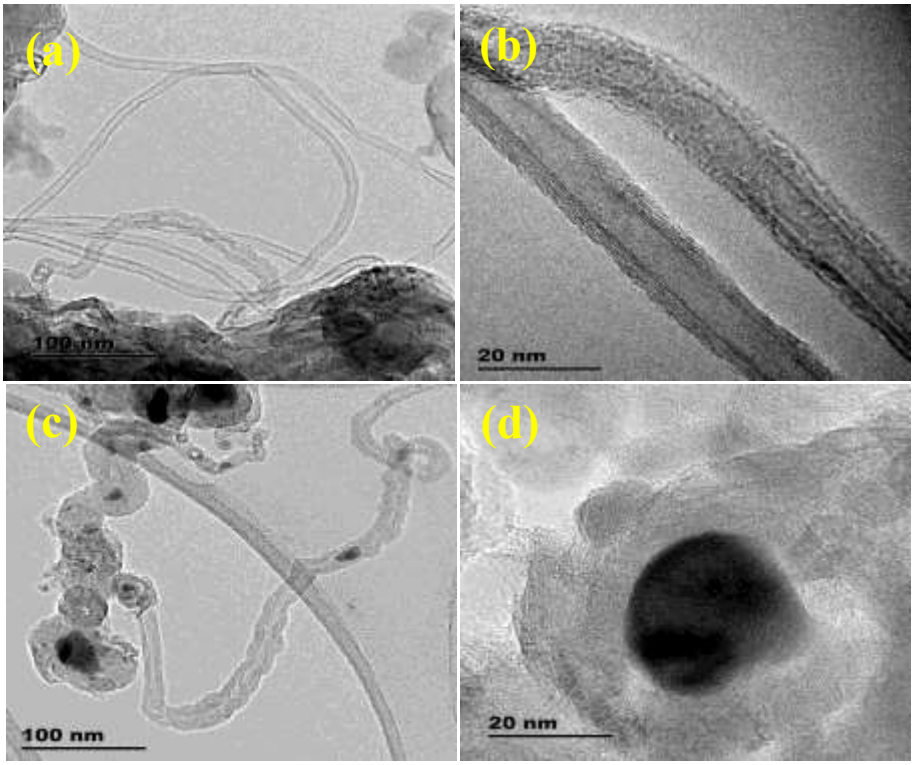


Figure S1: TEM images of carbon materials grown at (a-c) 650℃ (Sample 5) and (d) 550 ℃ (sample 4).

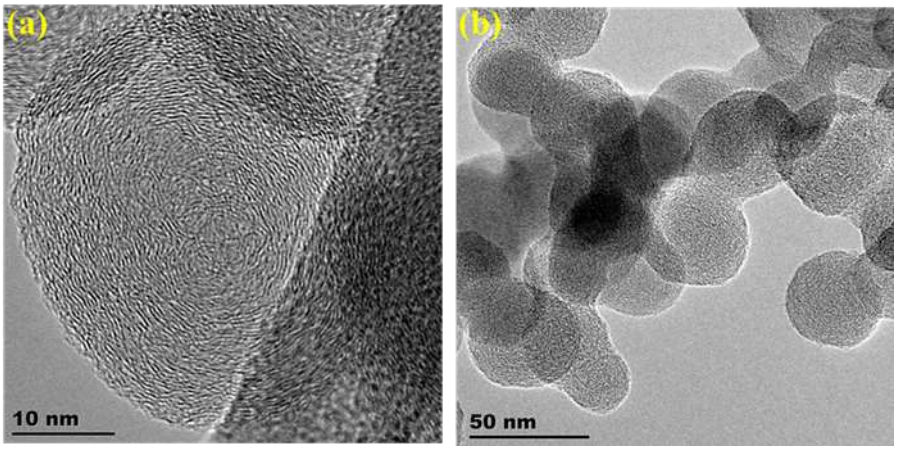


Figure S2: TEM images of (a) pristine and (b) B-doped CNOs.

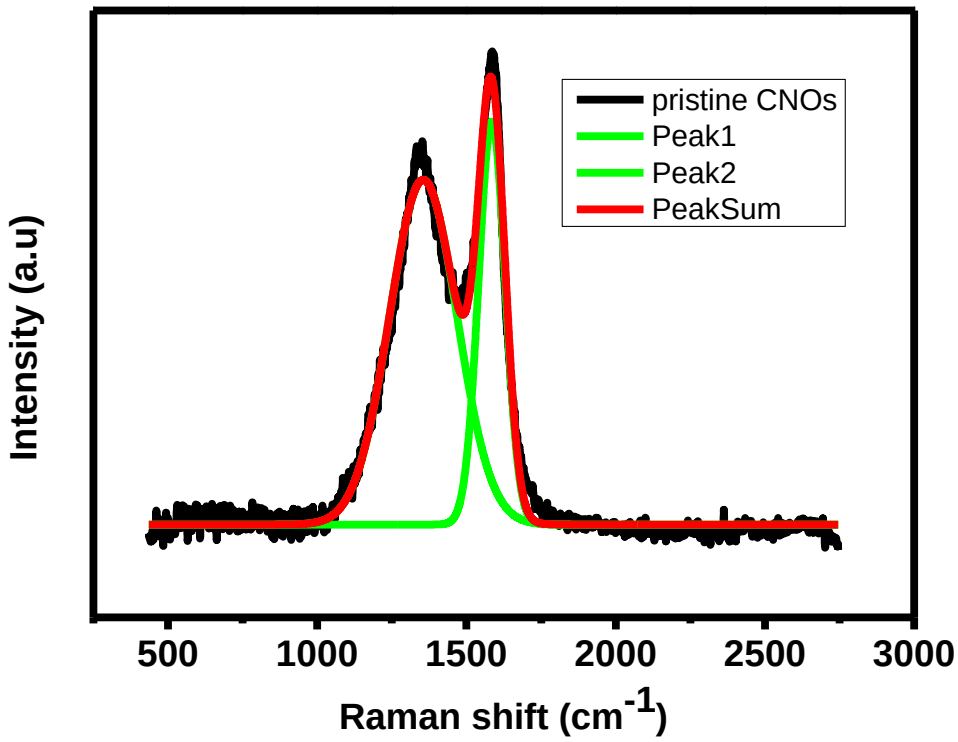


Figure S3: Raman spectra of pristine CNOs used for determination of the FHWM.